Inês Sofia Cortes Eusébio Camacho

Licenciatura em Bioquímica

Effects of UV radiation exposure on DNA and DNA repair enzymes

Dissertação para obtenção do Grau de Mestre em Biotecnologia

Orientador: Doutor Filipe Folgosa, Investigador Pós-Doc, FCT-UNL
Co-orientador: Doutora Cristina M. Cordas, Investigadora Auxiliar, FCT-UNL
Co-orientador: Prof. Doutora Alice S. Pereira, Professora Auxiliar, FCT-UNL

FACULDADE DE CIÊNCIAS E TECNOLOGIA
UNIVERSIDADE NOVA DE LISBOA

Setembro de 2012

“Copyright”

Effects of UV radiation exposure on DNA and DNA repair enzymes

Inês Sofia Cortes Eusébio Camacho

Faculdade de Ciências e Tecnologia

Universidade Nova de Lisboa

Agradecimentos

Em primeiro lugar, gostaria de agradecer aos meus orientadores, Dr. Filipe Folgosa, Dra. Cristina M. Cordas e Prof. Dra. Alice S. Pereira, por me terem dado a oportunidade de realizar a minha tese de mestrado no seu grupo de investigação. Estou deveras grata não só pela enorme ajuda científica, mas principalmente pelo apoio, estímulo e conselhos dados ao longo da realização deste trabalho.

Aos Drs. Filipe Folgosa e Cristina M. Cordas, gostaria ainda de agradecer a amizade, o companheirismo, a paciência, a disponibilidade e a compreensão demonstrados ao longo deste ano. Agradeço também as merecidas chamadas de atenção. Filipe e Cristina, vocês são os meus mentores! Pelo meu crescimento científico e pessoal, e por tudo, um muito obrigada!

Aos Profs. Drs. Pedro Tavares e Alice S. Pereira, agradeço o facto de me terem recebido no seu laboratório e facultado a utilização do seu material e equipamentos. Gostaria ainda de agradecer ao Prof. Dr. Pedro Tavares pelos debates e conversas inspiradoras (embora nem sempre de acordo), pelas suas opiniões e conselhos, e, principalmente, por acreditar em mim. Obrigada!

Agradeço à Daniela Penas, colega de laboratório, a ajuda e disponibilidade demonstradas. À Joana Wilton, Rui Almeida, Cristina Timóteo, Susana Ramos, Ana Pina e Leonor Morgado, agradeço o convívio e a boa disposição. Em suma, a todo o pessoal do laboratório 425 (presente no dia-a-dia e os que por lá passam de vez em quando), agradeço o excelente ambiente, a boa disposição e os momentos de convívio e descontracção que tanto me animaram durante este ano.

Às minhas amigas de Mestrado, Joana e Viviana, agradeço a amizade, o apoio, a motivação e os momentos de descontracção e "parvoíce" partilhados ao longo dos últimos dois anos. Obrigada por aturarem os meus stresses e devaneios constantes. À Joana, agradeço ainda as longas conversas telefónicas que tanto me animaram nesta fase. Obrigada!

Aos meus amigos, em especial ao Márcio, à Marina, à Susana e ao Natan, agradeço principalmente a compreensão pela minha "ausência" durante esta fase e o facto de estarem sempre disponíveis para me ouvir e animar. Prometo que vos recompenso! Agradeço a amizade, o apoio e os bons momentos passados ao longo destes anos. Obrigada por me aturarem!

Ao João, agradeço o amor, o carinho, a amizade, o apoio, a força e a paciência demonstrados ao longo destes anos e principalmente nesta fase.

E, por fim, o agradecimento mais importante. Aos meus pais, a quem agradeço a minha vida! Obrigada pelo amor e apoio incondicionais, obrigada pela força, paciência e compreensão demonstrados ao longo de uma vida. Se não fossem vocês, eu não teria chegado onde cheguei nem seria o que sou hoje. Obrigada mãe, por me "picares" e "arreliares", e assim contribuíres para o meu progresso. Agradeço também à minha avó e ao meu irmão pelo amor e apoio incondicionais. Apesar de não nos falarmos com muita frequência, vocês estão sempre no meu coração. Agradeço também aos meus sobrinhos lindos por me fazerem sentir uma criança (mais ainda) e por compreenderem que a "Titi" tem que se ausentar muitas vezes e nem sempre pode brincar com eles tanto quanto gostaria. Obrigada por tudo, família, vocês são a minha força motriz!

Resumo

Na célula, a integridade do DNA está sob constante ameaça de agentes nocivos de origem endógena ou exógena, tais como as radiações UV e ionizantes e o stress oxidativo. Embora os efeitos destes agentes cancerígenos no DNA já tenham sido extensivamente estudados, muito pouco se sabe sobre o seu efeito nas enzimas de reparação do DNA.

O objectivo do presente trabalho foi o estudo do efeito da radiação UV na Endonuclease III de *E. coli*, uma DNA glicosilase pertencente ao sistema de reparação por excisão de bases. Esta enzima foi sobre-expressa homologamente e posteriormente purificada com um rácio Fe/proteína de 3.88 ± 0.63 (holoproteína).

A exposição da Endonuclease III à radiação UV durante 45 min (dose equivalente a 19.77 kJ) conduz possivelmente à destruição das ligações Fe-S do centro [4Fe-4S] ou à conversão deste centro a um estado redox diferente.

Os ensaios de mobilidade electroforética realizados mostram que a ligação da Endonuclease III ao DNA plasmídico promove um retardamento da banda correspondente à forma superenrolada do DNA, indicativo da formação de complexo(s) Endonuclease III-DNA. Estes ensaios mostram igualmente que a Endonuclease III é capaz de se ligar tanto à forma linear do DNA plasmídico como à superenrolada, embora com maior afinidade para a forma linear.

Ensaios de mobilidade electroforética realizados após 45 min de irradiação UV (19.77 kJ) revelam que, apesar de ocorrer um retardamento, os complexos formados são instáveis e dissociam-se durante a electroforese. Além disso, a presença de agregados proteína-DNA sugere a desnaturação de algumas proteínas. Após 6 h de irradiação (158.18 kJ) não se formam complexos, o que permite concluir que as moléculas de Endonuclease III foram irreversivelmente danificadas.

Os estudos electroquímicos foram realizados por voltametria cíclica e de pulso diferencial, à temperatura ambiente e em condições anaeróbicas; a Endonuclease III livre e o complexo Endonuclease III-DNA foram adsorvidos à superfície de um eléctrodo de grafite pirolítica não modificado. Pela primeira vez, foi observada a resposta electroquímica directa da Endonuclease III sem estar ligada ao DNA, com um par redox quasi-reversível exibindo um potencial formal de 178 ± 9 mV *vs.* NHE. A ligação da Endonuclease III ao DNA plasmídico promove um desvio (19 mV *vs.* NHE) do par redox característico da Endonuclease III para potenciais mais positivos. A irradiação do complexo proteína-DNA promove um desvio negativo de 25 mV *vs.* NHE no seu potencial redox.

Palavras-chave: Endonuclease III; DNA plasmídico; complexo proteína-DNA; radiação UV; ensaios de mobilidade electroforética; bioelectroquímica.

Abstract

DNA integrity in the cell is under constant threat from damaging agents of endogenous or exogenous origin, such as UV light, ionizing radiation and oxidative stress. Although the effects of these carcinogens on DNA have been extensively studied, very little is known about their effect on DNA repair enzymes.

The aim of the present work was the study of the effect of UV radiation on *E. coli* Endonuclease III, a DNA glycosylase belonging to base excision repair system. This enzyme was homologously overexpressed and then purified with a Fe/protein ratio of 3.88 ± 0.63 (fully-loaded form).

Endonuclease III exposure to UV radiation for 45 min (19.77 kJ dose) may lead to the destruction of the Fe-S bonds of the [4Fe-4S] cluster or to the conversion of this center into a different redox state.

Electrophoretic mobility shift assays with protein-DNA complex showed that Endonuclease III binding to plasmid DNA promotes a retardation of the free supercoiled DNA band, indicative of Endonuclease III-DNA complex(es) formation. These assays also showed that Endonuclease III is able to bind both linear and supercoiled plasmid DNA, although with higher affinity for the linear form.

Electrophoretic mobility shift assays performed after 45 min of UV irradiation (19.77 kJ) revealed that although shift occurred, the complexes formed were unstable and dissociated during electrophoresis. Moreover, the presence of aggregates suggests the unfolding of some Endonuclease III molecules. After 6 h of UV irradiation (158.18 kJ) no complexes are formed, leading to the conclusion that Endonuclease III molecules were irreversibly damaged.

The electrochemical studies were performed by cyclic and differential pulse voltammetry techniques, at room temperature and anaerobic conditions; Endonuclease III and Endonuclease III-DNA complex were adsorbed on a bare pyrolytic graphite electrode. For the first time, the direct electrochemical response of Endonuclease III unbound to DNA was observed, with a quasi-reversible redox couple displaying a midpoint potential of 178 ± 9 mV *vs.* NHE. Endonuclease III binding to plasmid DNA promotes a positive shift (19 mV *vs.* NHE) in the characteristic redox couple of Endo III. Protein-DNA complex UV irradiation promotes a negative shift in its redox potential of 25 mV *vs.* NHE.

Keywords: Endonuclease III; plasmid DNA; protein-DNA complex; UV radiation; electrophoretic mobility shift assays; bioelectrochemistry.

Abbreviations, symbols and constants

Abbreviations

aa	Amino acid
Abs	Absorbance
Amp	Ampicillin
AP	Apurinic/apyrimidic
APE1	Apurinic/apyrimidic endonuclease
APS	Ammonium persulfate
Asp	Aspartate
BCA	Bicinchoninic Acid
BER	Base excision repair
bp	(DNA) base pairs
BSA	Bovine serum albumin
CE	Counter electrode
CPD	Cyclobutane pyrimidine dimers
CT	Charge transport
CV	Cyclic voltammetry
D. vulgaris	*Desulfovibrio vulgaris* strain Hildenborough
DPV	Differential pulse voltammetry
DR	Direct repair
DSB	Double-strand break
E. coli	*Escherichia coli*
Endo III	Endonuclease III
FCL	Fe-S cluster loop
Fd	Ferredoxin
GPD	Gly/Pro-rich loop
HhH	Helix-hairpin-helix
HiPiP	"High-potential" iron protein
HOPG	Highly oriented pyrolytic graphite
HR	Homologous recombination

ICL	Interstrand crosslink
IPTG	Isopropyl-β-D-thiogalactopyranoside
LB	Luria Bertani broth, known as Luria Broth
LB/Agar/Amp	Luria Broth containing Agar and Ampicillin
LMW	Low molecular weight
MMR	Mismatch repair
MWCO	Molecular weight cut-off
NER	Nucleotide excision repair
NHE	Normal hydrogen electrode
NHEJ	Non-homologous end joining
OD	Optic density
PDB	Protein data bank
pDNA	Plasmid DNA
PG	Pyrolitic graphite
Pol β	Polimerase β
Rd	Rubredoxin
RE	Reference electrode
RNS	Reactive nitrogen species
ROS	Reactive oxygen species
SCE	Saturated calomel electrode
SDS	Sodium dodecyl sulfate
SDS-PAGE	Sodium dodecyl sulfate – Polyacrylamide gel electrophoresis
SSB	Single-strand break
TEMED	N,N,N',N'-tetramethylethylenediamine
Tris	Tris(hydroxymethyl)methylamine
Trp	Tryptophan
Tyr	Tyrosine
UV	Ultraviolet
Vis	Visible light
WE	Working electrode

Symbols and constants

A_{geom}	Geometric area
c	Concentration
C	Coulomb
ε	Molar extinction coefficient
E	Potential
$E^{0'}$	Formal reduction potential
E_p	Peak potential
E_{pa}	Anodic peak potential
E_{pc}	Cathodic peak potential
ΔE_p	Potential difference
F	Faraday constant
I	Current
I_p	Maximum peak current
I_{pa}	Maximum anodic peak current
I_{pc}	Maximum cathodic peak current
K_{sh}	Heterogeneous electron-transfer rate constant
mUA	Milliunits of absorbance
n	Number of electrons
N_A	Avogrado constant
R	Molar gas constant
T	Temperature
υ	Scan rate
V	Volt

Table of contents

Figures Index

Tables Index

Chapter 1 Introduction

During a lifetime, organisms are constantly exposed to harmful agents, both exogenous and endogenous, that may cause damage and jeopardize the integrity of their genome.

1.1 DNA damage and its consequences

1.1.1 Damage to the DNA nucleobases

A perplexing myriad of lesions threatens DNA integrity in three main ways. First, some chemical bonds in DNA tend to spontaneously disintegrate under physiological conditions. The simplest reaction that is potentially harmful to DNA is the spontaneous hydrolysis of nucleotide residues (depurination/depyrimidination), resulting in abasic sites (**1**, Figure 1.1). These are very base-labile and can continue to fragment, in a spontaneous fashion, to form cytotoxic single-strand breaks. Spontaneous or induced deamination of cytosine, adenine, guanine or 5-methylcytosine converts the bases to the miscoding uracil (**2**), hypoxanthine, xanthine and thymine, respectively [1].

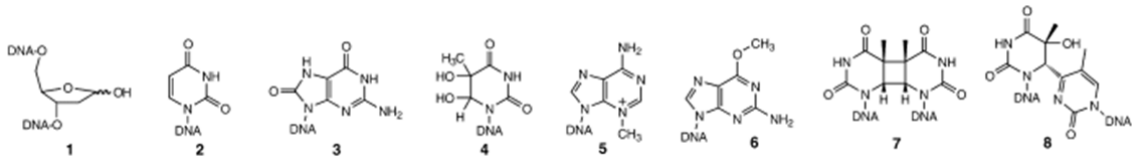

Figure 1.1 | Examples of common lesions to DNA. Abasic sites (**1**) and uracil (**2**) arise from hydrolysis; oxidative damage results in the formation of 8-oxoguanine (**3**) and thymine glycol (**4**); methylating agents form, among others, 3-methyladenine (**5**) and O^6-methylguanine (**6**). UV radiation induces the formation of photoadducts such as the cyclobutane pyrimidine dimers (CPD, **7**) and (6-4) photoadducts (**8**). Adapted from [2].

Second, the products of our own metabolism – byprodutcs – can have harmful effects on DNA. Enzymatic reactions have an error rate, and their reaction products include free radicals, such as reactive oxygen species (ROS) and reactive nitrogen species (RNS), products of lipid peroxidation (oxidation of polyunsaturated fatty acids in lipids) and endogenous alkylating agents [3]. ROS, such as superoxide anions, hydroxyl radicals and hydrogen peroxide, are a natural byproduct of the normal metabolism of oxygen [2]; however, exposure to environmental stress (e.g., UV or heat exposure), may increase ROS levels dramatically, leading to a condition known as oxidative stress. The most prominent oxidative base adducts include mutagenic 8-oxoguanine (**3**) and thymine glycol (**4**), which can block DNA transcription and replication. Cofactors of enzymatic reaction can accidently methylate DNA to form the relative harmless 7-methylguanine, cytotoxic 3-methyladenine (**5**) and the mutagenic and cytotoxic O^6-methylguanine (**6**) [2].

In addition to lesions arising from normal cellular metabolism, there are numerous exogenous sources of damage. Harmful environmental agents include ultraviolet (UV) components of sunlight, ionizing radiation and genotoxic chemicals, such as cigarette smoke, alcohol or biocides and pesticides [3–5]. For many organisms, including humans, one of the most important environmental mutagen is the UV radiation. This type of radiation also lead to the formation of dipyrimidine photoadducts, principally cyclobutane pyrimidine dimers (CPD, **7**) and (6-4) photoadducts (**8**) [6]. Furthermore, excess of UV radiation can lead to ROS formation, as aforementioned.

1.1.2 Damage to the DNA backbone and Interstrand Crosslinks

This type of injury occurs mostly through oxidation of the deoxyribose sugar, whose hydrogen atoms are highly reactive toward ROS. The primary products of these fragmentations are single-strand breaks (SSBs) (**1**, Figure 1.2). On the other hand, double-strand breaks (DSBs) (**2**, Figure 1.2) are induced by ionizing radiation, X-rays and chemotherapeutic drugs. DSBs can also occur during replication of SSBs and repair of interstrand crosslinks (ICLs) [2–4]. ICLs are highly cytotoxic because they block all processes that necessitate the separation of the two DNA strands (e.g., DNA replication and transcription) [2].

Figure 1.2 | ROS, ionizing radiation, X-rays and chemotherapeutic drugs are examples of agents that fragment deoxyribose sugars in DNA. These fragmentations lead to the formation of single- (SSBs, **1**) and double-strand breaks (DSBs, **2**). Adapted from [2].

The outcome of DNA damage is diverse and generally adverse. Some lesions are primarily mutagenic, others mainly cytotoxic and cytostatic [3]. While acute effects, such as inhibition of transcription and replication, trigger cell-cycle arrest or cell death (apoptosis), long-term effects, namely irreversible mutations and chromosome aberrations, lead to ageing and oncogenesis [4]. As stated before, many lesions block transcription and can also interfere with DNA replication. Figure 1.3 provides an overview of the most important agents that cause DNA damage, the lesions formed, and the repair pathways employed to remove these lesions from DNA.

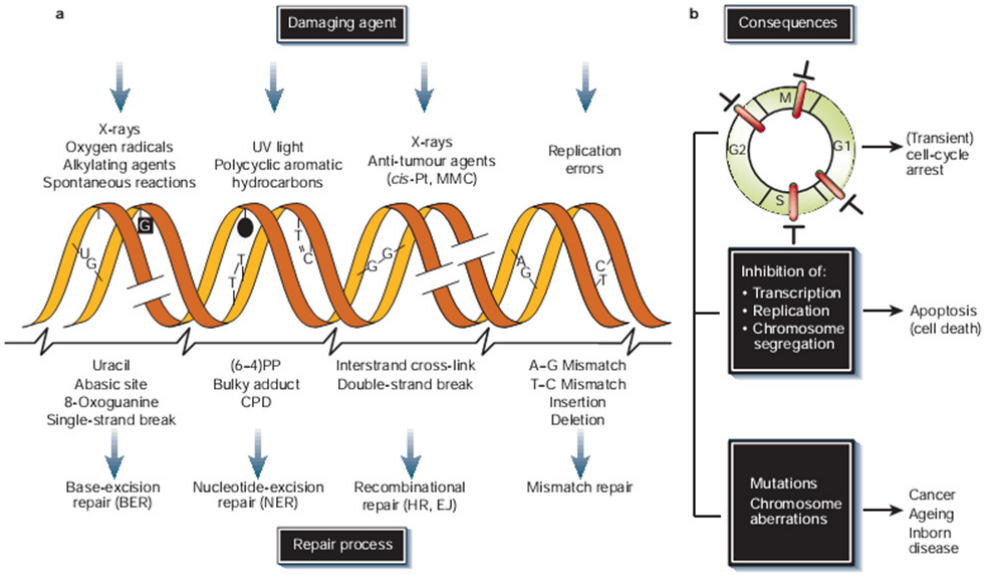

Figure 1.3 | DNA damage and repair mechanisms. **a)** Damaging agents (both of endogenous and exogenous nature) cause DNA lesions that are counteract by lesion-specific DNA repair systems; **b)** Acute effects arising from DNA damage can trigger cell-cycle arrest or inhibition of DNA metabolism, which in turn can lead to apoptosis. On the other hand, long-term consequences of DNA injury can lead to ageing or oncogenesis. Abbreviations: *cis*-Pt and MMC, cisplatin and mitomycin C, respectively (both DNA-crosslinking agents); (6–4)PP and CPD, (6–4) photoproduct and cyclobutane pyrimidine dimer, respectively (both induced by UV light); HR, homologous recombination; EJ, end joining [4].

1.2 DNA repair systems

As a consequence of the diversity of DNA injuries, cells have developed a sophisticated DNA maintenance apparatus, consisting of different repair systems (Figure 1.3). Although each system focus on a specific category of DNA lesion, as a whole they counteract most of the potentially mutagenic and cytotoxic lesions in order to re-establish the correct genome structure [3, 4]. DNA damage causes a temporary arrest of cell-cycle progression, allowing repair to take place prior to replication [7]. No correction procedure is going to be absolutely exact and error-free, but repair of common DNA lesions clearly demands highly accurate performance [6]. The main, partly overlapping, DNA repair systems operating in mammals are direct repair (DR), base excision repair (BER), nucleotide excision repair (NER), mismatch repair (MMR), homologous recombination (HR) and non-homologous end joining (NHEJ) [4]. The first two systems are rather simple in molecular terms and their mechanisms have already been described in some detail; in contrast, the others are more complex repair pathways that are not yet fully understood [2].

1.2.1 Direct repair

Some single repair proteins directly revert certain injuries, such as O^6-methylguanine methyltransferase, which removes the miscoding alkylation lesion O^6-methylguanine. This highly

mutagenic lesion pairs with both C or T and is capable of fooling the mismatch repair system into triggering futile rounds of mismatch removal and subsequent reincorporation of the erroneous base by repair replication. The specific methyltransferase flips out the methylated nucleoside from DNA, accommodates it in its active-site pocket, removes the deleterious non-native methyl group from the guanine residue and transfers it to an internal cysteine. However, *S*-methylcysteine is chemically very stable, so the protein irreversibly inactivates itself. This illustrates how in some situations an entire protein may be sacrificed for the repair of a single damaged base [3, 6].

1.2.2 Homologous recombination and Non-homologous end joining

HR is a highly complex and accurate pathway that uses an intact homologous DNA molecule as a template to repair a DSB. NHEJ is a relatively simple and not so accurate system that involves the re-ligation of broken DNA ends and does not require a homologous template [2] (Figure 1.4).

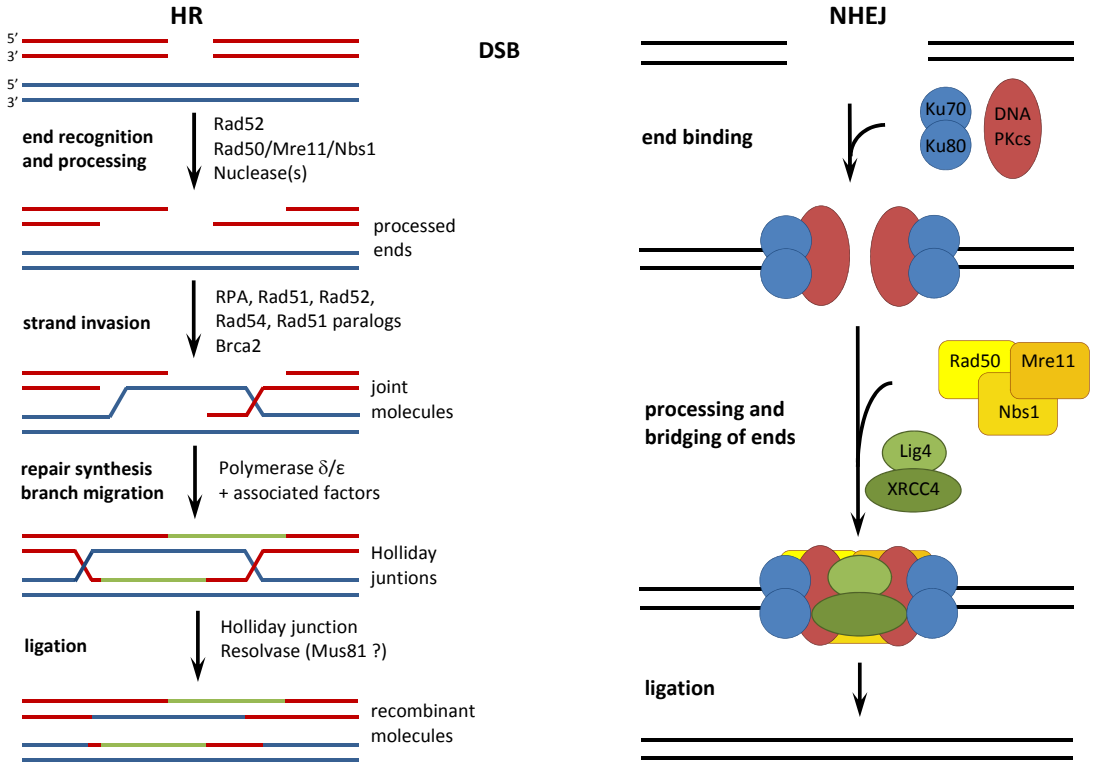

Figure 1.4 | Homologous recombination (HR) and non-homologous end joining (NHEJ) repair systems. HR is initiated by the recognition of a DSB by Rad52 protein. To promote strand invasion, the 5'-3' exonuclease activity of the Rad50/Mre11/Nbs1 complex expose both 3' ends. The ssDNA ends are bound by RPA protein. A joint molecule between the damaged (red template) and undamaged DNA (blue template) is generated by a branch migration reaction involving various proteins. DNA polymerases and their associated factors carry out repair synthesis (sequences in green) and Holliday junctions are formed. These are resolved by endonucleolytic cleavage and rejoining in a reaction that may involve the Mus81 protein. In NHEJ mechanism, DSBs are recognized by the Ku70 and Ku80 proteins, which specifically bind to DNA ends and form a complex with the DNA-dependent protein kinase catalytic subunit (DNA-PKCS). The ends of the break may be processed in a step involving Rad50/Mre11/Nbs1 complex. This and XRCC4/DNA ligase IV complexes may be involved in the processing and bridging of the DNA ends. The break is then sealed by XRCC4/DNA ligase IV. Adapted from [2].

1.2.3 Nucleotide excision repair and Mismatch repair

Two of the three DNA excision repair systems that remove most of the damaged or inappropriate bases in DNA are the nucleotide excision repair (NER) and the mismatch repair (MMR).

NER is, probably, the most complicated of the excision repair systems. It deals with the wide class of bulky, helix-distorting lesions that interfere with base pairing and generally obstruct transcription and normal replication. Two NER subpathways exist with partly distinct substrate specificity: global genome NER (GG-NER) surveys the entire genome for distorting injury, and transcription-coupled repair (TCR) deals with damage that blocks elongating RNA polymerases [2 , 4, 6]. On the other hand, MMR minimizes replication errors by a systematic survey of newly synthesized strands. It removes nucleotides mispaired by DNA polymerases and insertion/deletion (ranging from one to ten or more bases) that result from slippage during replication or recombination [4] (Figure 1.5).

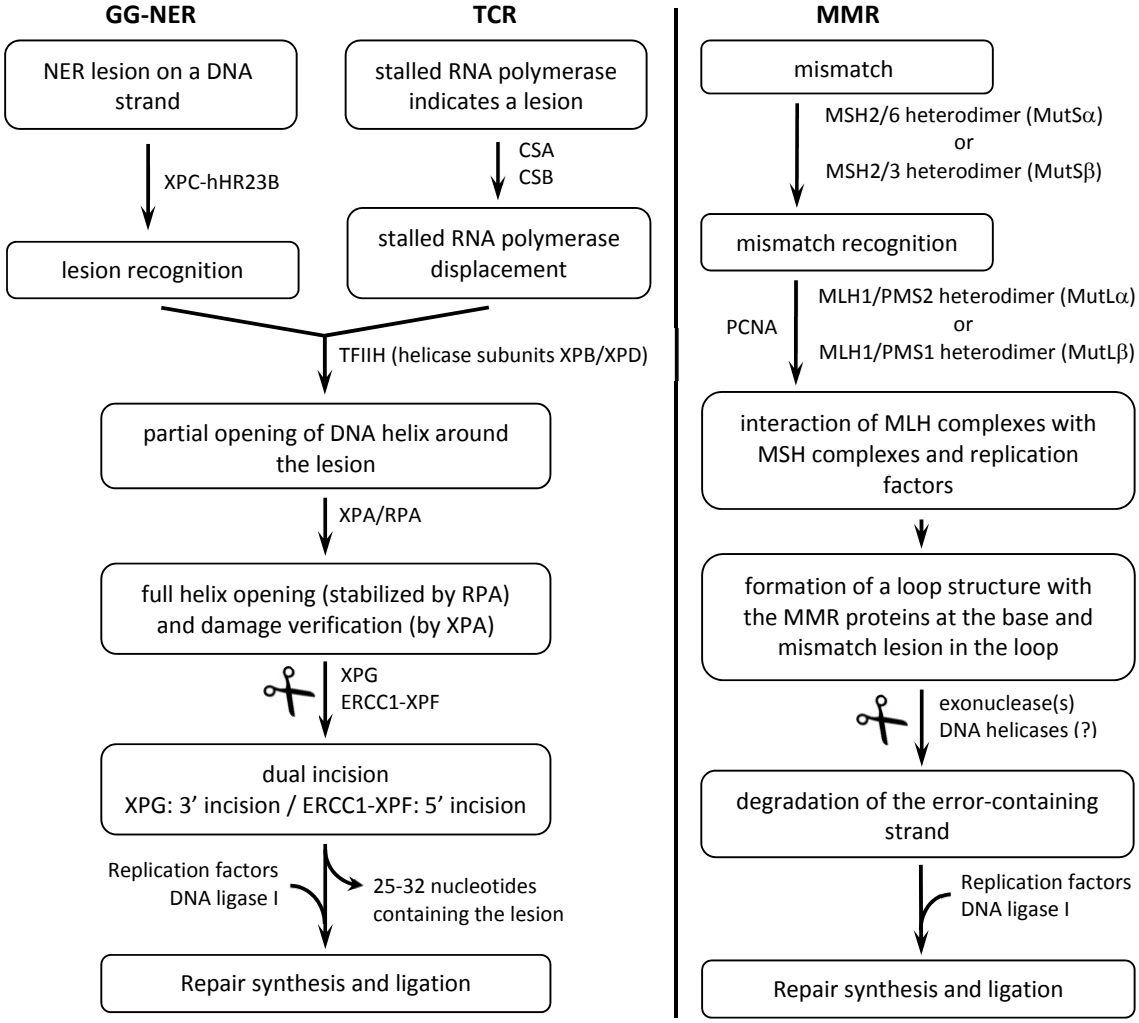

Figure 1.5 | Nucleotide excision repair (NER) and mismatch repair (MMR) systems.

1.2.4 Base excision repair

The other mechanism belonging to DNA excision repair systems is the base excision repair. This system will be explained in much more detail because one of its core components is the subject of study in this thesis.

BER removes subtle, non-bulky, DNA lesions through a “cut-and-patch” multistep mechanism that involves the participation of several enzymes. This robust and dynamic repair system is the main guardian against damage due to cellular metabolism, which includes oxidative lesions, methylation, deamination and hydroxylation products, spontaneous hydrolysis, and different kinds of single-strand breaks [1, 3, 4, 8]. These injuries may or may not impede transcription and replication, although they frequently miscode; BER is therefore particularly relevant for preventing mutagenesis [4]. BER is also one of the major systems that repair oxidative DNA damage caused by ROS (arising from ionizing radiation), to both purines and pyrimidines [7]. Compared with other DNA repair systems, BER is highly conserved from bacteria to human in terms of the core components of its machinery, for example, at the level of DNA glycosylases, key initiators of this repair system [5, 9, 10].

BER occurs in two overall steps and requires the coordinated action of only four enzymes: a DNA glycosylase, followed by apurinic/apyrimidinic (AP) endonuclease (APE1), DNA polymerase β and DNA ligase. The first step in this cascade, damage-specific recognition and excision, is carried out by one of many DNA glycosylases that recognize damaged or mismatched bases and excise them from DNA. The second, a damage-general processing, is accomplished by the three early mentioned downstream enzymes that carry out strand incision, gap-filling and ligation, respectively [8, 10–12].

DNA glycosylases have a facilitated diffusion along the minor groove of DNA, which allows them to efficiently detect damaged bases in the context of an enormous background of normal bases [5, 6, 10]. Upon lesion recognition, they bind to the minor groove, flip the abnormal base out of the DNA major groove by DNA backbone compression to accommodate it in their active site that contains a recognition pocket [5, 6, 11, 12]. Each DNA glycosylase is programmed via its structure to recognize and act upon a particular lesion or group of lesions, so only bases that can be accommodated in a defined binding pocket upon nucleotide flipping provide the necessary contacts and orientation for base excision [5, 13]. In this recognition pocket, the damaged base is hydrolytically excised by cleavage of the *N*-glycosidic bond between the sugar phosphate backbone and the base, leaving an AP site (**I**, Figure 1.6) [7, 12]. These AP sites can also occur spontaneously by hydrolysis (**II**) [4]. DNA glycosylases have high affinity for their products, AP sites, and are likely to remain clamp to them until displaced by the second enzyme in the BER pathway, the endonuclease APE1, which has also greater affinity for the AP residues. This strategy is a safety mechanism, because if left unrepaired,

AP sites can be more cytotoxic and mutagenic than base lesions [1, 2, 6, 11]. When bound to DNA, APE1 hydrolyses the phosphodiester bond 5' to the AP site to generate a nick (**III**). Then, this enzyme interacts and recruits to the site of repair the next enzyme in the BER pathway, polymerase β (pol β) [6]. In mammals, the so-called short-patch repair is the dominant mode for the remainder of the reaction. In this main pathway, DNA pol β performs a one-nucleotide gap-filling reaction in the newly generated 3'-OH (**IV**) and excises the 5'-terminal abasic sugar-phosphate residue at the strand break via its AP lyase activity (**V**) [4]. The nick in DNA is then sealed by DNA ligase III, restoring the integrity of the helix [2]. DNA ligase forms a heterodimer with the non-catalytic XRCC1 protein (**VI**) and since pol β also interacts with it, this subunit acts as a scaffold protein by bringing the polymerase and ligase together at the site of repair; further stabilization of the complex may be achieved by direct binding of the NH_2-terminal region of XRCC1 to the DNA single-strand break [6–8].

A minor pathway of BER, the long-patch repair, may instead occur in cases where the terminal sugar-phosphate residue has a more complex structure that is relatively resistant to cleavage by the AP lyase function of pol β. This minor pathway relies on DNA polimerases δ or ε that incorporate 2–10 nucleotides after the AP site (**VII**) and the proliferating cell nuclear antigen (PCNA), a replication factor that acts as a DNA polymerase clamp, hence enhancing the activity of DNA pol δ/ε. The flap structure-specific endonuclease (FEN-1) binds PCNA and excises the displaced DNA flap (**VIII**). In this context, FEN-1 binding to PCNA stimulates FEN-1 endonuclease activity. Taken together, these findings suggest that PCNA promotes long-patch BER via its ability to interact with and coordinate the enzymatic activities of a DNA polymerase and endonuclease FEN-1. Therefore, PCNA acts as a scaffold protein in this alternative pathway in a way similar to that of XRCC1 in the main pathway. Finally, the last step in this minor pathway is the nick sealing by DNA ligase I (**IX**) [6, 8, 10, 14].

As described before, ROS and some exogenous agents, such as X-rays, can cause SSBs by destruction of deoxyribose residues. Such damages are processed and repaired by the same enzymes that are responsible for the later stages of BER. An abundant nuclear protein, poly(ADP-ribose) polymerase (PARP), which binds to and is activated by DNA strand breaks, and the recently identified polynucleotide kinase (PNK) (**X**) may be important when BER is initiated from a SSB to temporary protect and trim the ends for repair synthesis, acting as antirecombinogenic factors. PARP, as pol β and ligase III, interacts with the scaffold protein XRCC1 and may in this way accelerate the recruitment of these enzymes to the site of repair [4, 6].

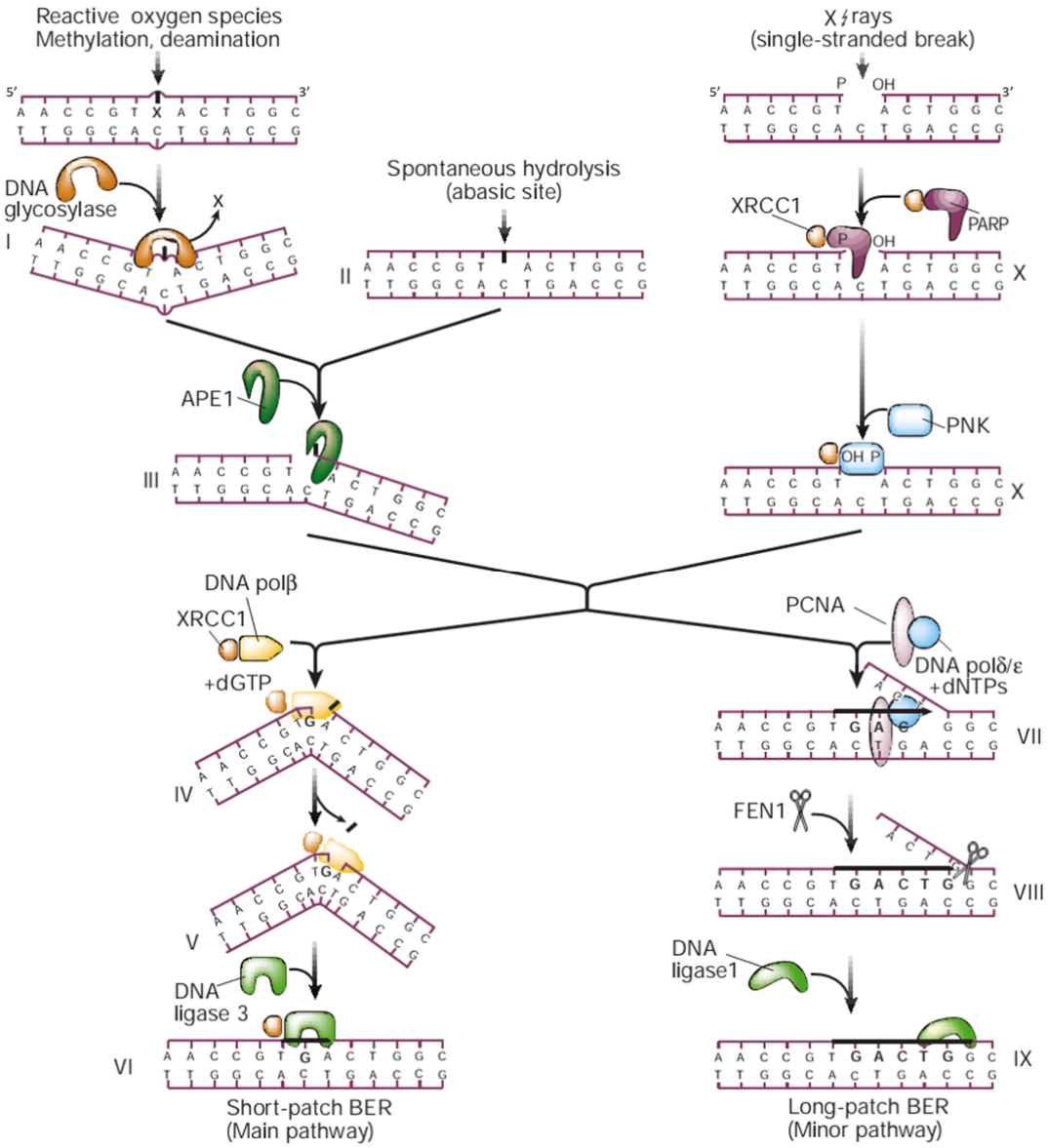

Figure 1.6 | Overview of base excision repair (BER) mechanism, with both short- (left) and long-patch (right) repair pathways. SSB repair system is also shown. Adapted from [4].

Although individual enzymes mediate each step in BER, the pairwise interactions between them indicated that this is a highly coordinated process, which ensures smooth repair of both abasic sites and strand-break intermediates, that are by themselves highly toxic and mutagenic [2, 9].

1.2.4.1 DNA glycosylases

As aforementioned, the key initiators of the BER system are DNA glycosylases, highly efficient enzymes that recognize and excise damaged bases. Although all DNA glycosylases cleave glycosidic bonds, they differ in their reaction mechanisms [15]. Indeed, these enzymes fall into two mechanistic classes: pure monofunctional glycosylases and bifunctional *N*-glycosylases (base excision)/AP lyases (strand nicking). As seen in Figure 1.7, the former use a water molecule as a nucleophile to cleave the *N*-glycosidic bond, leaving an AP site, which will be processed by an enzyme with AP lyase activity, such as APE1. The latter use an amino group (lysine residue) of the enzyme as a nucleophile for cleavage. This generates a covalent intermediate (Schiff base), which can undergo a β-elimination (associated AP lyase activity), leading to cleavage of the C3'-O bond and strand scission [2, 7, 13]. In this case, pol β lyase activity is not required [2].

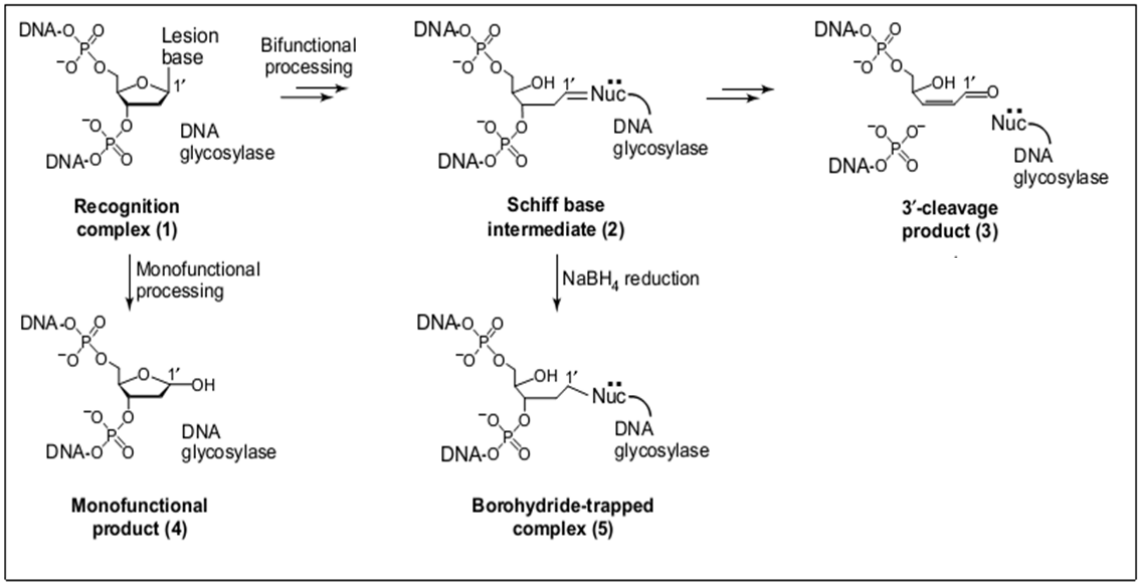

Figure 1.7 | Reaction mechanism of DNA glycosylases. First, DNA glycosylases recognize a base damage and bind to it (**1**). Monofunctional DNA glycosylases use a water molecule as a nucleophile, which attacks the C1' of the target nucleotide, leaving an AP site (**4**). In the case of bifunctional glycosylases, the nucleophilic attack involves an amino group (lysine residue) of the enzyme (Nuc) and the reaction yields a covalent intermediate (Schiff base) formed by the enzyme and C1' of the target nucleotide (**2**), thus expelling the damaged base. Additional reactions catalyzed by this enzyme leads to Schiff base β-elimination, resulting in C3'-O bond cleavage (**3**). Schiff base intermediate (**2**) can be reduced by sodium borohydride ($NaBH_4$), resulting in a stable, covalently "trapped" protein–DNA adduct (**5**), which has been used in various structural studies ([16] and references therein). Adapted from [13].

Most DNA glycosylases remove structurally different bases, while a few have very narrow substrate specificity. This information was obtained by cloning and characterization of several DNA glycosylases, including eleven distinct human DNA glycosylases (Table 1.1).

Table 1.1 | Human base excision repair DNA glycosylases, their substrate specificity and their homologous in other species. Adapted from [8, 9, 17].

Enzyme	Homologous in other species		Substrate specificity	AP lyase function
	E. coli	*S. cerevisiae*		
hUNG	ung	UNG1	U, 5-OH-U in ss/dsDNA	no
hSMUG1	-	-	U, 5-OH-U in ssDNA	no
hTDG	mug	-	U:G, T:G, εC	no
hMBD4	-	-	U:G, T:G in CpG sequences	no
hOGG1	fpg	OGG1, OGG2	8-oxoG:C, fapyG	yes
hMYH	mutY	-	A:G, A:8-oxoG	no
hNTH1	Endo III (nth)	NTG1, NTG2	Tg, Cg, fapyG, oxidized pyrimidines	yes
hNEIL1	nei	-	as NTH1 and fapyA, 8-oxoG	yes
hNEIL2	-	-	overlap with NTH1/NEIL1	yes
hNEIL3	-	-	unknown	?
hAAG (MPG)	alkA/tag	MAG1	3-MeA, 7-MeG, εA, Hx	no

Abbreviations: εC: 3,N^4-ethenocytosine; 8-oxoG: 8-oxoguanine; fapy: formamidiopyrimidine; Tg: thymine glycol; Cg: cytosine glycol; 3-meA: 3-methyladenine; 7-meG: 7-methylguanine; εA: 1,N^6-ethenoadenine; Hx: hypoxanthine.

Among the monofunctional glycosylases are hUNG, hTDG, hSMUG1, hMBD4 and hMPG. The first four of them display activity against bases that arise through deamination of C and/or 5-meC residues, whereas hMPG acts on alkylated bases. The bifunctional enzymes are hOGG1, hNTH1 and hNEIL (1 and 2), which together with the monofunctional hMYH deal principally with DNA bases damaged by active oxygen species. hOGG1 and hMYH counteract the mutagenic effect of 8-oxoguanine,the most frequent form of oxidative base damage, whereas oxidized pyrimidines such as thymine glycols are excised by the hNTH1 and hNEIL (1 and 2) glycosylases [9].

1.2.4.2 HhH superfamily

Structural studies revealed that DNA glycosylases fall into three main structural superfamilies that share little amino acid sequence homology between them [5, 13, 17]. The largest and most diverse of them, HhH superfamily, was founded with *E. coli* Endonuclease III (Endo III), whose crystal structure was the first to be fully characterized [18]. This superfamily includes glycosylases such as hOOG1, hMYH and hNTH1, along with a number of enzymes from other organisms (e.g. AlkA and MutY) [9]. The crystal structure of some of these proteins revealed that they consist of at least two α-helical domains (three, in the case of MutY and hOOG1). One of them typically has four α-helices, whereas the other is a six-helix barrel [10, 17]. The overall structure contains a conserved central α-helical motif, located near the cleft between the two domains that is common to the members of this family (Figure 1.8). The hallmark is a helix-hairpin-helix (HhH) motif, with a consensus sequence, followed at a specific distance by a Gly/Pro-rich loop (GPD motif) which contains a highly conserved catalytic Asp residue, as originally discovered for Endo III [19].

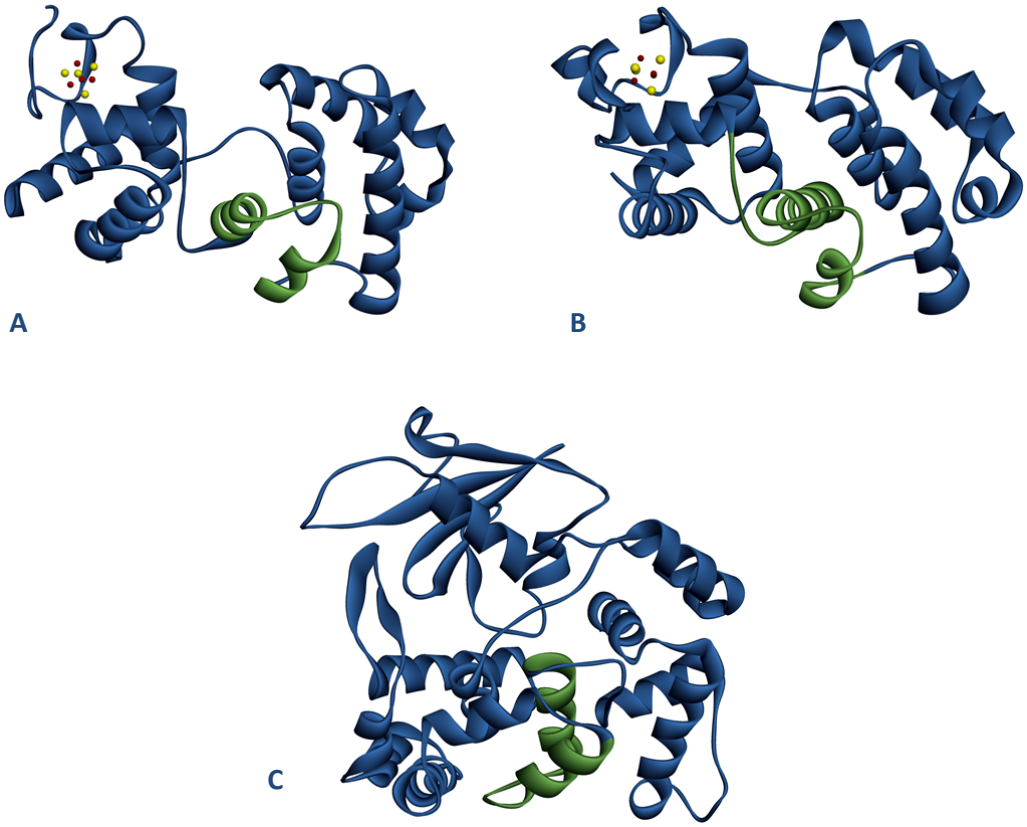

Figure 1.8 | Comparison of the three-dimensional structures of some enzymes belonging to the HhH DNA glycosylase superfamily. **A** – Endo III (PDB ID 2ABK), **B** – MutY (PDB ID 1KG2), **C** – hOGG1 (PDB ID 1KO9). The conserved HhH-GPD motif is shown in green. Figures were made using Accelrys DS Visualizer software (v3.5.0.12158), available at http://accelrys.com/.

In bifunctional DNA glycosylases, the conserved Asp in the GPD region is thought to protrude into the cleft, which is the active site of these enzymes, and deprotonate the ε-NH_3^+ group of a conserved Lys residue of HhH motif, forming an amine nucleophile that attacks the glycosidic bond [5, 7]. Instead, in monofunctional DNA glycosylases this conserved Asp residue may activate a water molecule which acts as the attacking nucleophile [7], as described in Figure 1.7.

The HhH motif is not directly involved in nucleotide flipping, but rather in the positioning of the enzyme next to the lesion [9, 16]. HhH is, therefore, considered a sequence-independent DNA binding motif [19]. Structural studies on Endo III-DNA complex have shown that the HhH motif participate in DNA recognition through interaction with phosphate and oxygen atoms of the DNA backbone [16].

Glycosylases of HhH superfamily share yet another important feature, a cubane [4Fe-4S] cluster, as first structurally characterized in Endo III [16, 18–22] and also found in MutY [23]. The same structural studies revealed a solvent-exposed loop near the cluster, termed the iron-sulfur cluster loop (FCL) motif (Figure 1.9).

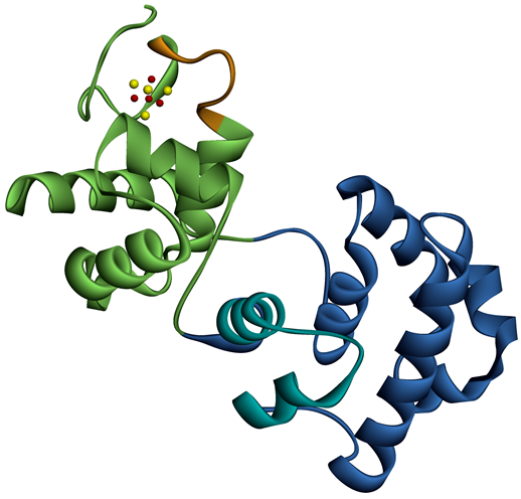

Figure 1.9 | HhH superfamily motifs represented in *E. coli* Endo III (PDB ID 2ABK). The six-helix barrel domain (dark blue) contains the HhH motif (light blue). The [4Fe-4S] cluster domain (green) contains the [4Fe-4S] cluster (red and yellow spheres, corresponding to the iron and sulfur atoms, respectively) and the FCL motif (orange) [19]. The figure was made using Accelrys DS Visualizer software (v3.5.0.12158), available at http://accelrys.com/.

1.2.4.3 Endonuclease III

As described above, one of the ubiquitous enzymes belonging to BER system is Endo III. The gene that encodes Endo III, *nth*, is a highly conserved BER gene; homologous of the *nth* gene are found in nearly every organism studied and the sequences of *nth* homologous are well conserved throughout phylogeny (Figure 1.10) [8].

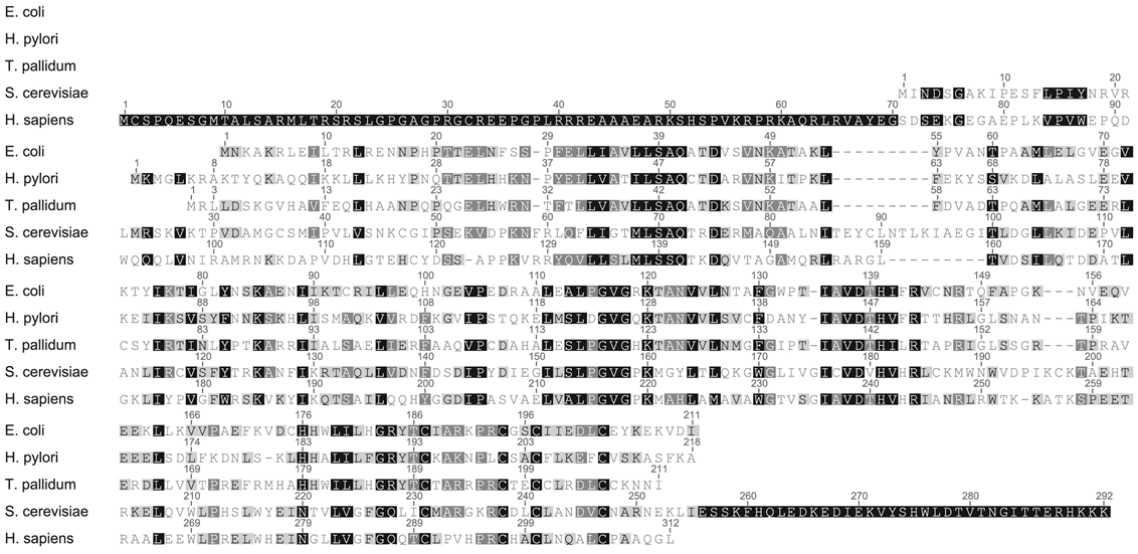

Figure 1.10 | Sequence alignment between nth gene products. HhH-type glycosylases from *E. coli, H. pylori, T. pallidum, S. cerevisiae and H. sapiens* were compared. Black, 100 % homology; dark grey, 80 to 100 % homology; light grey, 60 to 80 % homology; white, less than 60 % homology. Sequence alignment was made using Geneious Basic software [24], available at http://www.geneious.com/.

Endo III was first identified in *E. coli* as an endonuclease, based on its ability to generate SSBs in UV-irradiated dsDNA [25]. Studies on purified Endo III revealed that it is in fact a bifunctional DNA *N*-glycosylase/AP lyase, and thus can remove certain modified DNA bases and cleave the DNA backbone 3' to AP sites via the β-elimination mechanism. Substrates for glycosylase function of Endo III and its human homologue, hNTH1, consist of pyrimidines damaged by ring saturation, contraction or fragmentation (e.g. thymine glycol), generated by exposure to UV light, ionizing radiation, and oxidative stress [15, 16, 26].

The 23.6 kDa protein (211 amino acids) [27] is elongated and bilobal, with primarily α-helical secondary structure. As stated above, a central deep cleft separates two globular domains, a continuous six-α-helix barrel domain and a four α-helix one, the [4Fe-4S] cluster domain. The [4Fe-4S] cluster is held in place by an array of hydrogen bonds made with four conserved Cys residues, in the C-terminus [7, 18, 19]. The two domains lie astride the DNA duplex, with the lesion-containing strand sandwiched between them (Figure 1.11).

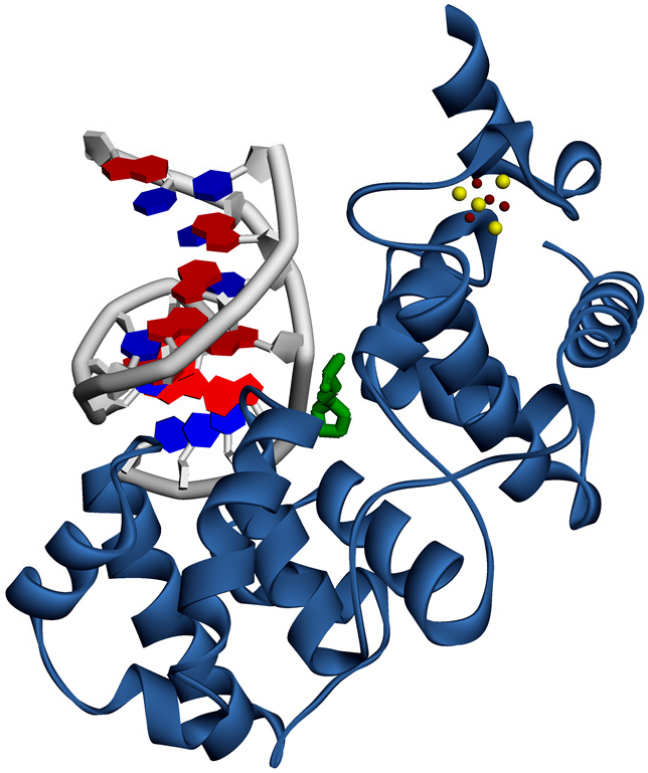

Figure 1.11 | Crystal structure of *Geobacillus stearothermophilus* Endo III bound to DNA containing an abasic site (PDB ID 1P59). The lesion is shown in green. The [4Fe–4S] cluster can be seen as red and yellow spheres, corresponding to the iron and sulfur atoms, respectively [16]. The figure was made using Accelrys DS Visualizer software (v3.5.0.12158), available at http://accelrys.com/.

1.2.4.4 Iron-sulfur clusters

There are two distinct types of cubane [4Fe-4S] cluster-containing electron-transport proteins that differ in their observed redox potentials. The ferredoxins (Fds) exhibit redox potentials of -100 to -650 mV whereas "high-potential" iron proteins (HiPiPs) exhibit midpoint potentials ranging from +50 to +450 mV [28–30]. This was explained by the three-state hypothesis of Carter [31], in which the protein environment stabilizes the $[4Fe\text{-}4S]^{3+/2+}$ or $[4Fe\text{-}4S]^{2+/1+}$ redox couple in HiPiP and Fd enzymes, respectively. In both cases, the resting state of the enzyme contains a $[4Fe\text{-}4S]^{2+}$ cluster.

A structural role for the cluster in Endo III was accepted on the basis of *in vitro* work that showed the cluster to be resistant to reduction and oxidation, in solution [20, 22]. Combination of kinetic, mutagenic and structural studies on *E. coli* MutY (a DNA glycosylase similar to Endo III), have shown that although the iron-sulfur cluster does not contribute significantly to the folding and stability of the protein, it is essential for DNA binding and catalysis [23]. This idea is consistent with structural studies on Endo III and MutY, which revealed a solvent-exposed [4Fe-4S] cluster loop formed by the first two cysteine ligands, FCL motif. This loop contains a high density of positively charged residues that are perfectly positioned to interact with the anionic DNA backbone. It extends from the cluster, protrudes into the minor groove of DNA and interacts with the HhH motif, aiding in DNA binding and damage recognition [5, 19, 29]. Other studies were made to probe the functional value of the cluster, by individually replacing the cysteine ligands of MutY with alanine, serine and histidine. Most of the modified proteins were unstable to overexpression, suggesting the need for a fully coordinated $[4Fe\text{-}4S]^{2+}$ cluster for the *in vivo* stability of the enzyme [29].

1.2.4.5 Iron-sulfur clusters and DNA-mediated charge transport: a facilitated route for DNA repair

A redox function for the clusters in BER glycosylases was unclear because redox activity in the physiological range of potentials was not found [20]. The $[4Fe\text{-}4S]^{2+}$ cluster is well separated from the enzyme active site and do not appear to participate in the glycosylase reaction. This cofactor is required for non-specific DNA binding and, thus, is essential for overall repair activity. Crystal structures in the absence and presence of DNA, moreover, reveal that the cluster is located near amino acid residues that contact DNA, as already mentioned. DNA binding significantly changes the environment of the cluster, taking the cluster loop from a relatively exposed polar environment to a more hydrophobic one near the DNA groove [16, 32–34]. The accumulating data indicating that the region around the $[4Fe\text{-}4S]^{2+}$ cluster contacts DNA hinted that the redox properties of the cluster may be modulated by the presence of DNA. Indeed, electrochemistry studies by cyclic voltammetry, both with MutY and Endo III bound to DNA-modified gold electrodes, demonstrated that they are redox-

active at physiological potentials, displaying stable, reversible signals with respective midpoints potentials of 90 and 58 mV *vs.* NHE, characteristic of HiPiPs. Scan rate dependence measurements show a linear relationship between the peak current and the square root of the scan rate, an indication of a diffusion-limited process. However, measurements of electron transfer rates indicate a relatively slow electronic transfer. The authors also state that in the absence of DNA modification of the electrode, no redox activity can be detected [34–36]. Thus, although resistant to oxidation and reduction in solution, binding to DNA shifts the redox potential of the enzyme, allowing its transition to the +3 state, consequently activating the enzyme [32, 34, 36].

On the basis of this DNA-mediated redox behavior, a model using DNA-mediated charge transport (CT) between DNA repair enzymes was proposed, given that DNA-mediated CT chemistry is highly sensitive to a wide variety of lesions that disrupt DNA base stacking, such as abasic sites or damage and mismatched bases [34, 36, 37]. As illustrated in Figure 1.12, DNA-mediated CT is sharply attenuated by the presence of any of the mentioned lesions.

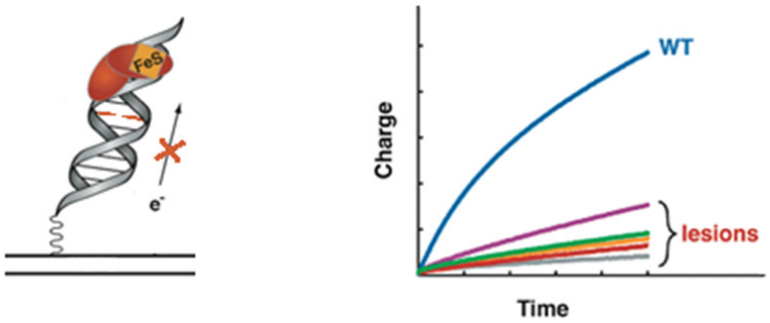

Figure 1.12 | DNA-mediated CT is attenuated by the presence of an abasic site or other lesions that affect dynamic stacking. Right side of the figure: illustrative graphic of the DNA-mediated CT attenuation when in the presence of a lesion (WT, wild-type). Adapted from [33, 37].

Therefore, DNA repair glycosylases can exploit DNA-mediated CT as a way to rapidly and efficiently search for DNA damaged sites in the genome [29, 36, 38]. DNA-mediated CT chemistry has been probed using biochemical, spectroscopic and electrochemical methods, and data shows that DNA facilitates CT over long molecular distances, owing to the π-stacking of base pairs. The planar, aromatic, hydrophobic, heterocyclic base pairs are stacked upon each other within the helix [37–40]. Crystal structures of both MutY and Endo III place the [4Fe-4S] cluster and DNA roughly ≈ 14 Å apart at their closest, and ≈ 20 Å from both the center of the DNA helix and the glycosylase active site [16, 18, 19, 23, 35]. At this distance, CT could proceed by either a single-step tunneling process or a multistep tunneling process, also called hopping, in which amino acids act as “stepping stones” for the electron as it travels from DNA to and through the protein. Overall, CT mechanism permit charge to travel from the DNA into a bound protein and then through the protein to a redox-active cofactor, such as a [4Fe-4S] cluster [40].

Figure 1.13 illustrates the proposed model for how DNA-mediated CT among BER enzymes may facilitate the detection of DNA lesions.

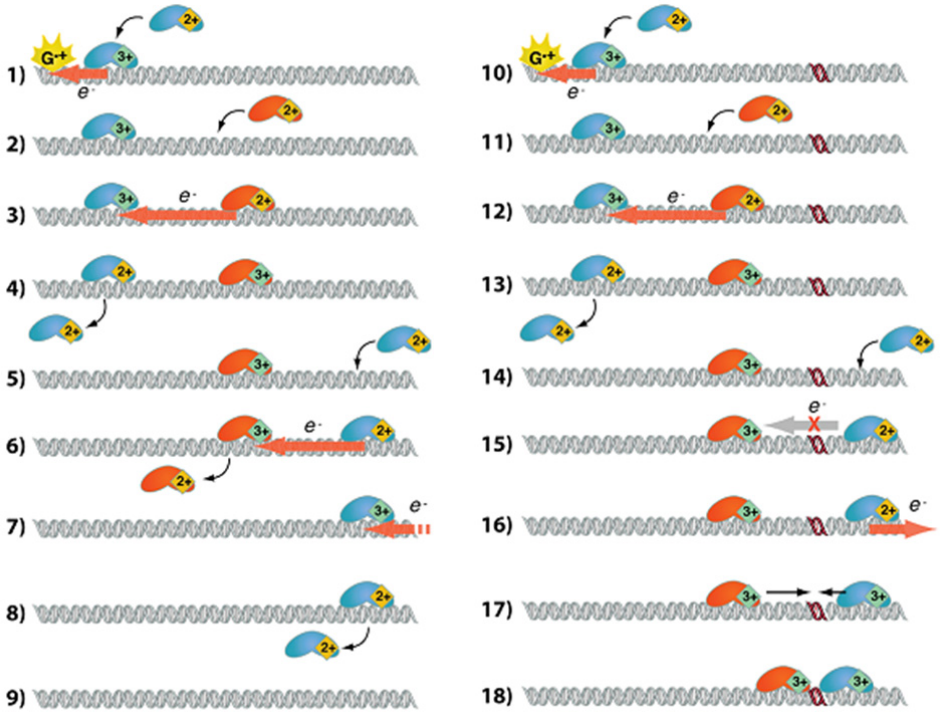

Figure 1.13 | Proposed model for long-range DNA-mediated CT in DNA repair. The orange and blue proteins represent two different Fe-S cluster-containing proteins of similar potential. In this model, guanine cation radical oxidizes a nearby BER Fe-S cluster to the 3+ state (1). Non-specific binding of a reduced protein nearby (2) allows electron transfer (3), following which the first protein, now in the 2+ state, has decreased affinity for DNA and can diffuse away (4). This process is repeated when another reduced protein binds the DNA non-specifically on the other side (5,7), followed by CT and dissociation of the newly reduced protein (6,8). The DNA is left empty of the 3+ bound protein (9). The directionality portrayed in (1-9) is illustrative, as the DNA-mediated CT is diffusive. When a lesion is present, steps 10-14 mirror steps 1-5. Reduced protein distal to the lesion, however, is unable to reduce the oxidized protein through DNA-mediated CT (15), which remains bound do DNA near the lesion. DNA-mediated CT, as shown in the previous steps, can oxidize a reduced protein on the distal side of the lesion (16), and protein in 3+ state accumulated near the lesion can processively diffuse along the DNA (17) and repair the lesion upon direct contact (18) [37].

Within the cell, the iron-sulfur clusters of BER glycosylases are in the $[4Fe\text{-}4S]^{2+}$ state. On binding DNA in a non-specific fashion, the enzyme undergoes a shift in redox potential, which allows its transition to the 3+ state by cellular oxidants, including guanine radicals. If the surrounding genome is free of damage or mismatched bases, this enzyme can be reduced, via DNA-mediated CT, by a distally non-specifically bound redox-active glycosylase of similar reduction potential. The reduction of the first enzyme favors its dissociation from DNA and relocation to another site, since the 2+ state has decreased affinity for DNA. Thus, this method serves as a scanning mechanism for the repair glycosylases in search for damaged or mismatched bases. If a damaged site is present, it short-circuits this DNA-mediated charge-transfer process and the oxidized repair proteins do not suffer

reduction. Thus, they remain bound to DNA in the vicinity of the lesion site and processively diffuse toward it on a longer time scale, in order to fix the lesion. Hence, DNA CT provides a rapid strategy to redistribute DNA repair proteins onto regions of the genome containing lesions [29, 32, 34, 36–38, 41, 42].

Importantly, the first step of this damage detection method requires oxidation of DNA-bound Fe-S cluster repair enzymes. Studies indicate that guanine radical cations, cellular oxidants which are formed under conditions of oxidative stress, can promote oxidation of the $[4Fe\text{-}4S]^{2+}$ cluster of DNA glycosylases through DNA-mediated CT. Hence, they can be ‘‘repaired’’ directly through DNA-mediated electron transfer from the repair protein. Significantly, protein oxidation through this process serves further to drive the redistribution of DNA repair proteins on genomic sites, preferentially onto sites near lesions. Thus, guanine radicals can provide the driving force *in vivo* to trigger a DNA-mediated CT signaling cascade and, consequently, DNA repair [42].

Significantly, recent studies indicate that MutY and Endo III engage in a cooperative functional relationship in their search for damage in the genome and redistribute in the vicinity of lesions, which is another important feature of the DNA-mediated CT damage detection model. Due to the similarity in redox potentials measured for these enzymes (within ≈ 30 mV range), electrons may transfer between them and, in this process, information about the integrity of the surrounding DNA is transmitted. This provides a further explanation for the low copy number yet high *in vivo* effectiveness of BER enzymes. This cooperation, or helper function, does not involve the glycosylase specific reaction and arises from a distance; what does appear to be required for helper function is an intact [4Fe-4S] cluster as well as an electroactive protein-DNA interface [37, 41].

Figure 1.14 illustrates the type of methodology used in the electrochemical studies of Endo III on highly oriented pyrolytic graphite (HOPG) electrodes, which allowed for the direct comparison of the electrochemistry of Endo III in the absence and presence of DNA [33].

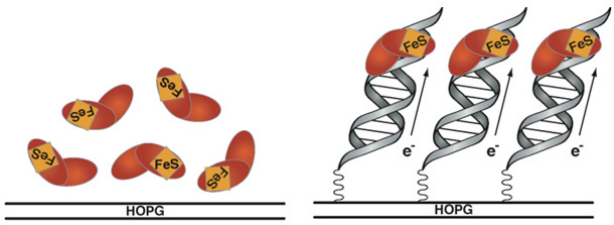

Figure 1.14 | Schematic representation of the type of methodology used in the electrochemical studies of Endo III on HOPG, with and without electrode DNA-modification [33].

Figure 1.15 shows cyclic voltammograms of Endo III with DNA modification. According to Gorodetsky *et al,* the only observed redox signal in the range of 600 mV to -400 mV *vs.* NHE is a quasi-reversible redox couple with a midpoint potential of 20 ± 10 mV *vs.* NHE. Although with a large error, the authors observed a cathodic peak at -30 ± 20 mV *vs.* NHE. Moreover, the authors' interpretation is that the system characteristics indicate slow diffusive kinetics, as found in other experiments already mentioned. Indeed, in all respects, this couple resembles that found for Endo III at a DNA-modified gold surface and is assigned to the $[4Fe\text{-}4S]^{3+/2+}$ cluster redox process. To establish that this signal is DNA-mediated and not the result of direct interaction with the electrode surface, experiments were conducted with an electrode modified with DNA featuring an abasic site prepared under identical conditions. As seen in Figure 1.13, a complete loss of signal is observed at the electrode modified with DNA containing an abasic site. Thus, the DNA does not serve to locally concentrate the protein on the graphite surface; the duplex with an abasic site would serve a similar function. Instead, the authors' interpretation according to these results is that DNA-mediated CT through the π-stacking of DNA is required to observe [4Fe-4S] oxidation electrochemically on HOPG [33].

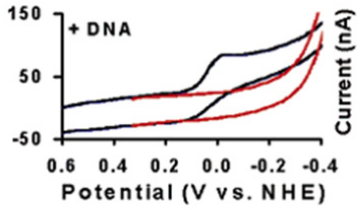

Figure 1.15 | Cyclic voltammetry assays of Endo III on a DNA-modified HOPG electrode. Cyclic voltammetry of an electrode modified with DNA featuring an abasic site is in red. Both runs were taken using the inverted drop cell electrode configuration versus Ag/AgCl reference [33]. Note: *Although missing in the original paper, one should read yy axis as –I.*

Due to its extended potential window, HOPG allows for the study of the electrochemistry of Endo III also in the absence of DNA, a measurement made impossible by the potential window limit on gold [33, 43]. According to Gorodetsky *et al*, oxidative scans of Endo III on bare HOPG reveal an irreversible anodic peak at 250 ± 30 mV *vs.* NHE (Figure 1.16) [33].

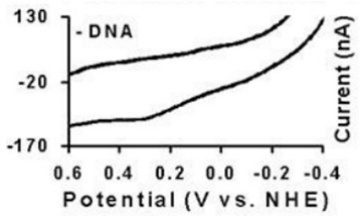

Figure 1.16 | Cyclic voltammetry assays of Endo III on a bare HOPG electrode, using the inverted drop cell electrode configuration versus Ag/AgCl reference [33]. Note: *Although missing in the original paper, one should read yy axis as –I.*

Although not mentioned in the original paper and despite the fact that controls are missing, from observation of Figure 1.16 it seems that a cathodic peak is present around 50 mV *vs*. NHE.

Gorodetsky *et al* stated that successive positive scans lead to new broad, irregular signals at much lower potentials. The authors' interpretation is that these results are consistent with previous observations that oxidation in the absence of DNA (i.e., in solution) leads to decomposition of the Endo III cluster, since these redox signals are commonly associated with [3Fe-4S] clusters [33, 35].

Figure 1.17 summarizes the potentials values that have been determined for Endo III on HOPG, according to Gorodetsky *et al*. Redox potential measurement of both free and bound Endo III on the same surface allowed for the demonstration that binding to DNA shifts the redox potential of the cluster by more than 200 mV in the cathodic direction and stabilizes its $[4Fe\text{-}4S]^{3+}$ state, whereas without DNA it is $[4Fe\text{-}4S]^{2+}$ state that is more stable [33, 43].

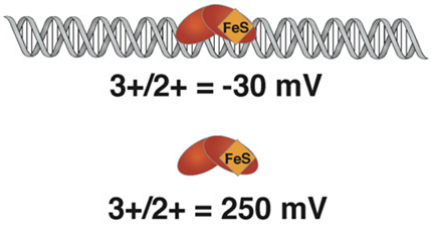

Figure 1.17 | Illustration of the potentials *vs.* NHE for the redox couples of Endo III in the presence and absence of DNA, on HOPG electrode. Adapted from [33].

Notably, the resultant shift in potential is not associated with significant conformational changes in the protein upon binding to DNA; the structures of the bound and free proteins are remarkably similar. Instead, the negative shift of more than 200 mV in potential must correspond to a decrease in DNA binding affinity of more than three orders of magnitude between the 2+ and 3+ forms of the cluster [33]. While previous evidence qualitatively indicated a lessened DNA binding affinity for the reduced protein [34], these data provide a more quantitative estimate. In the context of the described model of DNA-mediated signaling for damage detection, the authors' interpertation is that it is this difference in DNA binding affinity for the reduced *vs.* oxidized state that leads to the dissociation of protein from the DNA upon reduction and thus the redistribution of BER proteins onto sites near damage [33].

Chapter 2 Objectives

Although the effects of UV light, ionizing radiation and oxidative stress on DNA have been extensively studied, very little is known about the effect of these carcinogens on DNA repair enzymes, in particular on the Fe-S containing DNA glycosylases, such as Endonuclease III (Endo III). Although intact DNA repair is essential for a healthy organism, DNA-repair enzymes counteract the efficiency of a number of important antitumor agents (e.g. ionizing radiation, cisplatin, alkylating agents and mitomycin C) that exert their cytotoxic effects by damaging DNA. Thus, selective inhibition of DNA repair enzymes in malignant cells may greatly improve antitumor therapies. Indeed, modulation of DNA damage responses coupled with more conventional radiotherapy and chemotherapy approaches could sensitize cancer cells to treatment. DNA repair enzymes are, therefore, suitable targets for drug design to enhance cancer therapies.

Based on what was stated above, the aim of this thesis is the study of the effect of UV radiation on *E. coli* Endo III, a DNA repair enzyme belonging to BER repair system, that has a human homologous with similar structure. This particular enzyme was chosen due to its ubiquity and because it is the most well characterize [4Fe-4S] cluster-containing DNA glycosylase.

UV-visible spectroscopy and electrochemical methodologies will be used during this project to monitor the integrity and redox state of the [4Fe-4S] cluster, in the absence and presence of DNA, and on non-UV irradiated and UV irradiated samples. Thus, this center will be used to assess the effect of UV radiation in this protein and in its activity.

Endo III, plasmid DNA and protein-DNA complex behavior, before and after exposure to UV radiation, will be assessed both by electrophoresis (SDS-PAGE and agarose gel) and by electrochemical methods.

Chapter 3 *E. coli* cells transformation, homologous overexpression and purification of recombinant Endonuclease III

This chapter aims to present the homologous overexpression and purification steps of recombinant Endonuclease III (Endo III), the DNA repair enzyme to be studied in this work. Endo III was overexpressed both in 2xYT and M9 media, with different purposes. 2xYT was used to express all the proteins used in this work while M9 was used to test the expression system for ^{57}Fe supplementation.

All trademarks not mentioned, instrumentation and protocols used in this chapter are described in the Appendices section.

3.1 Transformation

Before proceeding to transformation, it was necessary to prepare competent *E. coli* cells. The protocol used for this purpose is described in Appendix B.1.

Transformation of chemically competent *E. coli* cells (C43 (DE3) strain) was performed according to the manufacturer protocol (*vide* Appendix B.2.1). These cells were transformed with a pET21c(+) plasmid vector (*Novagen*), which contains the coding gene for the wild type Endo III, pET21c(+)–Endo III (Figure 3.1). This plasmid vector was produced through a ligation reaction performed by a colleague (Daniela Penas) who kindly provided it for this project.

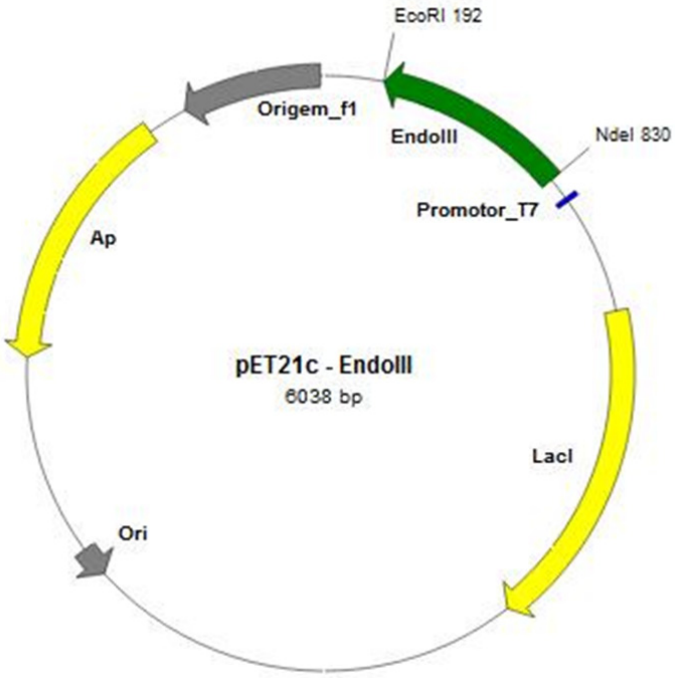

Figure 3.1 | pET21c(+)-Endo III cloning vector map.

Since the aforementioned plasmid vector contains an ampicillin resistance gene, this antibiotic was added to all culture media, allowing the strict selection of the transformed bacteria containing the vector used to overexpress the gene encoding the protein under study. The ampicillin concentration was 0.1 mg/mL, diluted from a 100 mg/mL stock solution.

After transformation, cells were plated on sterile Petri dishes containing solid LB culture medium (*vide* Appendix C.1) with 0.1 mg/mL ampicillin (LB/Agar/Amp) and incubated overnight at 37 ^{o}C to promote colony growth.

3.2 Overexpression in 2xYT, extraction and purification

The following overexpression protocol was established by Daniela Penas and Márcia Guilherme [44]. In order to have a large-scale production and subsequent purification, two steps of pre-cultures were performed prior to the main overexpression growth. The first step consisted of 5 mL of LB medium (*vide* Appendix C.1) containing 0.1 mg/mL ampicillin (pre-inoculum I), that grew at 200 rpm and 37 ^{o}C for about 8 h. The second step consisted in the addition of 1 mL of pre-inoculum I to 100 mL of LB/Amp medium that grew overnight at 200 rpm and 37 ^{o}C (pre-inoculum II). Finally, 10 mL of pre-inoculum II were inoculated in 1 L of 2xYT medium (*vide* Appendix C.2) and the cells were allowed to grow at 180 rpm and 37 ^{o}C. This medium was chosen because it had already been determined that it is the one that gathers the best growth conditions [44]. Microbial growth was monitored measuring the $OD_{600\ nm}$ until it reached 0.5, at which point the culture was induced with 0.2 mM IPTG (*NZYTech*), supplemented with 72 μM $FeSO_4.7H_2O$, and left to grow overnight at 180 rpm and 20 ^{o}C. All these growth procedures were performed aerobically. After growth, cells were harvested by centrifugation for 15 min at 3 900 *g* and 4 ^{o}C, with an average of 7.675 g cells/L of culture medium (wet weight). The overexpression conditions are summarized and schematized in Figure 3.2.

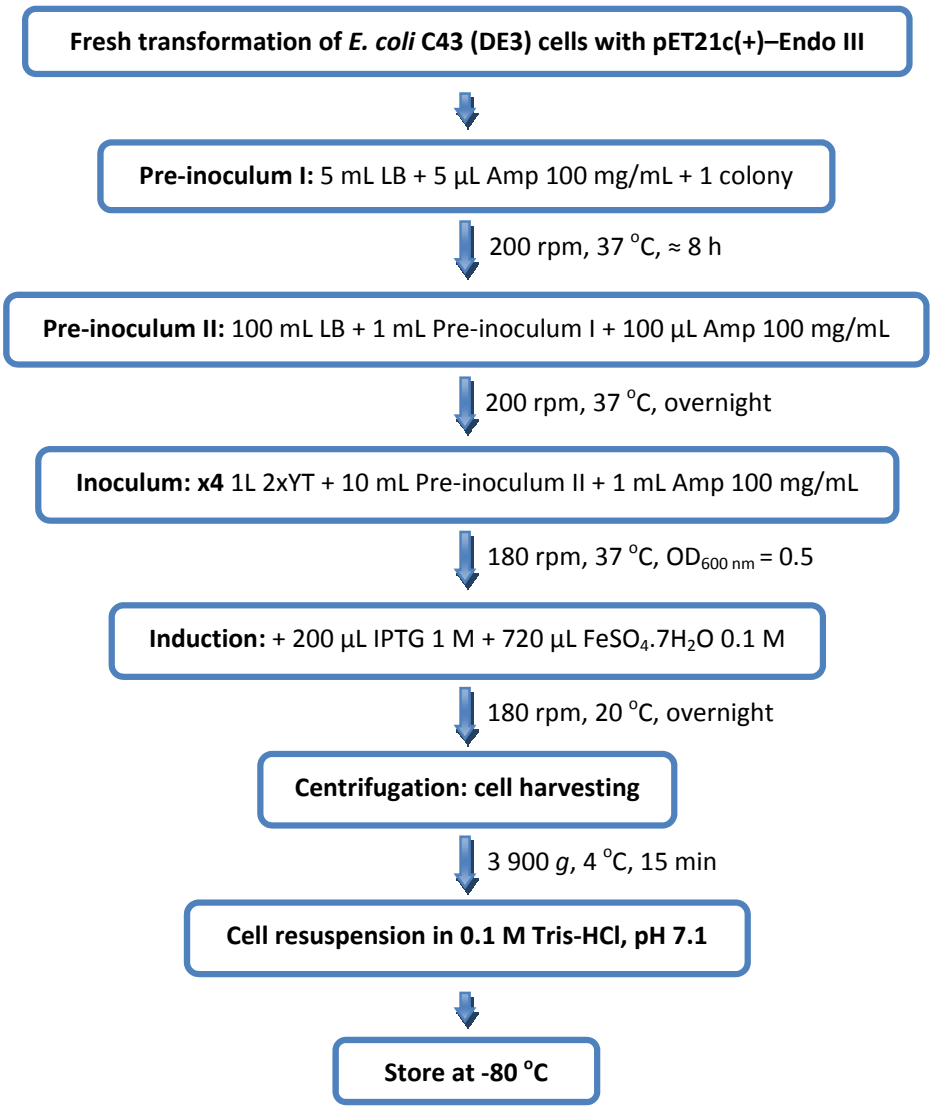

Figure 3.2 | Schematic representation of the homologous overexpression of recombinant Endo III in *E. coli*, in 2xYT medium.

After Endo III overexpression, the protein was isolated from the remaining cellular components before proceeding with its purification. Therefore, the extraction protocol included firstly thawing cells with a water flow and then cell disruption through 3 cycles with an ultrasonic probe. Each cycle consisted of 3 min at 104 W cm^{-2} and 1 min 30 s at rest, always on ice. During cell disruption, DNase (*Roche*) was added to the cell suspension to reduce the viscosity of the cellular extract. After centrifugation for 20 min at 10 500 *g* and 4 °C, the resulting supernatant was ultracentrifuged for 1 h 30 min at 125 000 *g* and 4 °C, to separate membrane and soluble fractions. Protein overexpression and cellular localization were verified by SDS-PAGE (Figure 3.3, *vide* Appendix E.1 for SDS-PAGE preparation).

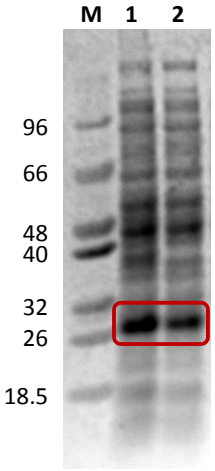

Figure 3.3 | Endo III production time course analyzed by SDS-PAGE (4-12 % gradient pre-cast NuPAGE® gel (*Invitrogen*), 35 min, 200 V). The gel was stained with Coomassie Brilliant Blue. The molecular mass (in kDa) of each protein standard is indicated on the left side of the figure. **M** – LMW Standard (*vide* Appendix E.1, Figure E.1.A); **1** – Supernatant after low-speed centrifugation; **2** – Supernatant after ultracentrifugation. The red box indicates the Endo III protein bands.

Observation of the electrophoretic profile in Figure 3.3 reveals an intense band corresponding to Endo III (red boxed bands), with a determined molecular mass of 27.6 kDa. This value is similar to the one described in the literature, which is 26.3 kDa in the native state [27].

The soluble fraction was then used to purify the protein under study. Based on *E. coli* Endo III theoretical isoelectric point (8.4), determined from its primary sequence with *Protparam* software (http://web.expasy.org/protparam/) [45], it was assumed that the protein had a positive total charge at pH 7.1. As such, an ionic exchange chromatography was used. The soluble extract, overnight dialyzed against 0.1 M Tris-HCl, pH 7.1 and clarified by filtration was applied onto a pre-equilibrated Resource S (6 mL, *GE Healthcare*) column coupled to an ÄKTA system (Prime Plus, *GE Healthcare*) at 6 mL/min (*vide* Appendix D). After column washing with 0.1 M Tris-HCl, pH 7.1 (buffer A), a continuous linear gradient up to 1 M Tris-HCl, pH 7.1 (buffer B) at 6 mL/min was applied to elute adsorbed proteins. 4 mL fractions were collected.

The purity of collected fractions was assessed by UV-Vis spectrophotometry, using the A_{410nm}/A_{280nm} ratio. Due to their aromatic amino acids content, most proteins absorb light at 280 nm, whereas the Fe-S bond of Endo III [4Fe-4S] cluster absorbs at 410 nm [19, 20, 46, 47]. Fractions with higher purity (A_{410nm}/A_{280nm} ratio ≥ 0.3) were combined in a fraction named F.I, whilst the ones with lower purity level (0.2 ≤ ratio < 0.3) were combined in a fraction named F.II.

Besides UV-Vis spectrophotometry, SDS-PAGE was also used to assess the purity of these fractions. The results are presented in Figure 3.4.

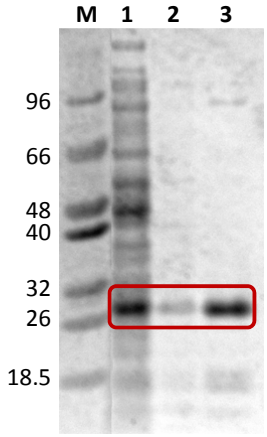

Figure 3.4 | Purity assessment of fractions collected from the Resource S chromatographic column by SDS-PAGE (4-12 % gradient pre-cast NuPAGE® gel (*Invitrogen*), 35 min, 200 V). The gel was stained with Coomassie Brilliant Blue. The molecular mass (in kDa) of each standard is indicated on the left side of the figure. **M –** LMW Standard; **1 –** Flow-through fraction; **2 –** F.II; **3** – F.I. The red box indicates the bands corresponding to Endo III.

Analysis of Figure 3.4 confirms the higher purity of fraction F.I. Since a large amount of protein was detected in the flow-through fraction, the decision was to recover it by performing a second ionic exchange chromatography, using the same column. Fraction F.I was considered pure and was used in the subsequent studies.

Fraction F.I was dialyzed overnight in 0.1 M Tris-HCl, pH 7.1 and centrifuged for 20 min at 10 500 *g* and 4 °C. Finally, a UV-Vis spectrum (250 to 800 nm) of a 1:4 dilution of this fraction was performed (Figure 3.5) to calculate its concentration through the Lambert-Beer's Law.

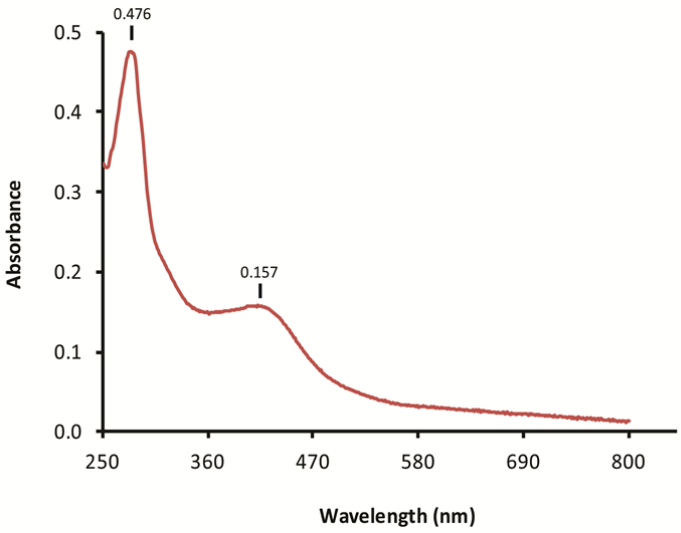

Figure 3.5 | UV-Vis spectrum of pure Endo III overexpressed in 2xYT medium.

As mentioned before, the Fe-S bonds of Endo III cluster absorbs at 410 nm; therefore, this was the wavelength used to quantify F.I. Using the published molar extinction coefficient of Endo III at this wavelength (1.7×10^4 $M^{-1}cm^{-1}$) [20], the protein concentration was determined to be 36.94 µM.

3.3 Overexpression in M9 medium, extraction and purification

The purpose was to optimize the conditions of Endo III overexpression in M9 medium for further enrichment in ^{57}Fe. This iron isotope is widely used in Mössbauer spectroscopy (*vide* Future work, Chapter 11).

Two steps of pre-cultures were performed prior to the main overexpression growth. The first step consisted of 5 mL of LB/Agar medium containing 0.1 mg/mL ampicillin (pre-inoculum I), that grew at 200 rpm and 37 ^{o}C for about 8 h. The second step consisted in the addition of 1 mL of pre-inoculum I to 100 mL of M9 (*vide* Appendix C.3) medium containing 0.1 mg/mL ampicillin, that grew overnight at 200 rpm and 37 ^{o}C (pre-inoculum II). Finally, 10 mL of pre-inoculum II were inoculated in 1 L of M9 medium and the cells were allowed to grow at 180 rpm and 37 ^{o}C. Microbial growth was monitored measuring the $OD_{600\ nm}$ until it reached 0.5, at which point the culture was induced with 0.2 mM IPTG (*NZYTech*), supplemented with 0.2 mM $FeSO_4.7H_2O$, and left to grow overnight at 180 rpm and 20 ^{o}C. All these growth procedures were performed aerobically. After growth, cells were harvested by centrifugation for 15 min at 3 900 *g* and 4 ^{o}C, with an average of 7 g cells/L of culture medium (wet weight). The overexpression conditions are summarized and schematized in Figure 3.6.

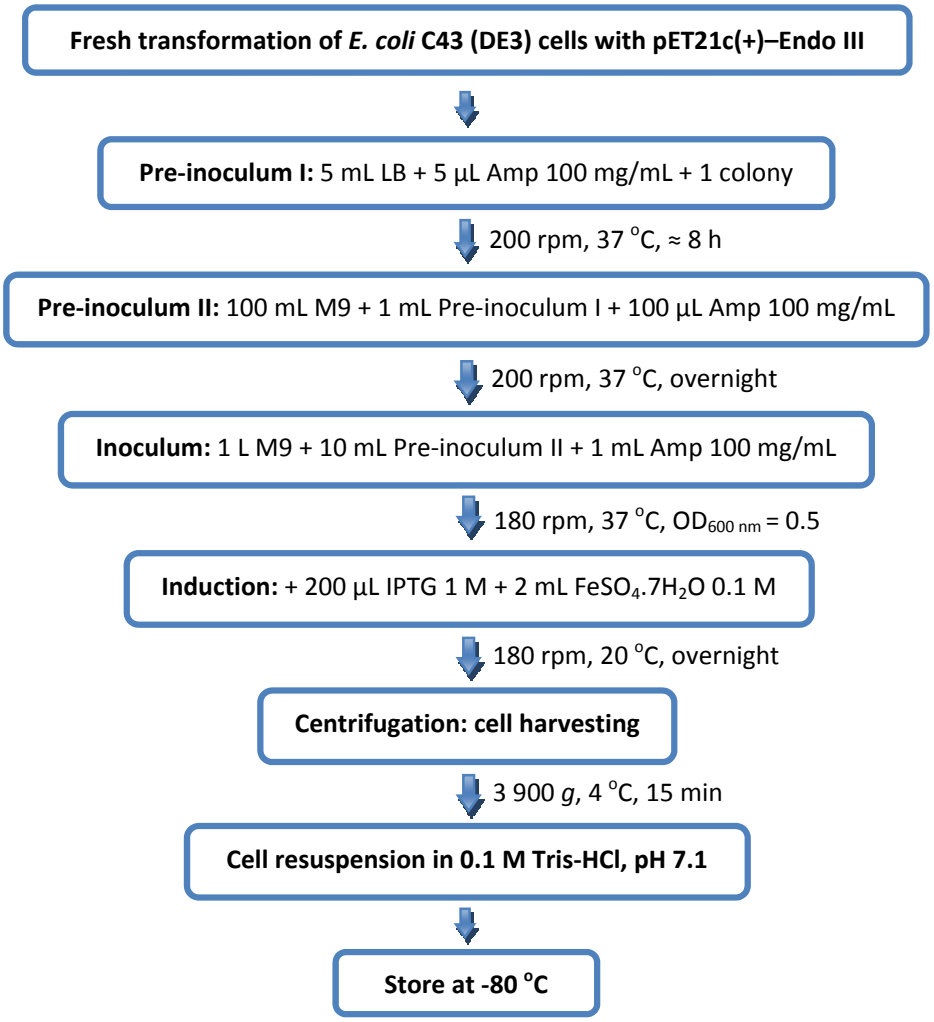

Figure 3.6 | Schematic representation of the homologous overexpression of recombinant Endo III in *E. coli*, in M9 medium.

After Endo III overexpression, the protein was isolated from the remaining cellular components in the same way as described for overexpression in 2xYT medium. After centrifugation for 20 min at 10 500 *g* and 4 °C, the resulting pellet was resuspended in 0.1 M Tris-HCl, pH 7.1 and went through cell disruption and centrifugation as early mentioned. The supernatant obtained in the first centrifugation (SN1) and the one resulting from pellet centrifugation (SN2) were mixed together and ultracentrifuged for 1 h 30 min at 125 000 *g* and 4 °C, to separate membrane and soluble fractions. Protein overexpression and cellular localization were verified by SDS-PAGE (Figure 3.7).

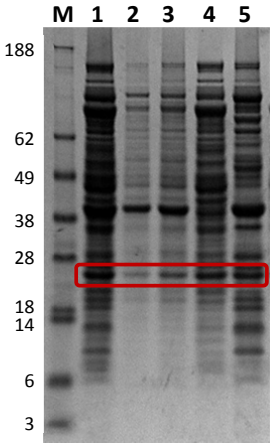

Figure 3.7 | Endo III production time course analyzed by SDS-PAGE (4-12 % gradient pre-cast NuPAGE® gel (*Invitrogen*), 35 min, 200 V). The gel was stained with Coomassie Brilliant Blue. The molecular mass (in kDa) of each protein standard is indicated on the left side of the figure. **M** – SeeBlue® Pre-stained Standard (vide Appendix E.1, Figure E.1.B.); **1** – Supernatant after low-speed centrifugation (SN1); **2** – Pellet after low-speed centrifugation; **3** – Supernatant resulting from low-speed centrifugation of the resuspended pellet (SN2); **4** –Supernatant after ultracentrifugation; **5** – Pellet after ultracentrifugation. The red box indicates the Endo III protein bands.

The red boxed bands observed in Figure 3.6 correspond to Endo III, with a calculated molecular mass of 23.1 kDa. This value is similar to the one described in the literature, which is 23.5 kDa (predicted from the amino acid sequence) [27].

Endo III was then purified in the same way as described for overexpression in 2xYT medium. The elution profile of the purification step is presented in Figure 3.8.

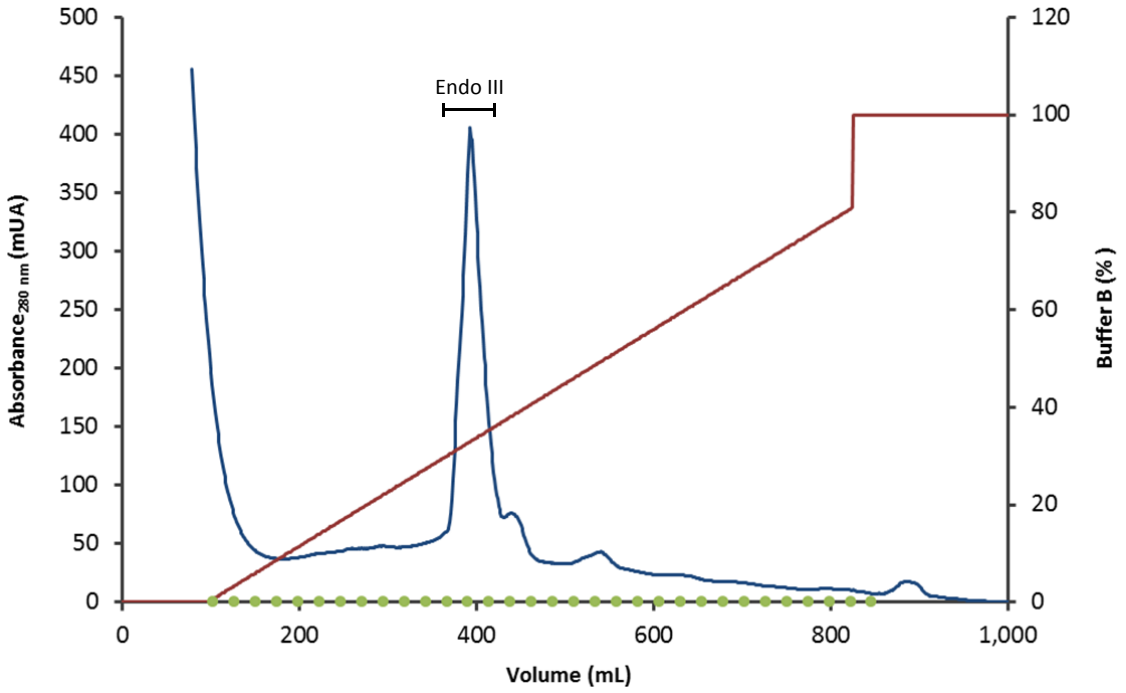

Figure 3.8 | Elution profile of Resource S chromatographic column used in Endo III purification. A continuous linear gradient up to 1 M Tris-HCl, pH 7.1 (buffer B) at 6 mL/min was applied for protein elution. 4 mL fractions were collected. The first band to be eluted was excluded since it corresponds to proteins that did not adsorbed to the chromatographic medium. Blue line, Endo III elution; red line, Buffer B gradient; green dots, fractions.

According to the elution profile, Endo III was eluted between 350 to 425 mM of buffer (i.e., from 28 to 36 % buffer B), corresponding to fractions 12, 13 and 14. The purity of these fractions was assessed by UV-Vis spectrophotometry, using the A_{410nm}/A_{280nm} ratio. Fraction 13 had higher purity (A_{410nm}/A_{280nm} ratio ≥ 0.3) and was named fraction F.I. Fractions 12 and 14 were combined in a fraction named F.II since they had a lower purity level (0.2 ≤ ratio < 0.3).

Besides UV-Vis spectrophotometry, SDS-PAGE was also used to assess the purity of these fractions. The results are presented in Figure 3.9.

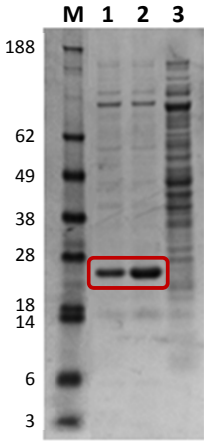

Figure 3.9 | Purity assessment of fractions collected from the Resource S chromatographic column by SDS-PAGE (4-12 % gradient pre-cast NuPAGE® gel (*Invitrogen*), 35 min, 200 V). The gel was stained with Coomassie Brilliant Blue. The molecular mass (in kDa) of each standard is indicated on the left side of the figure. **M –** SeeBlue® Pre-stained Standard; **1 –** F.II; **2** – F.I.; **3 –** Flow-through fraction. The red box indicates the bands corresponding to Endo III.

Analysis of Figure 3.9 confirms the higher purity of fraction F.I. Although this fraction was not dialyzed, a UV-Vis spectrum (250 to 800 nm) of a 1:10 dilution of it was performed (Figure 3.10) to calculate its concentration through the Lambert-Beer's Law. The protein concentration of F.I was determined to be 35.29 µM.

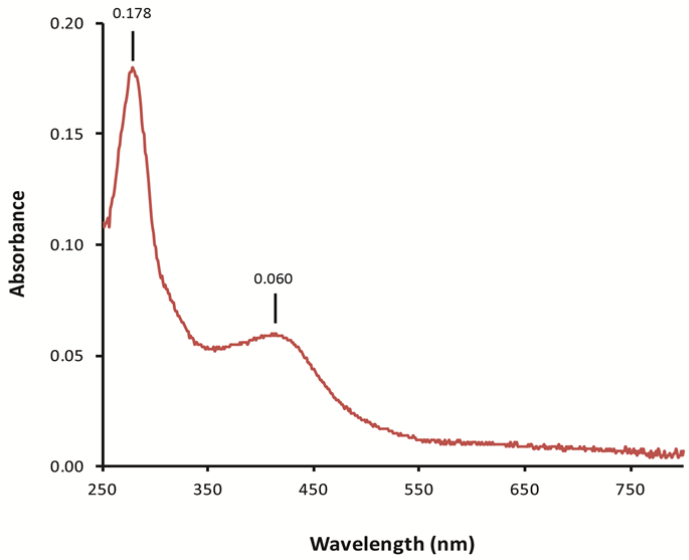

Figure 3.10 | UV-Vis spectrum of pure Endo III overexpressed in M9 medium.

Chapter 4 Protein and iron quantifications

4.1 Protein quantification

Nowadays, there are several methods available for protein quantification. In this work, the method described by Lowry and coworkers was used [48].

The reaction mechanism involves reduction of the Folin reagent and oxidation of aromatic amino acids (mainly tryptophan, also tyrosine). The concentration of the reduced Folin reagent is then measured by absorbance. As a result, the total concentration of protein in the sample can be deduced from the concentration of Trp and Tyr residues that reduce the Folin reagent [48].

Taking into account what was mentioned above, it was necessary to choose which protein standard to use. In general, one should choose a protein with an amino acid composition similar to the protein to be quantified.

In Table 4.1, the molecular mass and content in aromatic amino acids of each protein, obtained with *ProtParam* software, are presented.

Table 4.1 | Molecular mass and aromatic amino acids composition of Endo III, Rubredoxin and BSA.

Protein	Molecular mass (kDa)	Total number of aa	Aromatic aa composition
E. coli Endo III	23.6	211	Tyrosine = 5 Tryptophan = 2 Phenylalanine = 6
D. vulgaris Rubredoxin (Rd)	5.6	52	Tyrosine = 3 Tryptophan = 1 Phenylalanine = 2
Bos taurus (Bovine) Serum Albumin (BSA)	69.3	607	Tyrosine = 21 Tryptophan = 3 Phenylalanine = 30

According to the information contained in Table 4.1, Rubredoxin (laboratory stock) was chosen as the standard because its content in aromatic amino acids is more similar to that of Endo III.

Stock concentration of Rubredoxin was determined by UV-Vis spectroscopy, using a molar extinction coefficient at 490 nm of 6 900 M^{-1} cm^{-1} [49]. Taking the 1:50 dilution into account, its concentration was determined to be 3.23 mM. This value was converted to mg/mL using Rubredoxin molecular mass (5 574.1 Da). The protein was then diluted to 2 mg/mL and its concentration was confirmed by UV-Vis spectroscopy (Figure 4.1).

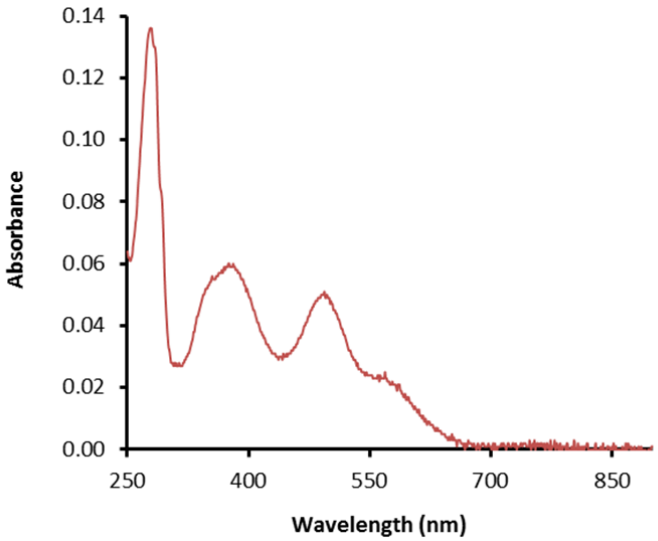

Figure 4.1 | UV-Vis spectrum of Rubredoxin (2 mg/mL).

Lastly, it was necessary to do a further dilution to 0.5 mg/mL, and this was the concentration used in Lowry's protocol (*vide* Appendix F.1.1).

Regarding Endo III samples, two different dilutions were made from an initial Endo III concentration of 28.47 µM that was determined by UV-Vis spectroscopy (1:4 dilution) (Figure 4.2).

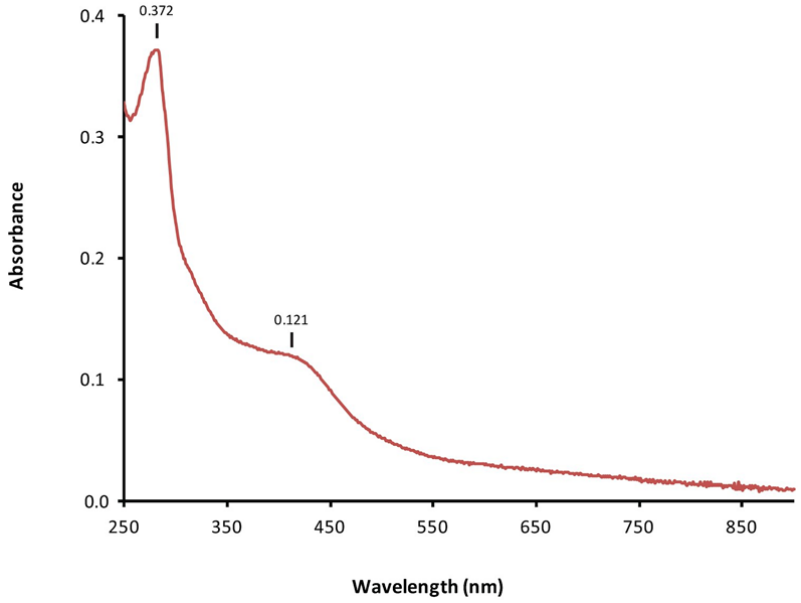

Figure 4.2 | UV-Vis spectrum of pure Endo III.

After preparation of the standards (in duplicate) and the Endo III samples (in triplicate), absorbance measurements at 580 nm were performed (Figure 4.3).

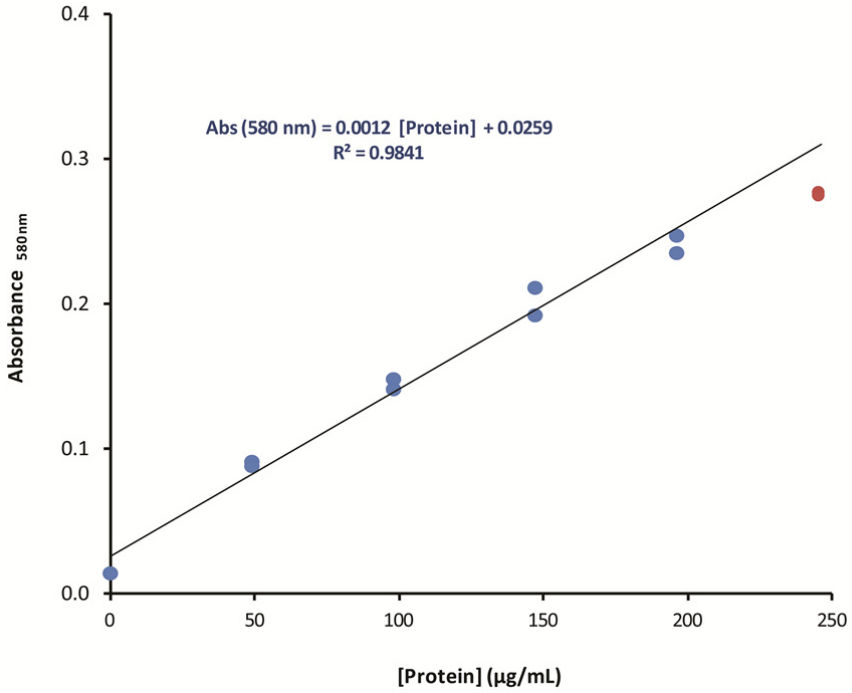

Figure 4.3 | Calibration curve obtained with Rubredoxin standard for the Lowry method. The experimental datapoint in red was not considered for the linear regression.

After measurements, the concentration of Endo III samples was determined using the calibration curve equation obtained (Figure 4.3). Endo III concentration was determined to be 26.35 ± 4.28 µM. Given the associated error, this value is close to the one calculated from the UV-Vis spectrum (28.47 µM, Figure 4.2). Based on the protein concentration, a molar extinction coefficient at 410 nm was determined to be equal to 18 365 ± 2 462 M^{-1} cm^{-1}, which is close to the reported $\varepsilon_{410\ nm}$ of $1.7x10^4$ M^{-1} cm^{-1} for this enzyme [20], given the associated error.

Other common method used to quantify protein is the BCA (Bicinchoninic Acid) method [50], which was also used to determine the concentration of Endo III (*vide* Appendix F.1.2 for method description). This method was performed based on manufacturer's protocol [51]. Since the concentration values obtained were not reproducible, they were not shown nor used.

4.2 Iron content determination

Iron quantification was achieved by performing the Phenanthroline method [52].

In the Phenanthroline method, the amount of iron present in a sample is determined by reacting this element with 1,10-phenanthroline, a bidentate ligand. This reaction will form a stable orange-red complex, which can be then monitored through absorbance measurements at 510 nm. For the phenanthroline to react with iron, this ion must be first reduced to its ferrous state, which is done by reacting the iron with hydroxylamine hydrochloride through the following reaction [53]:

$$2Fe^{3+} + 2NH_2OH + 2OH^- \rightarrow 2Fe^{2+} + N_2 + 4H_2O$$

The complex formation is exemplified in Figure 4.4.

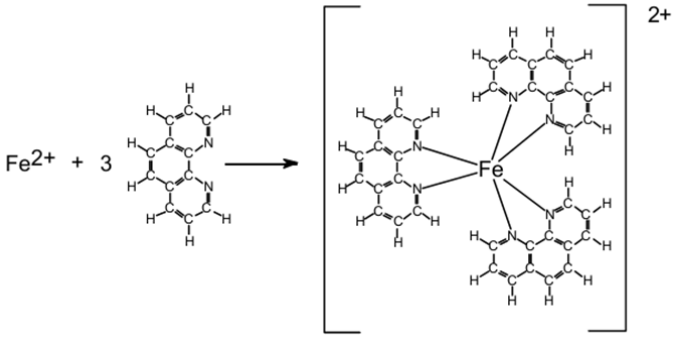

Figure 4.4 | Phenanthroline-iron complex formation [53].

The Phenanthroline method requires extraction of iron from the protein polypeptide chain. Therefore, Endo III samples (30 nmol Fe) were reduced with L(+)-ascorbic acid sodium salt. After 10 min of incubation, the pH was lowered with HCl and protein was precipitated by addition of trichloroacetic acid. The supernatant of centrifuged samples was transferred to a new tube [54].

The calibration curve was obtained with a standard iron solution (0.01 mg/mL) following a protocol adapted from [55] (*vide* Appendix F.2).

After preparing the standards (in duplicate) and the iron samples (in triplicate), absorbance measurements at 510 nm were performed (Figure 4.5).

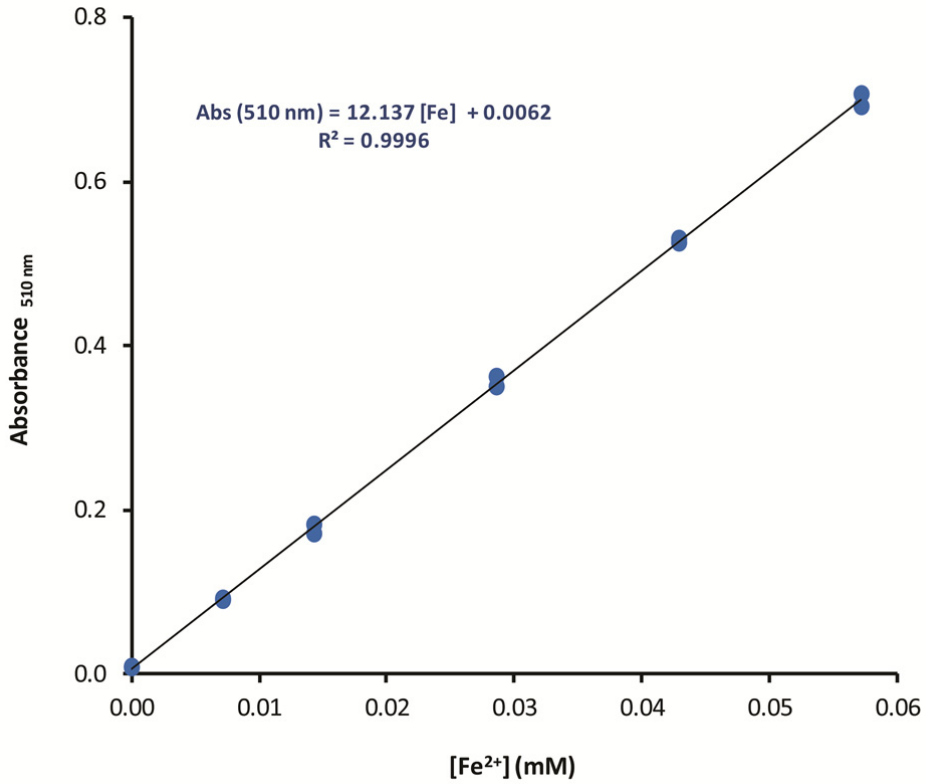

Figure 4.5 | Calibration curve for iron quantification using 1,10 - Phenanthroline method.

The iron content in Endo III samples was determined using the calibration curve equation obtained (Figure 4.5). After determining all sample quantification, the average iron concentration was calculated, coming to a value of 102.153 ± 0.952 µM (Table 4.2).

Table 4.2 | Determination of iron content in Endo III.

Sample	$A_{510\ nm}$ median	[Fe] median (mM)	[Fe] median taking dilutions into account (mM)	[Fe] median taking dilutions into account (µM)	StDev (µM)
Fe_Endo_0.5 mL	0.131	0.010	0.103	102.8	0.1
Fe_Endo_0.6 mL	0.154	0.012	0.101	101.5	0.0
				102.2	**1.0**

As mentioned before, each molecule of Endo III contains a [4Fe-4S] cluster. Thus, assuming that all clusters are intact, there should be 4 iron ions for protein. The Fe/protein ratio determined was 3.88 ± 0.63, which proves, once more, that the protein was purified with a high degree of purity and in a [4Fe-4S] fully-loaded form.

Chapter 5 Effect of UV radiation on plasmid DNA

This chapter aims to present the results obtained with the exposure of plasmid DNA (pDNA) to UV radiation and provide an explanation for those results.

Firstly, it was necessary to isolate pDNA to be used in the irradiation assays.

All trademarks not mentioned, instrumentation and protocols used in this chapter are described in the Appendices section.

5.1 pUC18 isolation

The first step in the pDNA production was the transformation of chemically competent NZY5α cells with pUC18 plasmid, which was performed according to the manufacturer's protocol (*vide* Appendix B.2.2). pUC18 is a plasmid DNA with 2 686 bp (*vide* Appendix G).

Since the plasmid contains an ampicillin resistance gene, this antibiotic was added to all culture media, allowing the strict selection of the transformed bacteria containing the vector. The ampicillin concentration was 100 µg/mL.

After transformation, cells were spreaded on LB/Agar/Amp Petri dishes and incubated overnight at 37 °C.

The microbial growth started with one pre-inoculum, in LB/Amp, that grew for about 8 h at 200 rpm and 37 °C. The culture was left to grow overnight in LB medium at 180 rpm and 37 °C. Finally, pUC18 plasmid was isolated from cells according to *Plasmid Midi Kit* protocol (*Omega*). The production conditions are summarized and schematized in Figure 5.1.

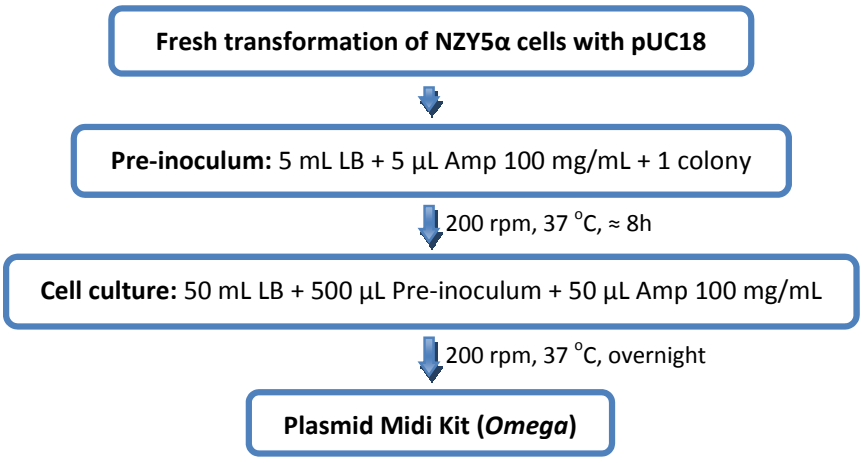

Figure 5.1 | Schematic representation of the production of pUC18 in NZY5α cells.

After pUC18 extraction and purification, its purity was assessed by a 0.8 % agarose gel electrophoresis (Figure 5.2), which was prepared according to the manufacturer's instructions (*vide* Appendix E.2). The results were visualized with SYBRSafe stain (*Invitrogen*) and imaged with Safe Imager ™ (*Invitrogen*) in a Gel Logic 100, Imaging System (*Kodak*).

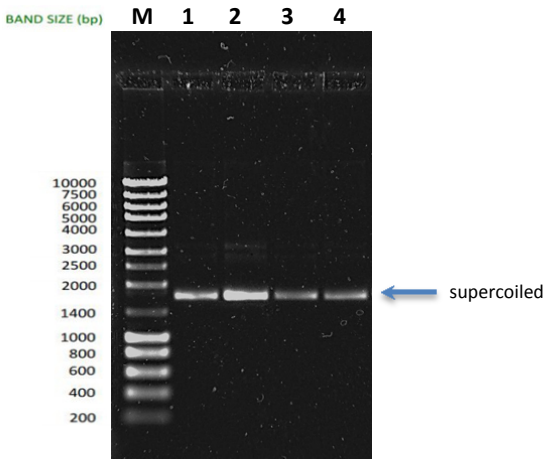

Figure 5.2 | pUC18 plasmid purity assessement by a 0.8 % agarose gel electrophoresis (1 h 15 min, 80 V). The gel was stained with SYBRSafe. The molecular size (bp) of each DNA standard is indicated on the left side of the figure. **M** – NZYDNA Ladder III Standard (*vide* Appendix E.2, Figure E.2); **1 – 4**: pUC18 samples with different concentrations.

From observation of Figure 5.2, it was concluded that the pUC18 samples were pure. This figure shows a typical electrophoretic profile of double strand DNA (dsDNA), with the supercoiled form as the predominant one.

pDNA samples concentration was determined using the molar extinction coefficient of dsDNA at 260 nm, 50 $(\mu g/mL)^{-1}cm^{-1}$ [56]. The concentration of the sample that will be used in the forthcoming irradiation assays (lane 2 in Figure 5.2) was determined to be 80 µg/mL.

To study the effect of UV irradiation on the different forms of pDNA, pUC18 was linearized with the restriction enzyme *Eco*R I.

5.2 pUC18 digestion

pUC18 plasmid was hydrolyzed with *Eco*R I at 37 °C, for 1 h, according to the manufacturer's instructions (*vide* Appendix G).

The hydrolysis efficiency was then assessed by a 0.8 % agarose gel electrophoresis shown in Figure 5.3.

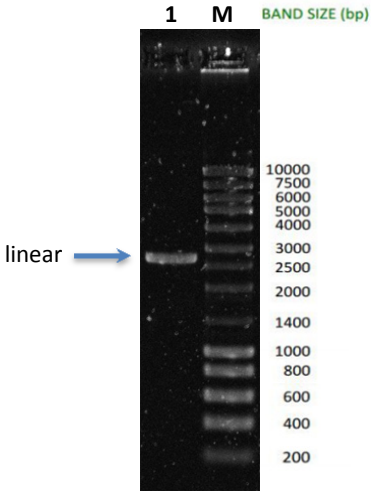

Figure 5.3 | pUC18 hydrolysis efficiency assessed by a 0.8 % agarose gel electrophoresis (1h, 80 V). The gel was stained with SYBRSafe. The molecular size (bp) of each DNA standard is indicated on the right side of the figure. **M** – NZYDNA Ladder III Standard; **1 –** linear pUC18.

From observation of Figure 5.3, it was concluded that the pUC18 hydrolysis was successful. As previously mentioned, this plasmid has 2 686 bp which is in agreement with the molecular size of the band in the gel.

5.3 Irradiation of linear and supercoiled pUC18

The UV exposure assays were performed with the linear and supercoiled forms of pUC18 with a concentration of 1.92 nM, in 0.1 M Tris-HCl, pH 7.1 and at room temperature (*vide* Appendix H.1 for experimental details).

These assays were conducted in a custom-made system that was built as a result of a collaboration with Prof. Paulo Ribeiro's research group from Physics Department at FCT-UNL [57]. The system, consisting of a lamp and a lifting sampler, is housed in a 480 mm x 380 mm x 1800 mm cabinet (Figure 5.4). This cabinet was used as the irradiation chamber and is equipped with a cylindrical Philips TUV PL-S 5W/2P 1CT lamp that has a predominant incidence at the wavelength of 254 nm, low pressure mercury vapor, 34 V of input voltage and 5.5 W of power, of which 1.1 W are UVC [57].

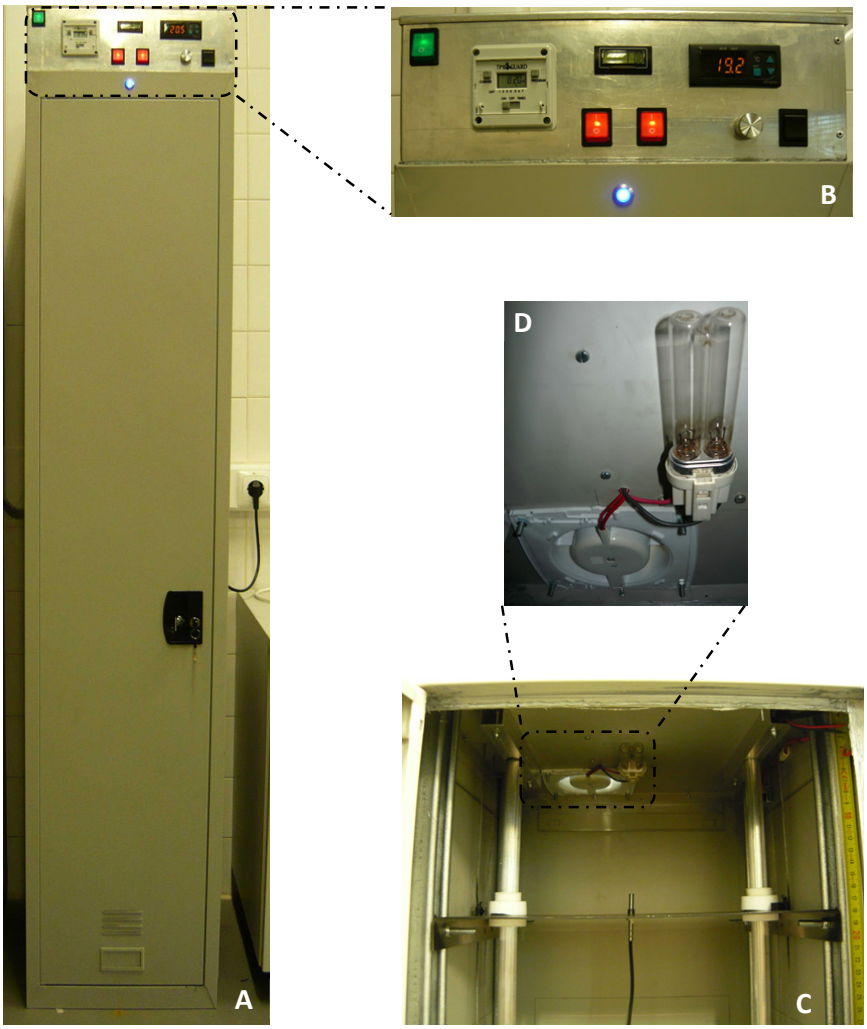

Figure 5.4 | A – Cabinet used in the UV irradiation experiments; **B –** Control unit and UV light on/off indicator (blue light means its on); **C –** Cabinet's interior, with the lifting sampler, the temperature sensor in the middle of it and a graduated scale (on the right); **D –** Air exhaust and cylindrical Philips TUV PL-S 5W/2P 1CT lamp.

Samples were exposed to UV radiation in transparent UV light cuvettes (UV micro-cuvette, *Brand*), at 10 cm distance from this source, while kept on ice. The irradiance ($\mu W/cm^2$) was monitored by a photo-radiometer HD2102.2 (*Delta Ohm*) with a probe LP471UVC (*Delta Ohm*) (Figure 5.5) and converted into dose (J = W.s) by multiplying it by the exposure area (cm^2) and the total time of exposure (s).

Figure 5.5 | Photo-radiometer HD2102.2 (*Delta Ohm*) with a probe LP471UVC (*Delta Ohm*).

Table 5.1 summarizes all exposure times and corresponding doses that were used in the forthcoming assays, knowing that the irradiance measured by the photo-radiometer was 182.5 $\mu W/cm^2$ and the exposure area, 4 mm^2.

Table 5.1 | Radiation doses used in irradiation assays.

Time of exposure to radiation (min)	Dose (kJ)
5	2.20
10	4.39
20	8.79
30	13.18
45	19.77
60	26.36
80	35.15
100	43.94
120	52.73
360	158.18

Linear pUC18 samples (1.92 nM) were exposed to UV radiation for 5, 10, 30, 60, 120 and 360 min (corresponding doses in Table 5.1). One of the samples was not irradiated to serve as control, corresponding to time 0 (zero). The effect of UV radiation exposure on the linearized plasmid DNA was analyzed by a 0.8 % agarose gel electrophoresis, as shown in Figure 5.6.

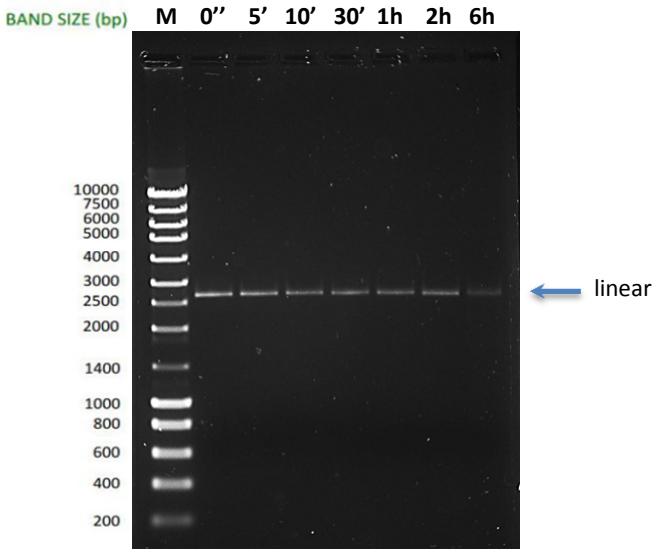

Figure 5.6 | Effects of UV radiation on linear pUC18 (1.92 nM), assessed by 0.8 % agarose gel electrophoresis (1 h 20 min, 80 V). The exposure time is indicated on top of the lanes. The gel was stained with SYBRSafe. The molecular size (bp) of each DNA standard is indicated on the left side of the figure. **M** – NZYDNA Ladder III Standard.

Observing Figure 5.6, one can see a decrease in the band intensity with increasing time of radiation exposure. The most likely hypothesis is that over irradiation, some of pDNA molecules suffer nicks and double strand breaks, leading to the molecule's fragmentation. The resulting lower molecular size fragments have a higher electrophoretic mobility and is highly likely that they end up exiting the gel, given the non-existence of lower molecular size bands in it.

To visualize linear pUC18 degradation with increasing time of exposure to radiation, the bands in Figure 5.6 were quantified using the image processing program ImageJ (http://imagej.nih.gov/ij/), following the software instructions [58, 59]. The area obtained for the first band (corresponding to 0'') was defined as 1, i.e., 100 %, and the fraction corresponding to the others was determined (Figure 5.7).

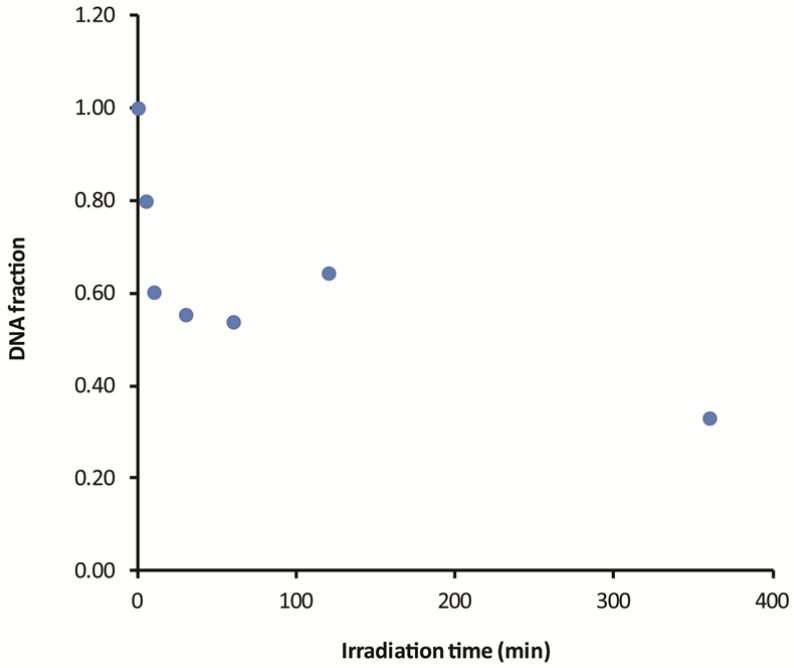

Figure 5.7 | Linear pUC18 degradation with increasing time of UV radiation exposure. The profile was obtained through quantification of the electrophoretic bands of the gel shown in Figure 5.6.

From Figure 5.7 observation, it became clear that after 6 h of irradiation more than 60 % of the initial amount of linear pDNA was damaged.

To infer about the effect of irradiation on supercoiled plasmid DNA (1.92 nM), the previous experiment was repeated with as-isolated pUC18. The effects of exposure to UV radiation were assessed in the same way and are presented in Figure 5.8.

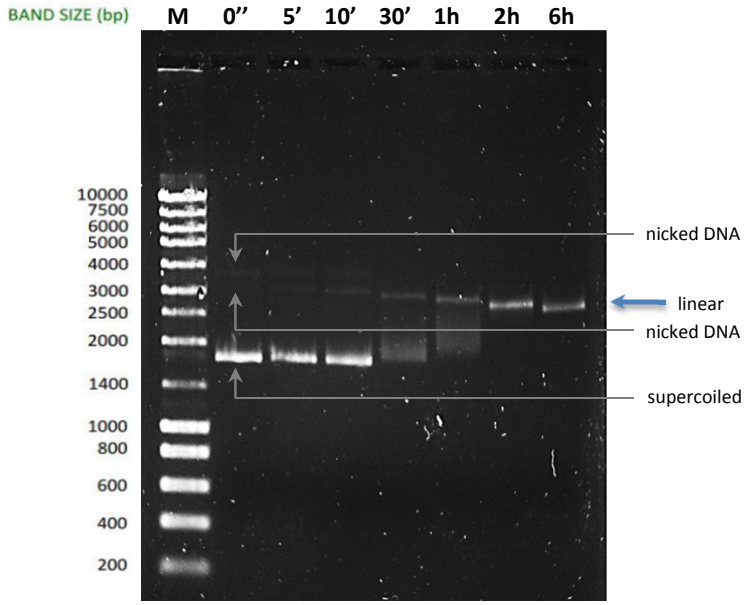

Figure 5.8 | Effects of UV radiation on supercoiled pUC18 (1.92 nM), assessed by 0.8 % agarose gel electrophoresis (1 h 20 min, 80 V). The exposure time is indicated on top of the lanes. The gel was stained with SYBRSafe. The molecular size (bp) of each DNA standard is indicated on the left side of the figure. **M** – NZYDNA Ladder III Standard.

Contrarily to what was observed with the linear pDNA, in Figure 5.8 one can observe significant differences in the electrophoretic mobility of DNA bands. In the experimental conditions tested, after 2 h of exposure to UV radiation (corresponding to a dose of 52.73 kJ) most DNA exhibit mobility corresponding to the linear form of pUC18, indicating that UV radiation leads to double strand breaks in the DNA molecule. Moreover, one can further conclude that once a double break occurs, converting the supercoiled form into the linear one, the effect of UV radiation is less observable, which is in agreement with what was previously stated. Nevertheless, it is worth noting that, as in linear pDNA experiment, the intensity of the bands decreases after 2 h of UV irradiation, indicating that some DNA molecules are hydrolised to small DNA fragments with higher electrophoretic mobility.

To further explore what was observed in Figure 5.8, a series of samples was prepared to increase the number of experimental points in the irradiation time course (corresponding doses in Table 5.1, *vide* Appendix H.1 for experimental details). The effects of exposure to radiation were assessed in the same way and are presented in Figure 5.9.

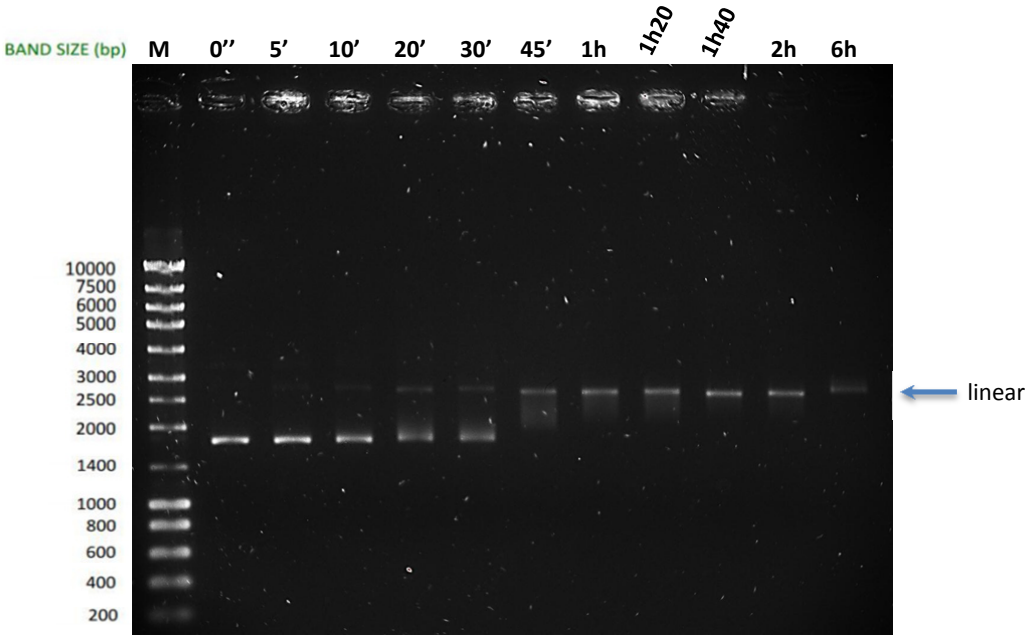

Figure 5.9 | Effects of UV radiation on supercoiled pUC18, assessed by 0.8 % agarose gel electrophoresis (1 h 20 min, 80 V). The exposure time is indicated on top of the lanes. The gel was stained with SYBRSafe. The molecular size (bp) of each DNA standard is indicated on the left side of the figure. **M** – NZYDNA Ladder III Standard.

Observing Figures 5.9 and 5.10, it is possible to note that with increasing time of UV radiation exposure the supercoiled form of pDNA is converted to the linear form, indicating that the supercoiled form suffers double strand break. Total conversion is observed between 1 h 20 min and 1 h 40 min of UV radiation exposure, corresponding to radiation doses of 35.15 and 43.94 kJ, respectively. However, after 1 h 40 min of UV irradition exposure the intensity of linear DNA bands start to decrease, which indicates that some DNA molecules are hydrolised to small DNA fragments, as stated for Figure 5.8.

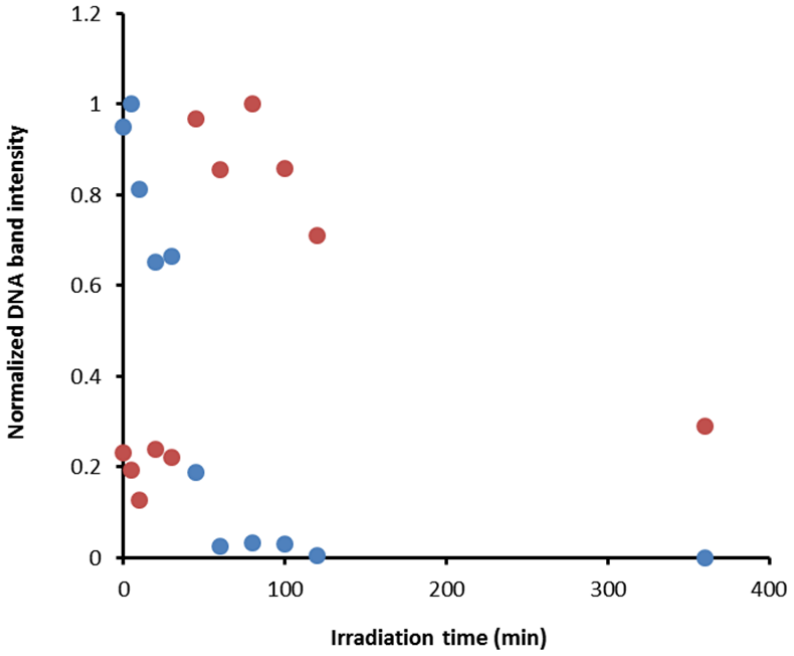

Figure 5.10 | Conversion of DNA supercoiled form (blue dots) to linear form (red dots) with increasing time of UV radiation exposure. The profiles were obtained by quantification of the electrophoretic bands of the gel shown in Figure 5.9. The quantification is presented in terms of band intensity. The decrease in intensity of the bands corresponding to the linear form with increasing UV radiation exposure time indicates that some DNA molecules are being hydrolised to small DNA fragments. Due to their higher electrophoretic mobility, these fragments end up exiting the gel and are not observed.

Chapter 6 Endonuclease III exposure to UV radiation and its effects

This chapter's goal is to present and analyze the results obtained with the exposure of Endo III to UV radiation.

All trademarks not mentioned, instrumentation and protocols used in this chapter are described in the Appendices section.

The assay of Endo III exposure to UV radiation (*vide* Appendix H.2 for experimental details) was conducted with the same equipment and in the same conditions (buffer, irradiation time, doses, distance from source, temperature, etc.) as the pUC18 irradiation assays. In the same way, one of the samples was not irradiated to serve as control (designated time 0). Effect of UV radiation on the protein was assessed by 4-12 % gradient pre-cast "NuPAGE® Novex® Bis-Tris Mini Gel" electrophoresis (Figure 6.1).

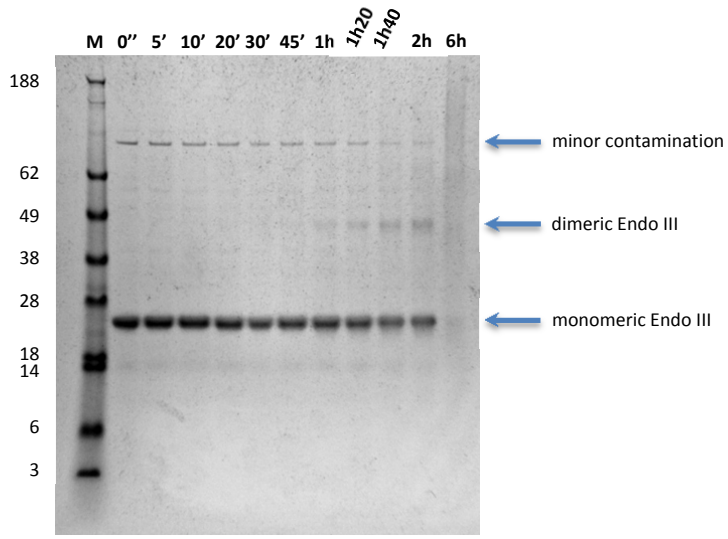

Figure 6.1 | Effects of UV radiation on Endo III (9.24 µM), assessed by SDS-PAGE (4-12 % gradient pre-cast NuPAGE® gel (*Invitrogen*), 35 min, 200 V). The exposure time is indicated on top of the lanes. The gel was stained with Coomassie Brilliant Blue R-250. The molecular mass (in kDa) of each protein standard is indicated on the left side of the figure. **M** – SeeBlue® Pre-stained Standard.

Observing Figure 6.1, it is found that above 45 min of radiation exposure (corresponding to a dose of 19.77 kJ) a band with approximately twice the molecular mass of the lower band, the latter corresponding to Endo III, starts to appear. Simultaneously to the appearance of this tenuous band, a decrease in the intensity of the lower band occurs. This behavior can be explained as the result of the formation of a covalent bond among Endo III protein monomers, probably between two tyrosine residues, a phenomenon commonly described as an effect of UV radiation on protein [60, 61]. This ligation derives from tyrosyl radicals, which are formed when the polypeptide chain tyrosines residues are exposed to UV radiation.

The UV-Vis spectrum of Endo III irradiated samples (Figure 6.2) allows the detection of modifications on the [4Fe-4S] center because this cluster has a maximum absorption at 410 nm. Again, significant modification of the UV-Vis spectrum of the protein was observed after 45 min of irradiation, when the intensity of the absorption peak at 410 nm begins to decrease, which probably means that the Fe-S bonds of the [4Fe-4S] are being destroyed by the UV radiation or that radiation is converting the center into a different redox state [33, 34, 36, 42].

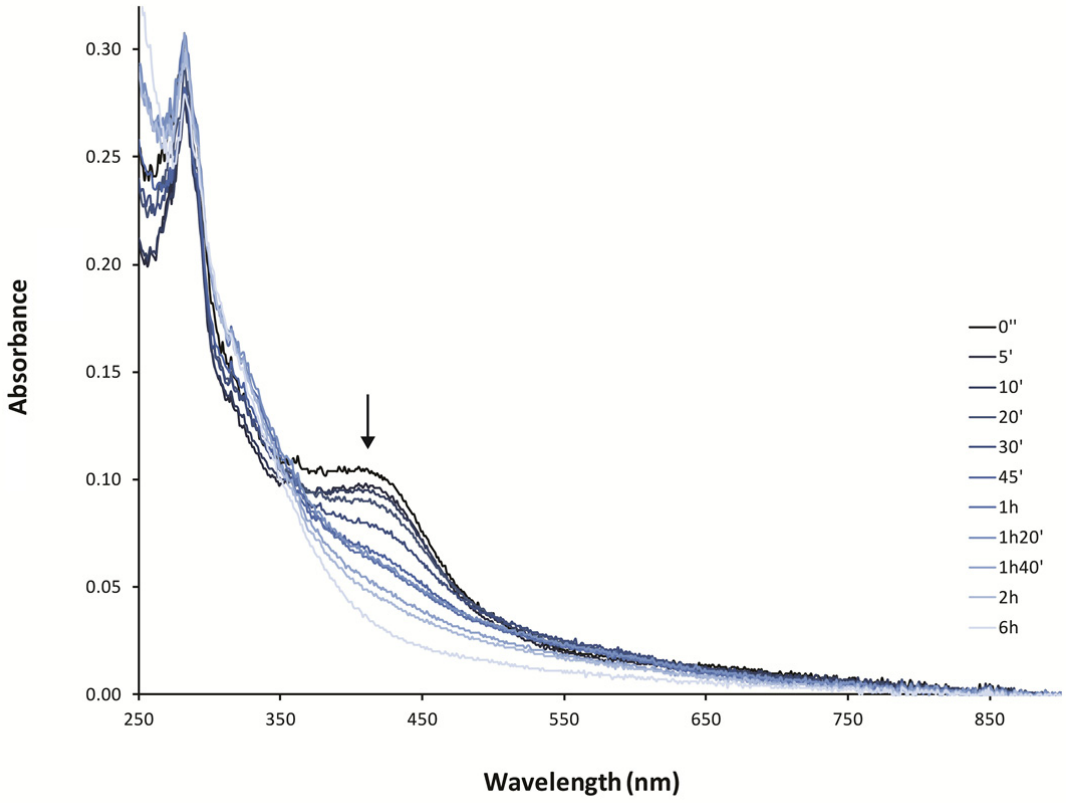

Figure 6.2 | UV-Vis spectrum of irradiated Endo III samples. Irradiation times are indicated on the right side of the graph (from less to more exposed samples). The arrow indicates the absorption peak at 410 nm.

Chapter 7 Electrophoretic mobility shift assays with Endonuclease III-DNA complex

To study the effect of UV radiation on the binding of Endo III to DNA, electrophoretic mobility shift assays (EMSAs) were performed.

The electrophoretic mobility shift assay is a fast and sensitive *in vitro* technique used to detect protein-nucleic acid interactions, i.e., protein-nucleic acid complexes. For this, solutions of protein and nucleic acid are combined and the resulting mixtures are subjected to electrophoresis under native conditions through polyacrylamide or agarose gel. In general, the electrophoretic mobility of a protein-nucleic acid complex is less than that of the free nucleic acid, which means that the rate of DNA migration is shifted or retarded when bound to protein. EMSA can be used quantitatively to measure thermodynamic and kinetic parameters [62, 63].

All trademarks not mentioned, instrumentation and protocols used in this chapter are described in the Appendices section.

The DNA-binding ability of Endo III to pUC18 was tested by EMSA after 2 h of incubation in 0.1 M Tris-HCl, pH 7.1, at room temperature. First, EMSAs were carried out on non-irradiated native protein, at different protein/DNA molar ratios (Figure 7.1). Free pDNA and Endo III samples were also assessed to serve as control.

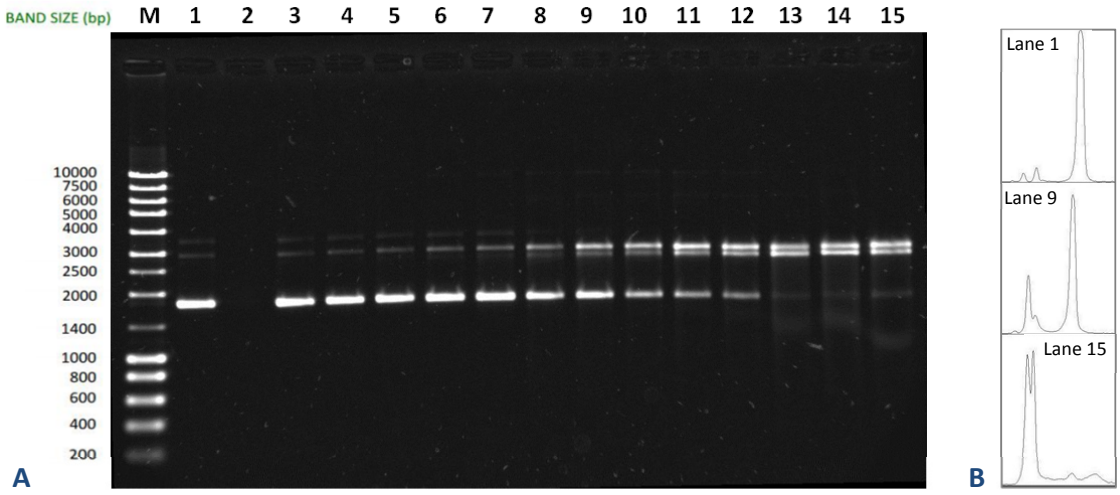

Figure 7.1 | A – Binding of Endo III to supercoiled pUC18 in 0.1 M Tris-HCl, pH 7.1 tested by EMSA (1 % agarose gel, 1 h 45 min, 80 V). The gel was stained with SYBRSafe. The molecular size (bp) of each DNA standard is indicated on the left side of the figure. **B -** Densitometric quantification of free control pDNA (Lane 1) and complex band (Lanes 9 and 15), using ImageJ. **M** – NZYDNA Ladder III Standard; **1** – pUC18 (10 nM) ; **2** – Endo III (10 μM); **3 to 15** – protein/DNA molar ratios of 4, 8, 17, 25, 33, 67, 100, 134, 168, 251, 500, 750, 1000, respectively.

The gel represented on Figure 7.1 shows that Endo III binding to DNA promotes a retardation of the free supercoiled DNA band, which is indicated by a decrease in the band's intensity. At a protein/DNA molar ratio of 500, most of the free DNA band that moves faster in the gel is shifted, showing the formation of Endo III-DNA complex(es) with defined mobility.

To determine DNA-binding ability of Endo III the electrophoretic images (triplicates) were processed (free pDNA and protein-DNA complex bands) using ImageJ. For densitometric quantification, regions above the free DNA were considered as complex. The relative Endo III-pDNA complex formation was plotted (Figure 7.2) as a function of protein concentration and fitted to the Hill equation, $f = f_{max}[Endo\ III]^n / (K_d + [Endo\ III]^n)$, in which f is the fractional saturation, f_{max} corresponds to 100 % complex formation, [Endo III] is the concentration of the binding protein, n is the Hill coefficient and K_d represents the macroscopic apparent dissociation constant and is a measure of the affinity of the protein to pDNA [64].

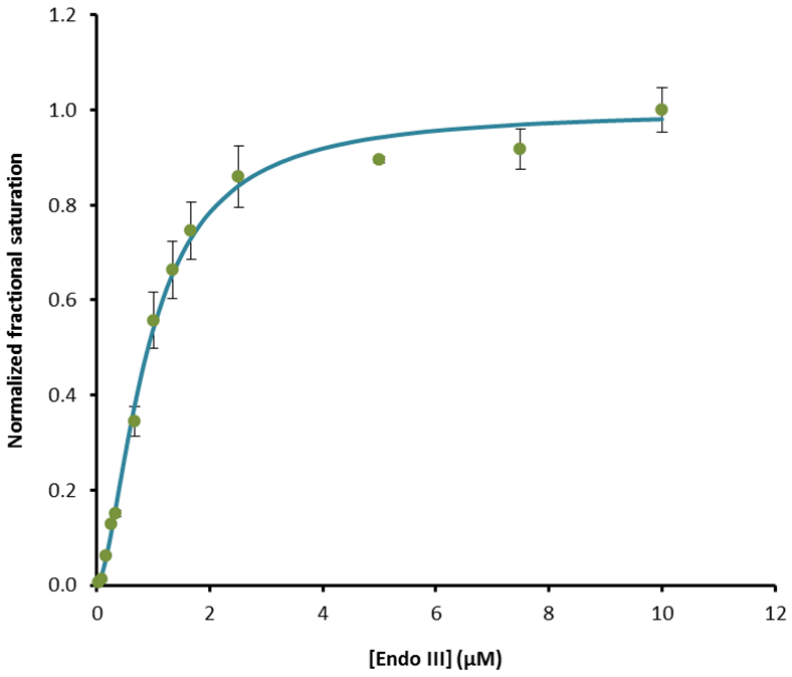

Figure 7.2 | Hill plot of Endo III binding to supercoiled DNA from EMSA, using protein concentrations between 0 µM and 10 µM, and 10 nM of pUC18. Blue line, Hill plot; green dots, experimental data.

Using Excel's Solver tool, the normalized experimental data was fitted to a Hill's equation with a K_d of 0.85 ± 0.13 µM and a n value of 1.63 ± 0.22 for the Endo III-supercoiled pDNA complex.

The same procedure was applied for determination of Endo III binding ability to linear pDNA (Figure 7.3).

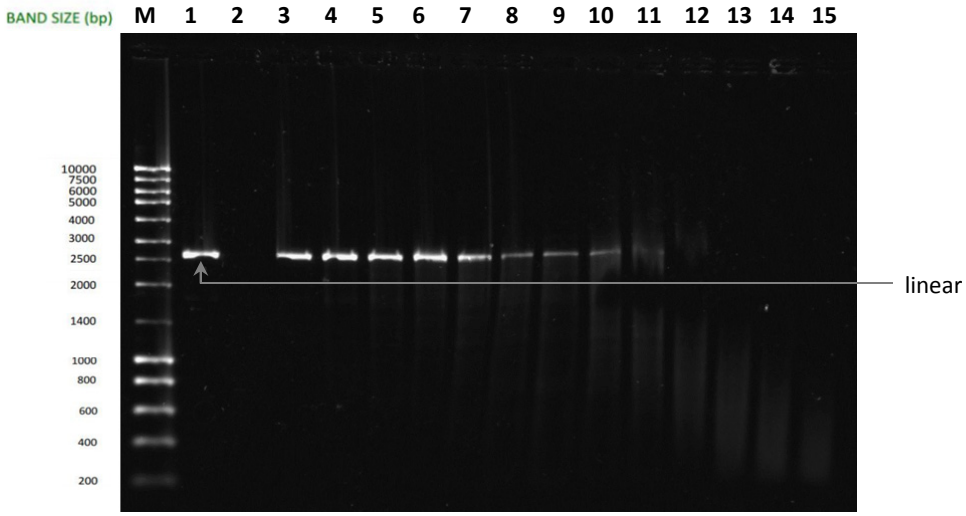

Figure 7.3 | Binding of Endo III to linear pUC18 in 0.1 M Tris-HCl, pH 7.1 tested by EMSA (1 % agarose gel, 1 h 45 min, 80 V). The gel was stained with SYBRSafe. The molecular size (bp) of each DNA standard is indicated on the left side of the figure. **M** – NZYDNA Ladder III Standard; **1** – pUC18 (10 nM); **2** – Endo III (10 μM); **3 to 15** – protein/DNA molar ratios of of 4, 8, 17, 25, 33, 67, 100, 134, 168, 251, 500, 750, 1000, respectively.

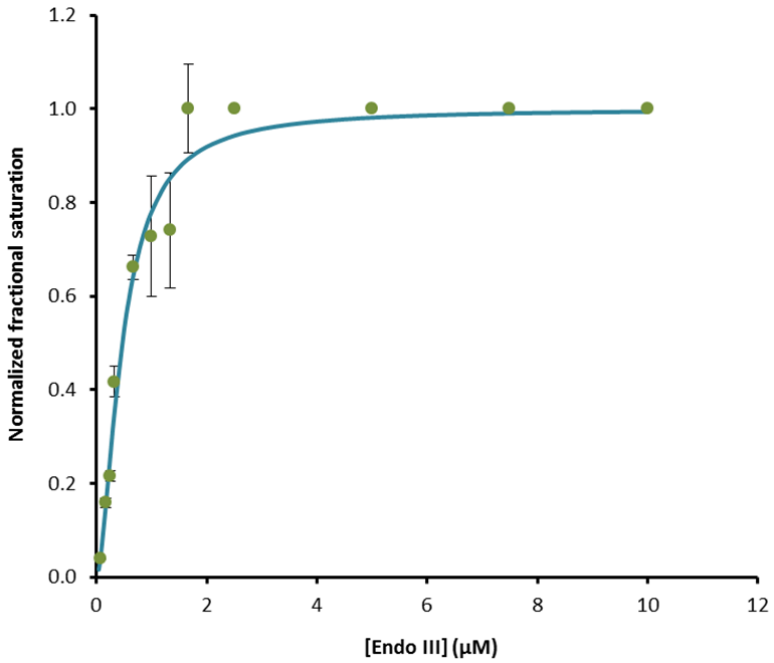

Figure 7.4 | Hill plot of Endo III binding to linear DNA from EMSA, using protein concentrations between 0 μM and 10 μM, and 10 nM of pUC18. Blue line, Hill plot; green dots, experimental data.

Normalized experimental data was fitted to a Hill's equation with a K_d of 0.28 ± 0.09 μM and a *n* value of 1.68 ± 0.30 for the Endo III-linear pDNA complex.

The EMSAs shown in Figures 7.1 and 7.3 demonstrate that recombinant Endo III is able to bind both linear and supercoiled pDNA. As previously stated, K_d value is a measure of the affinity of the protein to pDNA and since Endo III-linear pDNA complex has a lower K_d value, it was concluded that Endo III has a higher affinity to linear pDNA than to its supercoiled form, meaning that Endo III-linear pDNA complex is more stable than Endo III-supercoiled pDNA complex. The $n > 1$ values indicate positive cooperativity on Endo III binding to both supercoiled and linear DNA.

K_d values in the low micromolar range have been reported for *Desulfovibrio vulgaris* bacterioferritin (K_d of 1.5 ± 0.3 μM), HU histone-like proteins (K_d of 0.2–2.5 μM) and IHF (Integration Host Factor) from *E. coli* (K_d of 20–30 μM) [65].

A DNA binding assay in 50 mM Tris-HCl, pH 7.1 was also performed to determine the effect of the ionic strength (Figure 7.5). The same conditions of the previous assay were used, except for the binding buffer.

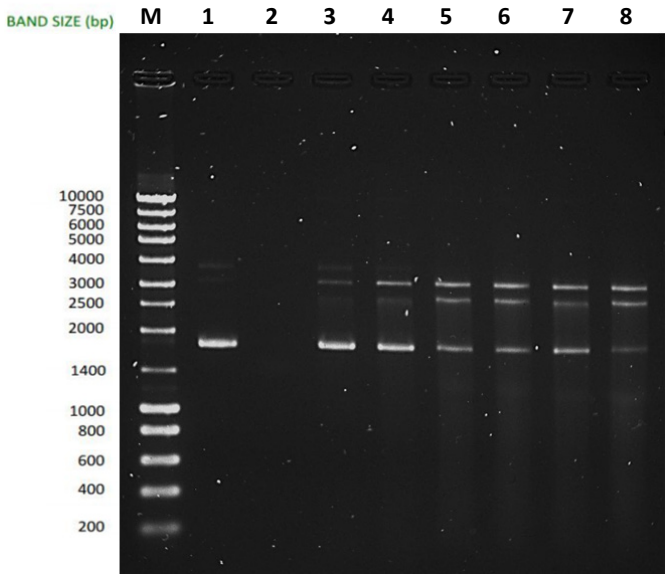

Figure 7.5 | Binding of Endo III to supercoiled pUC18 in 50 mM Tris-HCl, pH 7.1 tested by EMSA (1 % agarose gel, 1 h 45 min, 80 V). The gel was stained with SYBRSafe. The molecular size (bp) of each DNA standard is indicated on the left side of the figure. **M** – NZYDNA Ladder III Standard; **1** – pUC18 (10 nM); **2** – Endo III (4 μM); **3 to 8** – protein/DNA ratios of 25; 50; 100; 150; 200; 400, respectively.

As for the assays in 0.1 M Tris-HCl, pH 7.1 buffer, also here a shift in the migration profile is observed with increasing protein/pDNA ratio. During dialysis (from 100 mM to 50 mM Tris-HCl, pH 7.1), a protein precipitate was observed, indicating that it is not stable at this lower ionic strength. Therefore, Endo III stability during and throughout the assays could not be guaranteed and, as such, the use of this ionic strength was ruled out.

The following assays were performed with Endo III irradiated for different times and then incubated with supercoiled DNA for 2 h in 0.1 M Tris-HCl, pH 7.1, at room temperature. The same Endo III/pDNA ratios and same pUC18 concentration were used.

Endo III samples were irradiated in pairs for two different periods of time (*vide* Appendix H.3 for experimental details). UV exposure assays were conducted with the same equipment and in the same conditions (doses, distance from source, etc.) as the pUC18 and Endo III irradiation assays presented before. After exposure and incubation with pDNA, the effects on protein-DNA complex formation were assessed by a 1 % agarose gel electrophoresis. The results are shown in Figure 7.6. Free pDNA and Endo III samples were also assessed to serve as control.

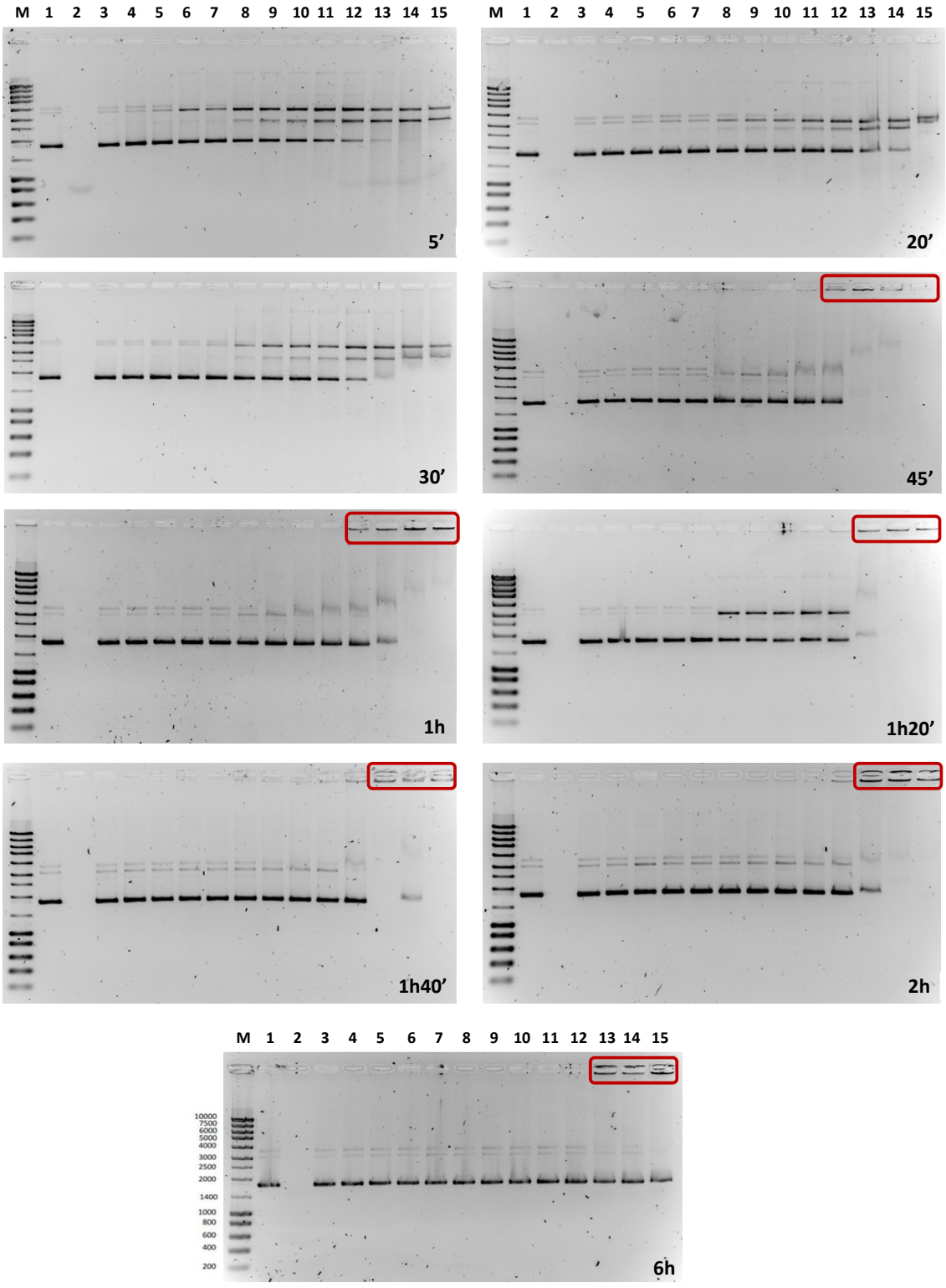

Figure 7.6 | EMSAs with different periods of exposure to radiation. The binding buffer was 0.1 M Tris-HCl, pH 7.1. The electrophoretic mobilities were assessed by 1 % agarose gel electrophoresis (1 h 45 min, 80 V). The gels were stained with SYBRSafe. **M** – NZYDNA Ladder III Standard; **1** – pUC18 (10 nM); **2** – Endo III (10 μM); **3 to 15** – protein/DNA ratios of 4, 8, 17, 25, 33, 67, 100, 134, 168, 251, 500, 750, 1000, respectively. Red-boxed wells contain aggregates that are unable to enter the gel matrix.

From observation of Figure 7.6, it was concluded that up to 30 min of UV irradiation (corresponding to a dose of 13.18 kJ), the behavior is similar to that observed in the assay without irradiation (Figure 7.1). This means that Endo III is not damaged with 30 min of exposure to UV radiation and, therefore, is able to bind to the plasmid.

After 45 min of exposure to radiation (corresponding to a dose of 19.77 kJ) the behavior changes, with the appearance of smeared bands corresponding to complexes with reduced mobility. Additionally, the retardation of the free supercoiled DNA band, indicated by a decrease in the band's intensity, is no longer observed. This fact, together with the smeared complex bands, could indicate that although some Endo III molecules bind to DNA, the complexes formed are somehow unstable and dissociate during electrophoresis. The reduced affinity of Endo III for DNA is possibly due to partial loss of the structure responsible for DNA binding, the FCL motif, owing to a higher exposure time to UV radiation. This is consistent with what was concluded in Chapter 6 (Figure 6.2), that the Fe-S bonds of the [4Fe-4S] clusters are destroyed by the UV radiation or that radiation converts these centers into a different redox state. These results are in agreement with Endo III studies that suggest the need for a fully coordinated $[4Fe\text{-}4S]^{2+}$ cluster for the *in vivo* stability of the enzyme [29]. Moreover, at higher protein/DNA molar ratios (from 251:1), one can observe aggregates that are unable to enter the gel matrix (red boxes). These aggregates are retained in the well because of their large size, suggesting that some Endo III molecules suffer some type of conformational change, probably unfolding, due to UV radiation exposure.

After 6 h of irradiation (corresponding to a dose of 158.18 kJ) the behavior completely changes since no shift occurs, not even at higher protein/DNA molar ratios. The electrophoretic profile in each one of the lanes is the same as the one of the free plasmid (lane 1), which means that no complexes are formed. That allows inferring that Endo III molecules were irreversibly damaged after 6 h of UV radiation exposure.

Chapter 8 Electrochemical characterization of recombinant Endonuclease III

In this chapter, the results on the electrochemical characterization of recombinant Endo III will be analyzed.

All trademarks not mentioned, instrumentation and protocols used in this chapter are described in the Appendices section.

The first step in the electrochemical characterization of Endo III was to verify its 3D-structure and determine its superficial electrostatic charge, in order to define the initial experimental conditions to be used in this study, namely the type of electrode material and the need of promoters/electrode modifiers. These conditions are important to ensure charge transfer between the enzyme and the electrode, and to avoid repulsion. Through the results obtained with the software Accelrys DS Visualizer (v3.5.0.12158) (Figure 8.1), it was concluded that the enzyme has a predominantly positive area (in blue) and a predominantly negative one (in red), with the [4Fe-4S] cluster (represented in Figure 8.1 – A) located, presumably, at the interface between them.

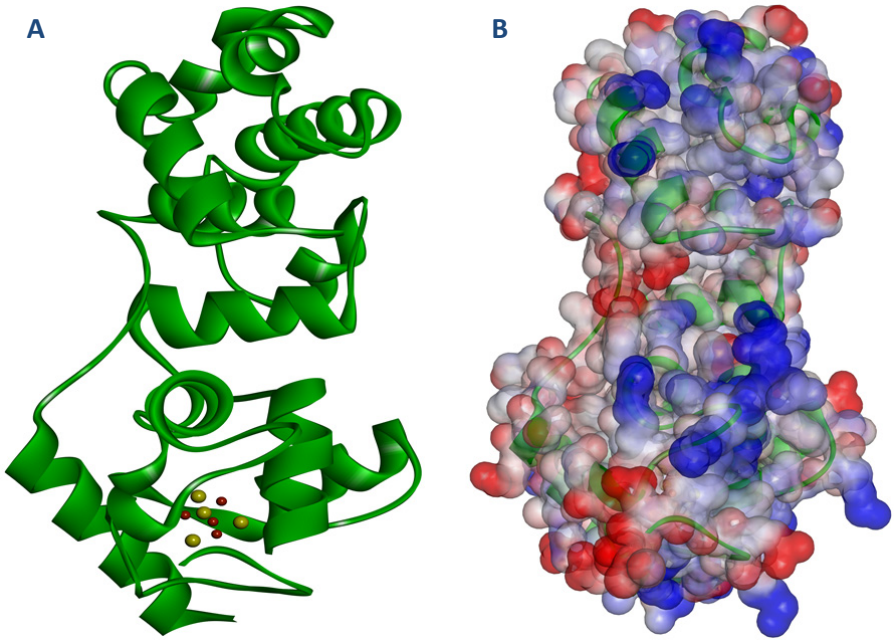

Figure 8.1 | Endo III 3D-structure (**A**) and its superficial electrostatic charge (**B**). The [4Fe-4S] cluster is represented in A, with the sulfur and iron atoms in yellow and red, respectively. In B, the positive area is represented in blue with a total of 27 positively charged residues (Arg + Lys). On the other hand, the negative area is represented in red with a total of 24 negatively charged residues (Asp + Glu). Both figures were made using Accelrys DS Visualizer software (v3.5.0.12158), available at http://accelrys.com/.

On this assumption, a whole set of electrochemical assays, in different conditions, were conducted, which involved different electrodes (both working and reference), different electrolytes, varying the protein concentration, the use of surface modifiers, promoters, etc., in order to obtain the electrochemical signal of Endo III (*vide* Appendix I).

In this chapter, all electrochemical assays were performed by cyclic voltammetry. This technique has the advantage of providing fast and direct measurements of the proteins redox properties and allows the use of wide range of potential windows. Through cyclic voltammetry it is also possible to obtain kinetic information on the redox centers [66].

Assays were performed in an electrochemical cell of one compartment with a three-electrodes (WE, RE and CE) configuration, inside a Faraday's box, at room temperature (Figure 8.2).

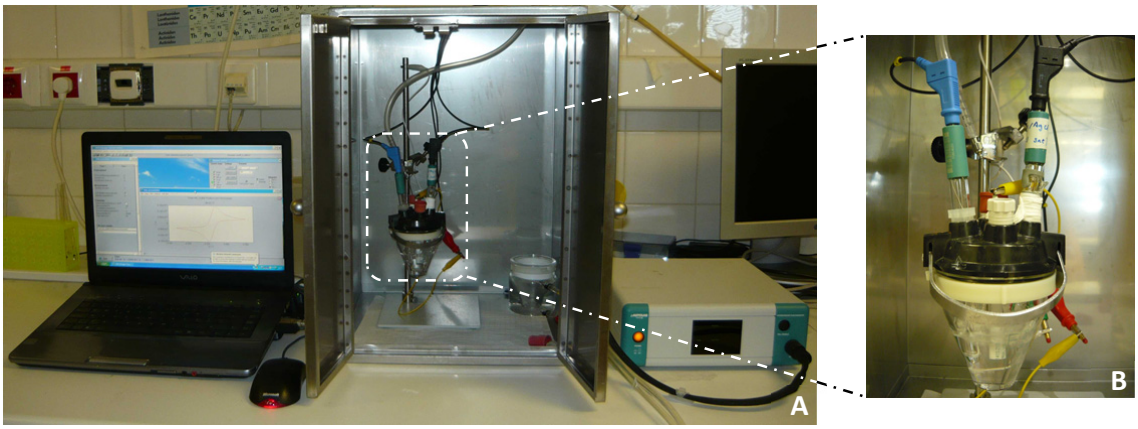

Figure 8.2 | A – Experimental setup used in electrochemical assays, consisting of a pc with GPES software, a potenciostat and a Faraday's box with the electrochemical cell inside. **B –** Electrochemical cell of one compartment with a three-electrodes configuration.

The electrolyte solutions were purged with Ar gas for at least 30 min to remove oxygen and kept under an Ar atmosphere during measurements. GPES (version 4.9, *Eco Chemie*) was used as the data acquisition software and assays were performed with a potenciostat "μAutolab Type III" (*Autolab*) and a potenciostat/galvanostat "Autolab 128N" (*Autolab*). All voltammograms began at the Open Circuit Potential (OCP) value and an initial negative (reductive) scan direction was established.

After trying the different approaches, the electrochemical signal of Endo III was obtained with the adsorption of 5 μL of this enzyme with a concentration of 183.88 μM onto the surface of a pyrolytic graphite (PG) electrode with prior co-adsorption of 3 μL of 2 mM neomycin (Figure 8.3). The pyrolytic graphite allows better results than normal graphite owing to the heating process that it suffers, which hardens the surface and leads to a greater homogeneity. Graphite has hydroxide and

carboxylate ions on its surface, which are formed by contact with water or oxygen. The negative charges of these ions form electrostatic bonds with positive charges of neomycin, promoting its adsorption onto the surface of the electrode.

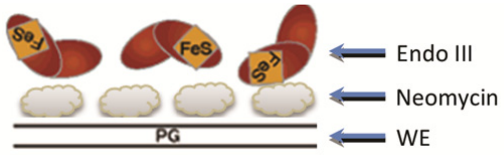

Figure 8.3 | Schematic representation of the methodology used in the electrochemical studies with Endo III on PG. Adapted from [33].

This assay and subsequent ones were performed in 0.1 M Tris-HCl, pH 7.1 + 0.1 M NaCl, against the reference electrode Ag/AgCl and with a platinum wire as the counter electrode. The supplementary NaCl was used as supporting electrolyte.

In contrast to what has been described in the literature [33], it was possible to obtain a direct electrochemical response of Endo III without modifying the electrode surface with DNA, which means that Endo III is electrochemically active. The voltammogram in Figure 8.4 demonstrates this finding.

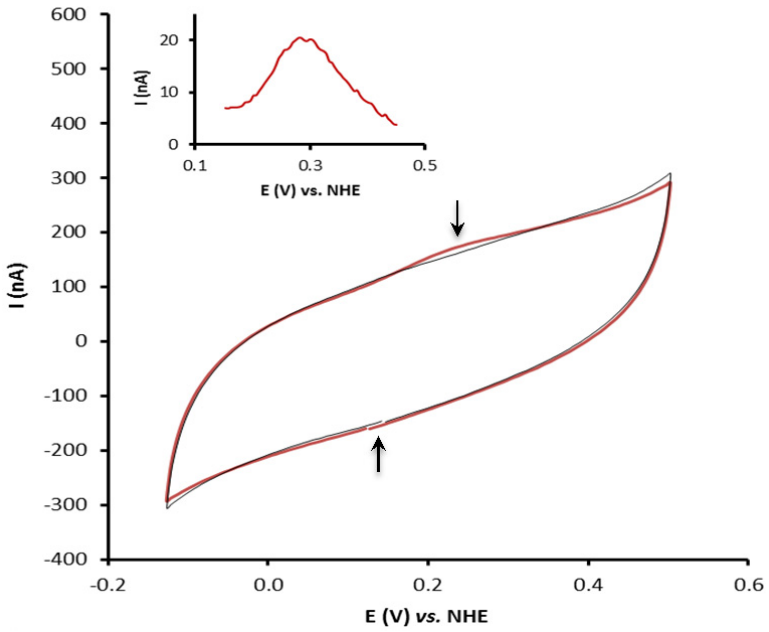

Figure 8.4 | Cyclic voltammogram of 183.88 μM Endo III (red line) and comparison with the blank (black line), obtained on bare PG at ν = 50 mV/s. All runs were performed in 0.1 M Tris-HCl, pH 7.1 + 0.1 M NaCl, using an electrochemical cell of one compartment with a three-electrodes configuration *versus* Ag/AgCl reference and Pt auxiliary. The arrows indicate the Endo III redox couple. Inset: blank subtraction in the anodic peak.

In Figure 8.4, a typical example of the obtained quasi-reversible redox couple is observed with a midpoint potential of 178 ± 9 mV *vs.* NHE. For this particular case, one can observe an anodic peak at 229 mV *vs.* NHE and a cathodic peak at 137 mV *vs.* NHE, both indicated with arrows. By comparison with the control and given that the protein does not contain any other electrochemically active metallic center in this potential window, this redox couple is assigned to the $[4Fe\text{-}4S]^{3+/2+}$ cluster redox process of Endo III adsorbed onto the electrode surface. The voltammetric results indicate that direct electron transfer between the redox center of adsorbed Endo III and the surface of the bare electrode had taken place. Furthermore, it is possible to conclude that Endo III is a HiPiP since the determined midpoint potential of Endo III is within the range reported in the literature for this type of [4Fe-4S] cluster-containing proteins, which is from +50 to +450 mV [29, 30].

8.1 Study of Endonuclease III system reversibility

The next step in the electrochemical characterization of Endo III was the diagnostic of the electrochemical system. Since this is not a bulk system and both electroactive species (oxidized and reduced Endo III) are adsorbed onto the WE surface, the diagnostic is conducted with the criteria for a thin layer electrochemical system, whose theory is similar to other non-diffusional system such as this one. In neither case there is any limitation from diffusion of electroactive species [67, 68].

The reversibility criteria are [67, 68]:

1. $I_p \alpha \nu$, the current peak varies with the scan rate
2. $\Delta E_p \alpha \nu$, there is no separation between the anodic and the cathodic current peaks
3. $I_{pa} / I_{pc} \approx 1$

The first criterion only applies for small scan rates, up to 50 mV/s, when a linear behavior is observed. Above that, the system deviates from linearity (due to increasing irreversibility) (Figure 8.5).

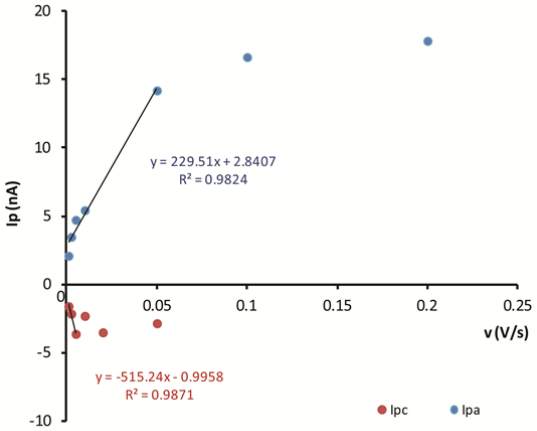

Figure 8.5 | Plot of current intensity *versus* applied scan rate.

The difference between the potential values of the anodic and the cathodic peaks, ΔE_p, also depends on the scan rate, exhibiting a linear behavior for scan rates in the range of 1 to 5 mV/s, (Figure 8.6 - A). Therefore, the second criterion is verified only in the supramentioned range.

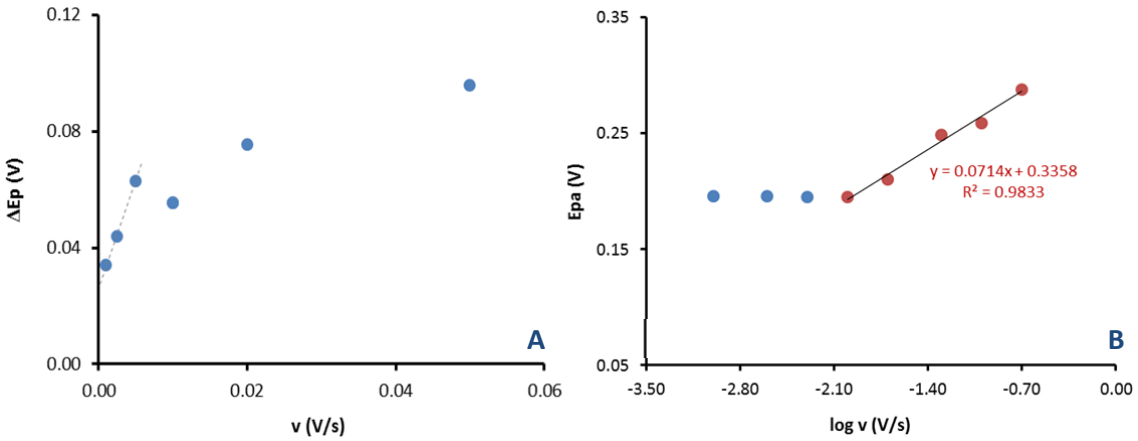

Figure 8.6 | A – Plot of potential difference *versus* applied scan rate. **B –** Plot of anodic potential *versus* logarithmic scan rate.

The slope of the plot E_{pa} *vs.* log ν (Figure 8.6 – B) is 71 ± 5 mV, which is close to the theoretical value of 60 mV for a reversible thin layer experimental system [69], and is indicative of a quasi-reversible system.

Overall, for low scan rates, the redox peak currents of Endo III increased linearly with increasing scan rate, and the peak-to-peak separation also increased (Figure 8.6 - A), indicating a surface-controlled process. Due to lack of definition of the voltammograms obtained for higher scan rates, is not possible to confirm if this behavior is maintained.

The determined I_{pa} / I_{pc} values were way higher than 1, and so the third criterion was not verified. This is mainly due to the fact that the cathodic peaks intensity is too small in comparison with the anodic ones, leading to higher I_{pa} / I_{pc} values. Major differences in faradaic and non-faradaic (capacitive) currents in the cathodic reaction may be an explanation for this result.

Since none of the early mentioned criteria is fully obeyed, it is possible to conclude that Endo III is not a reversible system, but most likely a quasi-reversible one.

8.2 Endonuclease III surface coverage

The degree of coverage of the WE surface was estimated through the surface concentration of electroactive adsorbed Endo III molecules (Γ, mol/cm^2). Γ was estimated by two methods:

1) $I_{pa} = f(\nu)$ slope,
2) Integration of the anodic peak, which equals the Q (charge) to be applied in Faraday's Laws of Electrolysis.

For method 1), the following equation was used [67]:

$$I_{pa} = \frac{n^2 F^2 A \Gamma \upsilon}{4RT} \tag{8.1}$$

where I_{pa} is the anodic peak current (A), n is the number of moles of electrons transferred per mole of electroactive species (mol^{-1}), A is the electrode area (cm^2), Γ is the surface concentration (mol/cm^2), ν is the scan rate (V/s), and R, T and F are gas, temperature and Faraday constant, respectively (R = 8.314 Jmol^{-1} K^{-1}, T = 293 K, F = 96485 C mol^{-1}).

Γ was estimated by using the slope of the linear equation of $I_{pa} = f(\nu)$ plot in Figure 8.6 and the equation 8.1. n equals 1 and the electrode area, 0.09 cm^2, was determined in Appendix J. Based on this method, the surface coverage of Endo III was estimated to be 2.67 x10^{-12} mol/cm^2.

For method 2), the following equation was used:

$$Q = A\, F\, n\, \Gamma \tag{8.2}$$

where Q is the total electric charge passed through the electroactive species (C), A is the electrode area, F is the Faraday constant, n is the number of moles of electrons transferred per mole of electroactive species and Γ is the surface concentration. This equation was derived from Faraday's

Laws of Electrolysis [70]. Q was obtained with the GPES software, through the integration of the anodic peak of Figure 8.5, and its value equals 2.147×10^{-8} C. Thus, based on this method, the surface coverage of Endo III was estimated to be 2.47×10^{-12} mol/cm^2, which is close to the value obtained by method 1).

Using the value of surface coverage obtained with method 2) and the Avogadro constant [71], the number of electroactive molecules of Endo III adsorbed onto the electrode surface was determined. For that purpose, equations 8.3 and 8.4 were merged to give rise to equation 8.5, which was used in the determination of the number of molecules.

$$\Gamma = \frac{n}{A} \tag{8.3}$$

$$N_A = \frac{N}{n} \tag{8.4}$$

$$N = \Gamma \, A \, N_A \tag{8.5}$$

where N is the number of molecules, Γ is the surface concentration (mol/cm^2), A is the electrode area (cm^2) and N_A is the Avogadro constant (6.022×10^{23} mol^{-1}). Thus, the number of electroactive molecules of Endo III adsorbed onto the electrode surface was determined to be 1.34×10^{11}.

The final step was to determine whether the adsorption of Endo III onto the electrode surface formed one or more layers. For that purpose, the total number of molecules of Endo III that can occupy the electrode surface was estimated. Since there is a considerable unpredictability regarding Endo III orientation upon deposition, horizontal and vertical orientations were considered. Their base areas, the ones nearer to the cluster, were calculated with the Accelrys DS Visualizer software (version 3.5.0.12158) (Figure 8.7), and the results obtained for one molecule of Endo III were 820.27 Å^2 and 480.42 Å^2 for the hypothetical horizontal and vertical orientations, respectively.

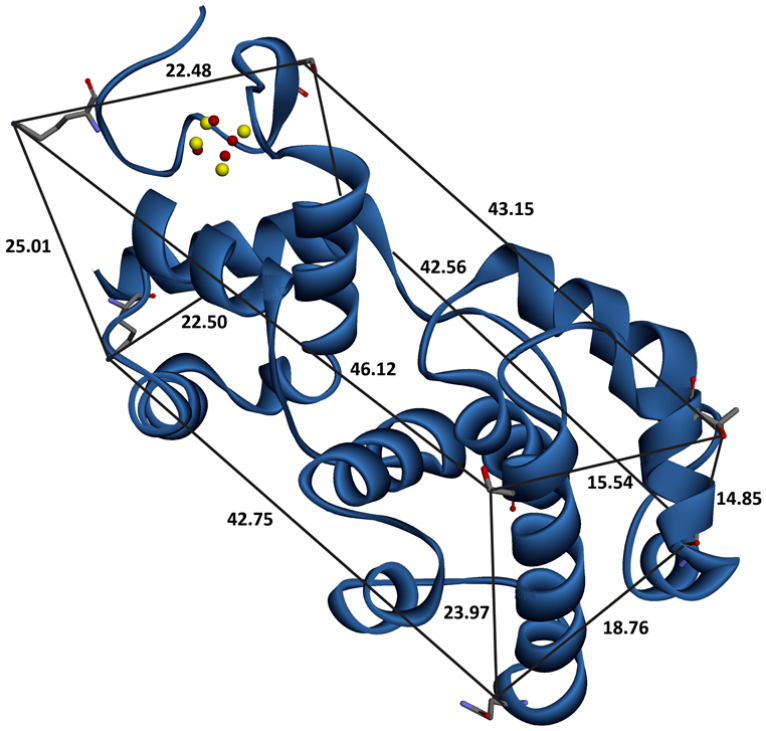

Figure 8.7 | Endo III surface area determination (PDB ID 2ABK) using Accelrys DS Visualizer software (version 3.5.0.12158), available at http://accelrys.com/.

Using the base areas obtained for one molecule and the electrode area, the total number of molecules of Endo III that can occupy the electrode surface was estimated to be 1.10×10^{12} and 1.87×10^{12}, in case of a horizontal and a vertical deposition, respectively.

The ratio between the number of electroactive molecules of Endo III adsorbed and the total number of molecules of Endo III that can occupy the electrode surface gives the percentage of coverage by this enzyme in the tested experimental conditions. The results are 12.18 % of coverage by a horizontal deposition and 7.17 % by a vertical deposition. Two possible explanations for these results are: a) few adsorbed molecules of Endo III are electrochemically active, or b) protein washing out when dipping the electrode in the electrolyte solution or upon sweep, by imposition of potential, both resulting in a submonolayer.

8.3 Electron transfer kinetics of Endonuclease III

Assays performed with a higher protein concentration adsorbed onto the electrode surface resulted in increased resistance, i.e., Endo III adsorption onto the electrode surface decreases conductivity. This result is shown in Figure 8.8, where one can observe a significant difference in resistance between the blank and Endo III voltammograms.

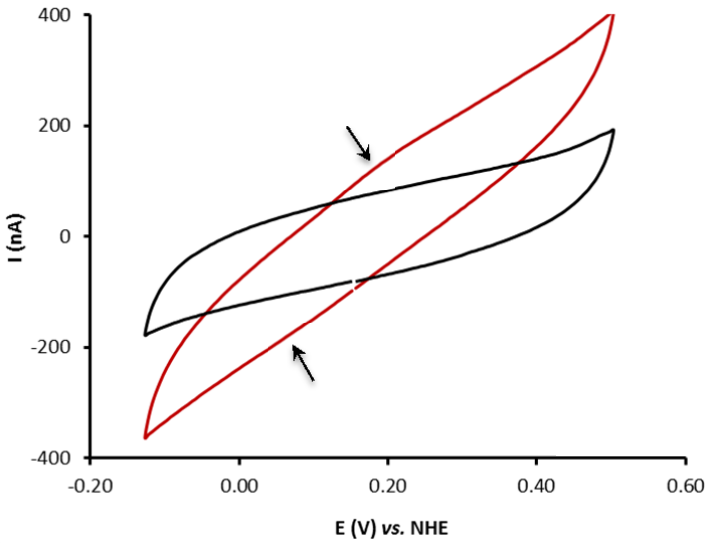

Figure 8.8 | Cyclic voltammogram of Endo III at higher concentration (314.71 μM, red line) and comparison with the blank (black line), obtained on bare PG at ν = 20 mV/s. All runs were performed in 0.1 M Tris-HCl, pH 7.1 + 0.1 M NaCl, using an electrochemical cell of one compartment with a three-electrodes configuration *versus* Ag/AgCl reference and Pt auxiliary. The arrows indicate the Endo III redox couple.

The observed resistance, together with the fact that Endo III capacitive current is high, leads to the conclusion that the enzyme itself is slightly non-conductive. This results in a slow electronic transfer, which is verified in the voltammograms shown in Figure 8.9 that were collected at lower scan rates, and in which better-defined redox peaks can be observed (when compared with the ones obtained with scan rates that are commonly used in characterization studies, such as 20 or 50 mV/s).

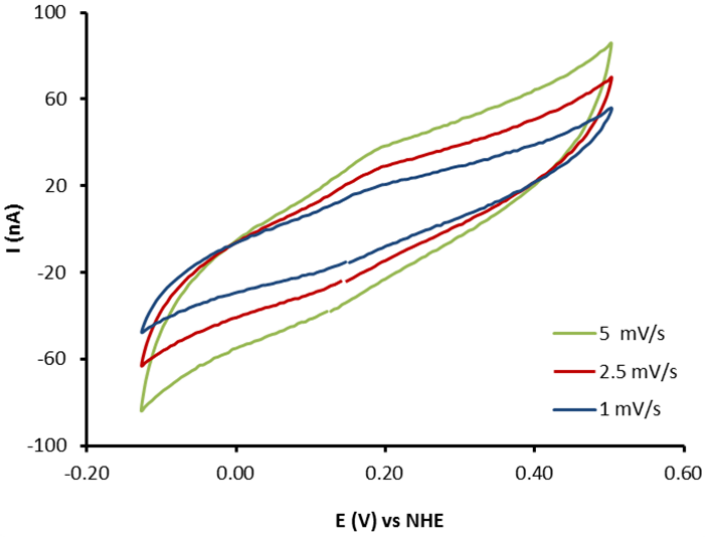

Figure 8.9 | Cyclic voltammograms of 188.83 μM Endo III, obtained at small scan rates on bare PG. Blue line, 1 mV/s; red line, 2.5 mV/s; green line, 5 mV/s. All runs were performed in 0.1 M Tris-HCl, pH 7.1 + 0.1 M NaCl, using an electrochemical cell of one compartment with a three-electrodes configuration *versus* Ag/AgCl reference and Pt auxiliary.

To prove that this electrochemical system has a slow electronic transfer, its heterogeneous electron-transfer rate constant was estimated using Laviron's mathematical approach for diffusionless electrochemical systems. Laviron derived general expressions for the linear potential sweep voltammetric response in the case of surface controlled electroactive species, when both the oxidized and the reduced forms are strongly adsorbed [69, 72]:

$$E_{pa} = E_0 + \frac{2.3RT}{(1-\alpha)nF} log \frac{(1-\alpha)}{m} \quad (8.6)$$

$$E_{pc} = E_0 - \frac{2.3RT}{\alpha nF} log \frac{\alpha}{m} \quad (8.7)$$

$$m = \frac{RTk_{sh}}{Fn\upsilon} \quad (8.8)$$

where α is the electron-transfer coefficient, n is the number of moles of electrons transferred per mole of electroactive species, m a parameter related to the peak-to-peak separation, and R, T and F are gas, temperature and Faraday constant, respectively.

From the experimental difference between the peak potential of the anodic and cathodic peaks, ΔE_p, and for a known α, the k_{sh} can be calculated. Two cases can be considered,

a) $\Delta E_p > 200/n$ mV,

b) $\Delta E_p < 200/n$ mV.

For case a), α can be calculated by the plot of $E_p - E_0 = f$ (log υ), which yields two straight lines with slopes equal to -2.3RT/αnF and 2.3RT/(1-α)nF for the cathodic and anodic peaks, respectively. It is, then, possible to calculate k_{sh} from the equation [69]:

$$k_{sh} = \frac{\alpha nF\upsilon_c}{RT} = \frac{(1-\alpha)nF\upsilon_a}{RT} \quad (8.9)$$

For case b), the determination of α cannot be precise, but for values close to 0.5 (between 0.3 and 0.7) the k_{sh} can still be determined with a negligible relative error (at the most about 6 % when α = 0.5). From a theoretical curve of $n\Delta E_p = f$ (1/m) (Figure 8.10), for a specific α and using the experimental ΔE_p values, the m parameter can be found. Then, using equation 8.8, k_{sh} is estimated for each scan rate.

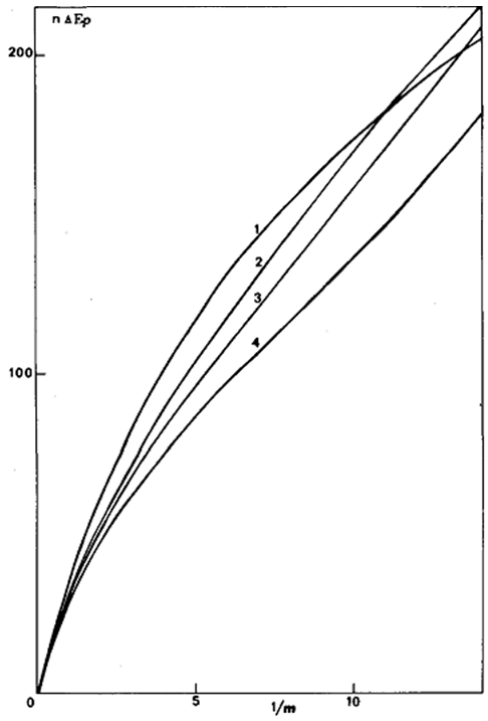

Figure 8.10 | Variations of $n\Delta E_p$ with 1/m. (1) α = 0.5, (2) α = 0.8, (3) α = 0.85 (4) α = 0.9 [69].

Due to the obtained ΔE_p values ($< 200/n$ mV), k_{sh} was determined according to case b). Assuming α = 0.5 and for n = 1, a k_{sh} of 0.50 ± 0.03 s^{-1} at a scan rate of 50 mV/s was estimated (maximum value in the experimental conditions tested, Figure 8.11). This value of k_{sh} confirms that this electrochemical system has a slow electronic transfer kinetic, as reported in the literature [34–36].

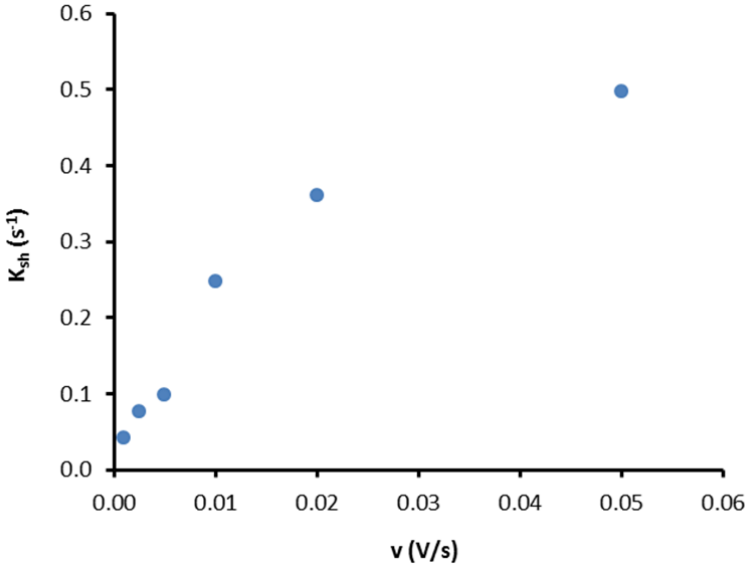

Figure 8.11 | Plot of estimated heterogeneous electron-transfer rate constant *versus* applied scan rate.

Chapter 9 Electrochemical behavior of Endonuclease III, plasmid DNA and protein-DNA complex, before and after UV irradiation

In this chapter, the results on the electrochemical behavior of recombinant Endo III, plasmid DNA and protein-DNA complex, before and after UV irradiation, will be analyzed.

All trademarks not mentioned, instrumentation and protocols used in this chapter are described in the Appendices section.

The UV exposure and the electrochemical assays were conducted with the same equipment as in the equivalent assays described in previous chapters, with concentrations of Endo III and pUC18 of 6.18 μM and 12.36 nM, respectively. The chosen protein/DNA molar ratio (500:1) guarantees that most of pDNA is bound to Endo III, i.e., that the complex is formed after 2 h of incubation, as shown in Figure 7.1. The complex UV irradiation (20 min at 10 cm of the source, corresponding to a dose of 8.79 kJ) preceded all electrochemical assays. All samples were prepared immediately prior to use.

9.1.1 Cyclic voltammetry assays

The first comparison made was between Endo III before and after UV irradiation. The only redox couple observed in both voltammograms (Figure 9.1) is assigned to the $[4Fe\text{-}4S]^{3+/2+}$ cluster redox process of Endo III adsorbed onto the electrode surface.

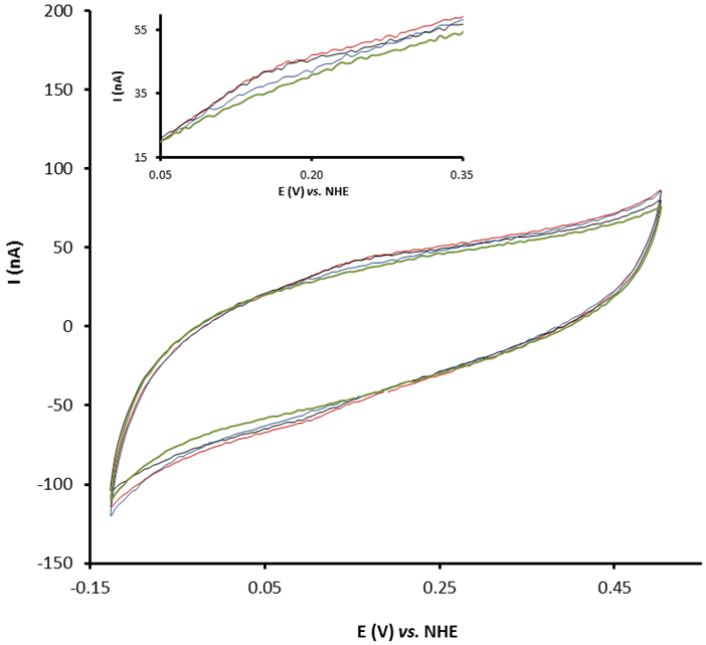

Figure 9.1 | Cyclic voltammograms of the 6.18 μM Endo III sample, before and after UV irradiation, obtained on bare PG at ν = 5 mV/s. Red line, Endo III without irradiation; black line, irradiated Endo III; blue line, blank without irradiation; green line, irradiated blank. All runs were performed in 0.1 M Tris-HCl, pH 7.1 + 0.1 M NaCl, using an electrochemical cell of one compartment with a three-electrodes configuration *versus* Ag/AgCl reference and Pt auxiliary. Inset: magnifying of the anodic process (0.05 to 0.35 V).

The determined midpoint potentials are 118 and 110 mV *vs.* NHE for the non-irradiated and irradiated protein, respectively. This small difference in potential brings up the question whether this is a real shift due to the effect of UV radiation at the level of protein conformation or coordination (metallic center) or if this value is within experimental error and, consequently, has no physical significance and, therefore, no shift should be considered. Further assays are needed to verify these hypotheses.

The next comparison was between pUC18 before and after being irradiated. Aside from the difference in the capacitive current shape, there are no major differences between the blanks and the pUC18 samples' voltammograms (Figure 9.2). Indeed, there are no faradaic currents present, as expected, since the electrochemical signal of DNA purine bases oxidation appears at a potential above the limit of the studied potential window.

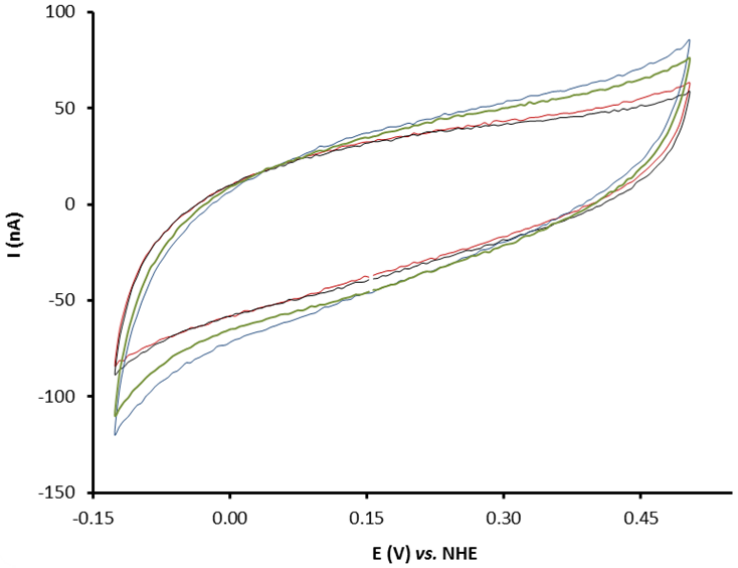

Figure 9.2 | Cyclic voltammograms of the 12.36 nM pUC18 sample, before and after UV irradiation, obtained on bare PG at ν = 5 mV/s. Red line, pUC18 without irradiation; black line, irradiated pUC18; blue line, blank without irradiation; green line, irradiated blank. All runs were performed in 0.1 M Tris-HCl, pH 7.1 + 0.1 M NaCl, using an electrochemical cell of one compartment with a three-electrodes configuration *versus* Ag/AgCl reference and Pt auxiliary.

The electrochemical characterization of Endo III and pDNA, before and after irradiation, was followed by the electrochemical characterization of the protein-DNA complex, also before and after irradiation (Figure 9.3).

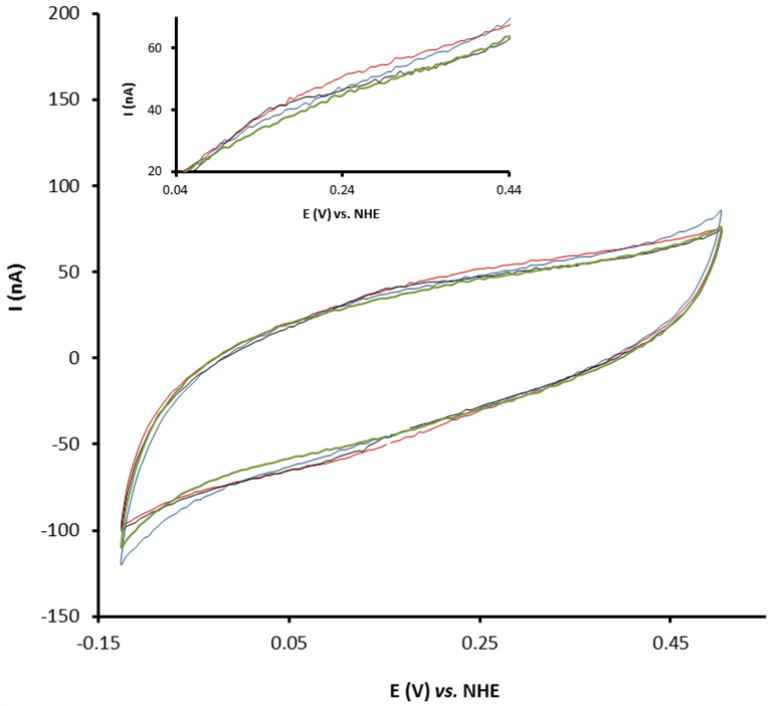

Figure 9.3 | Cyclic voltammograms of the adsorbed complex, before and after UV irradiation, obtained on PG at ν = 5 mV/s. Red line, complex without irradiation; black line, irradiated complex; blue line, blank without irradiation; green line, irradiated blank. All runs were performed in 0.1 M Tris-HCl, pH 7.1 + 0.1 M NaCl, using an electrochemical cell of one compartment with a three-electrodes configuration *versus* Ag/AgCl reference and Pt auxiliary. Inset: magnifying of the anodic process (0.04 to 0.44 V).

From Figure 9.3, one can observed that the complex redox couple presents more negative potential after exposure to UV radiation, similar to the one found for Endo III. The determined midpoint potentials are 137 and 112 mV *vs.* NHE for the non-irradiated and irradiated protein-DNA complex, respectively. The fact that irradiated complex and Endo III have similar midpoint potentials brings up the question about the stability of the complex after UV irradiation. The observed difference in the midpoint potential should be attributed to the DNA-protein complex dissociation due to UV irradiation, since the existence of a complex should not give rise to a redox potential similar to the free Endo III as it is observed for the non-irradiated complex. Thus, one should consider the hypothesis that the electrochemical redox couple observed after UV irradiation may be due to free Endo III.

The obtained voltammograms were overlaid in order to analyze the shift of the characteristic redox couple of Endo III.

Regarding the assays without irradiation (Figure 9.4), Endo III binding to pDNA seems to promote a positive shift of 19 mV in the characteristic redox couple of Endo III. The already mentioned midpoint potentials are 118 and 137 mV *vs.* NHE for unbounded Endo III and for protein-complex couple, respectively.

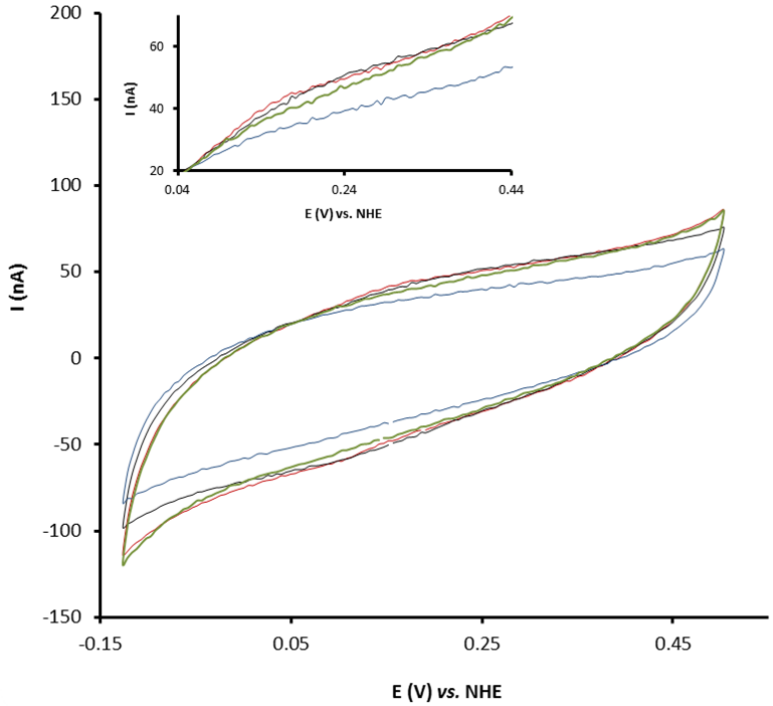

Figure 9.4 | Comparison of the cyclic voltammograms of Endo III, pUC18 and complex samples, before UV irradiation, obtained on PG at ν = 5 mV/s. Red line, Endo III; black line, complex; blue line, pUC18; green line, blank. All runs were performed in 0.1 M Tris-HCl, pH 7.1 + 0.1 M NaCl, using an electrochemical cell of one compartment with a three-electrodes configuration *versus* Ag/AgCl reference and Pt auxiliary. Inset: magnifying of the anodic process (0.04 to 0.44 V).

At first sight, it seems that there is no shift in the characteristic redox couple of Endo III, when comparing the assays of the irradiated Endo III and complex (Figure 9.5). Indeed, the determined midpoint potentials are 110 and 112 mV *vs.* NHE for unbounded Endo III and for protein-complex couple, respectively, which difference is within the experimental error (minimum 5 mV).

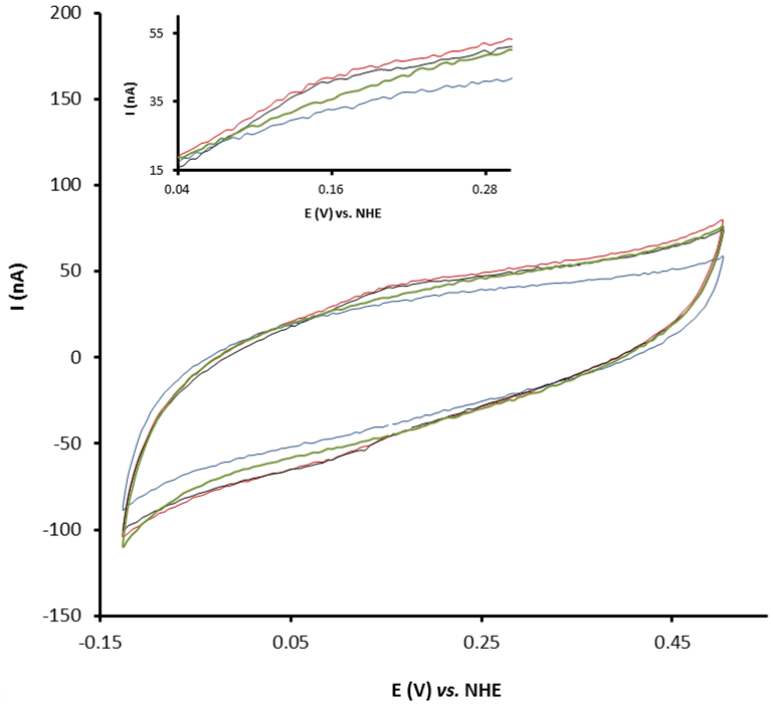

Figure 9.5 | Comparison of the cyclic voltammograms of Endo III, pUC18 and complex samples, after UV irradiation, obtained on PG at ν = 5 mV/s. Red line, Endo III; black line, complex; blue line, pUC18; green line, blank. All runs were performed in 0.1 M Tris-HCl, pH 7.1 + 0.1 M NaCl, using an electrochemical cell of one compartment with a three-electrodes configuration *versus* Ag/AgCl reference and Pt auxiliary. Inset: magnifying of the anodic process (0.04 to 0.30 V).

As discussed above, from the electrochemical results it appears that the irradiated complex presents similar features to the irradiated Endo III. This may point to a complex instability resulting from UV irradiation and potential imposition.

In addition, results obtained from supplementary EMSAs performed with these exact experimental conditions (complex incubation for 2 h before irradiation) showed that, with increasing irradiation time, complex migration profile changes to the point that significant amount of protein is no longer bound to DNA (Figure 9.6). The gel represented in Figure 9.6 was stained both for DNA and protein and from superimposition of the two different stainings it is possible to assume that, up to 10 min of irradiation, the complex has a similar behavior to the non-irradiated one, while from 20 min irradiation a white smear (protein staining) arises. With 30 min of irradiation, only a small amount of complex is observed when compared with the non-irradiated one. Besides, in the protein staining, a

band with similar migration profile to the free Endo III is observed. As in the electrochemical assays, also here one can speculate that a) the complex is effectively affected by UV radiation and is, therefore, destroyed or b) with 20 min of irradiation structural modifications occur in a fashion that affects the stability and, therefore, within the timescale of the EMSA, part of the complex may fragment. However, these assays were performed numerous times without desirable reproducibility, which is another evidence for the complex instability hypothesis.

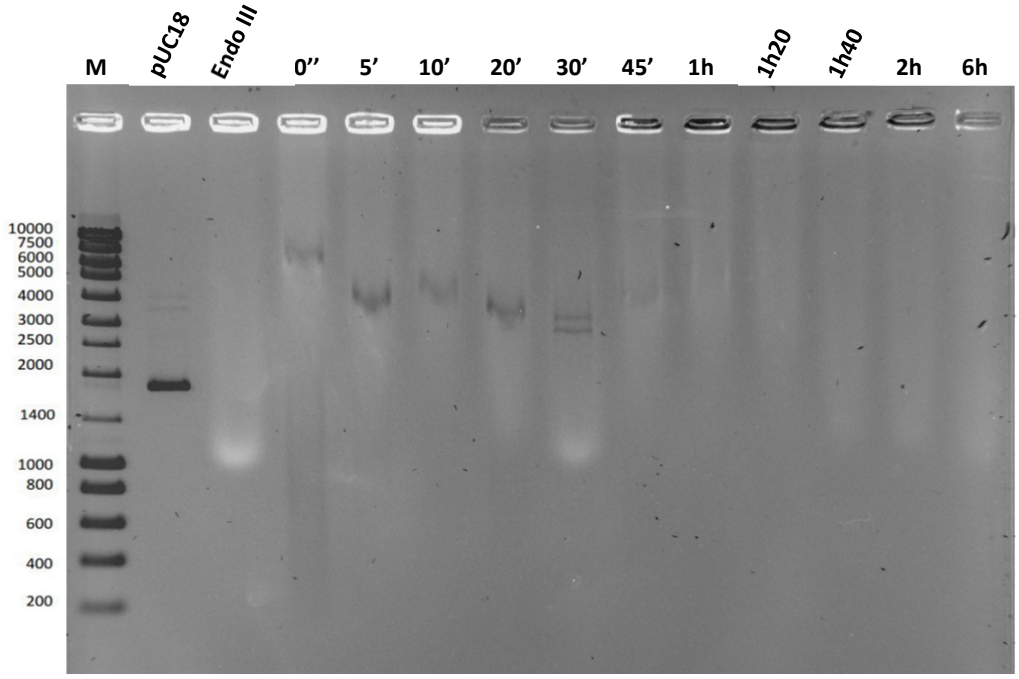

Figure 9.6 | Superimposition of protein and DNA stainings of the gel obtain by an EMSA performed with protein-DNA complex that was exposed to UV radiation for different periods of time (indicated on top of the lanes). The binding buffer was 0.1 M Tris-HCl, pH 7.1. The electrophoretic mobilities were assessed by 1 % agarose gel electrophoresis (1 h 45 min, 80 V). The gel was stained with SYBRSafe (for DNA) and with Coomassie Brilliant Blue (for protein). **M** – NZYDNA Ladder III Standard.

9.1.2 Differential pulse voltammetry assays

The previous assays were also performed by Differential Pulse Voltammetry (DPV), which is a pulse technique. This type of technique differs from the normal voltammetry because a potential pulse is applied. This base potential is incremented between pulses, the amplitude increments always being equal (Figure 9.7) [67].

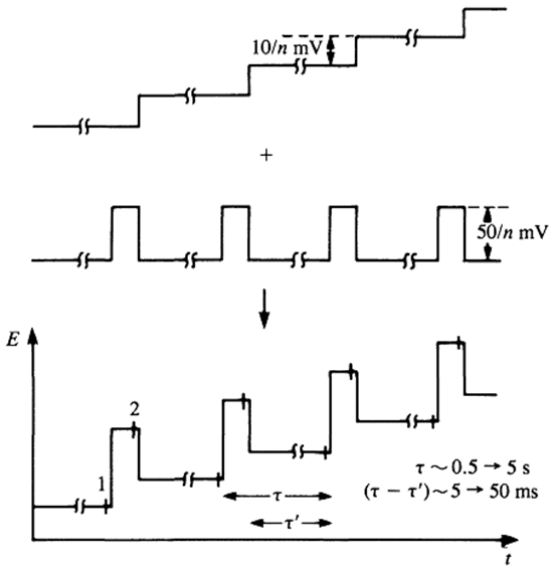

Figure 9.7 | Scheme of application of potentials in DPV [67].

After each application of a potential pulse, the capacitive current decays faster than the faradaic current. Thus, the current is sampled twice, immediately before pulse application and at the end of the pulse, when the charging current has already decayed. The subtraction of the currents allows an effective correction of the contribution of the charging background current and the result is a differential pulse voltammogram. This technique has, therefore, the advantage of providing greater sensitivity owing to an increase in the ratio between the faradaic and not faradaic (capacitive) currents [67, 73].

The differential pulse voltammogram is similar to the first derivative of a conventional voltammogram, which is a peak. The peak potential, E_p, can be approximately identified with $E_{1/2}$ [67]. With only the reduced (positive sign) or only the oxidized (negative sign) form initially present,

$$E_{max} = E_{1/2} \pm \frac{\Delta E}{2} \quad (9.1)$$

where ΔE is the pulse amplitude.

The same comparisons were made and the results of these assays are similar to those obtained with Cyclic Voltammetry. Midpoint potentials of the following assays were determined using equation 9.1.

The midpoint potentials of the characteristic peak of unbounded Endo III (Figure 9.8) are 117 and 107 mV *vs.* NHE for the non-irradiated and irradiated protein, respectively. This corresponds to a negative shift of 10 mV.

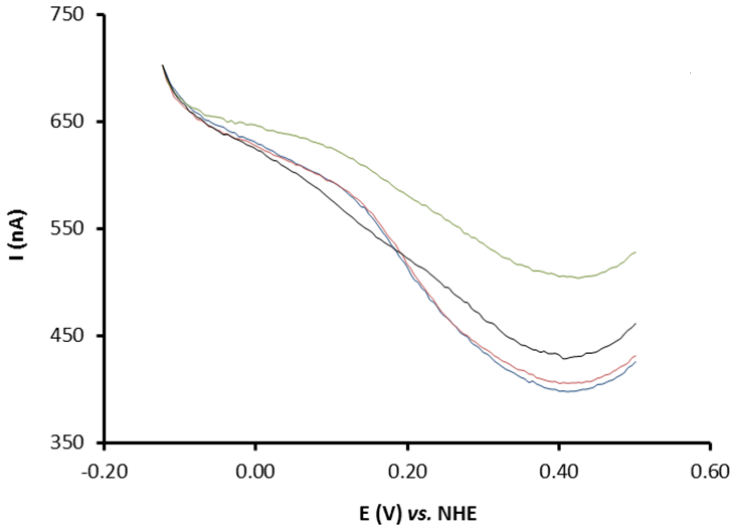

Figure 9.8 | Differential pulse voltammograms of the 6.18 μM Endo III sample, before and after Uv irradiation, obtained on PG, with 25 mV pulse amplitude and 5 mV step potential. Blue line, irradiated Endo III; red line, Endo III without irradiation; green line, irradiated blank; black line, blank without irradiation. All runs were performed in 0.1 M Tris-HCl, pH 7.1 + 0.1 M NaCl, using an electrochemical cell of one compartment with a three-electrodes configuration *versus* Ag/AgCl reference and Pt auxiliary.

Observing Figure 9.9, one can see a significant difference in the DPV's of non-irradiated and irradiated pUC18 and blank.

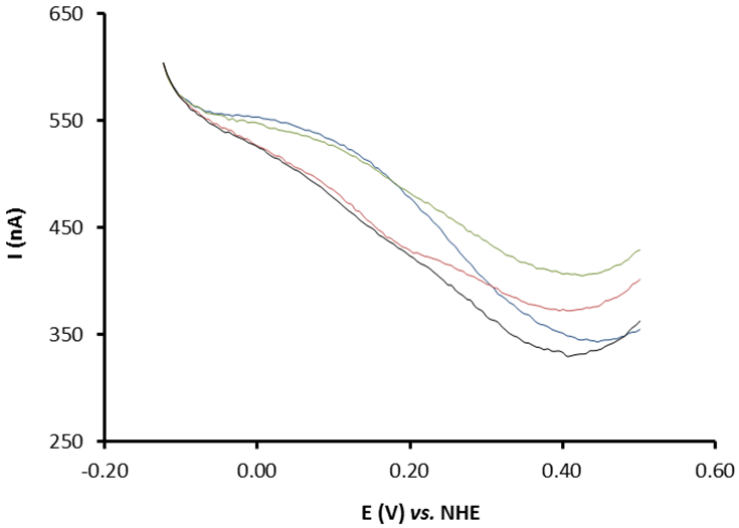

Figure 9.9 | Differential pulse voltammograms of the 12.36 nM pUC18 sample, before and after UV irradiation, obtained on PG, with 25 mV pulse amplitude and 5 mV step potential. Blue line, irradiated pUC18; red line, pUC18 without irradiation; green line, irradiated blank; black line, blank without irradiation. All runs were performed in 0.1 M Tris-HCl, pH 7.1 + 0.1 M NaCl, using an electrochemical cell of one compartment with a three-electrodes configuration *versus* Ag/AgCl reference and Pt auxiliary.

This difference is clearly due to the exposure to UV radiation. Even though no assays have been yet conducted to understand these processes, there is a possibility that this phenomenon is associated with the formation of radicals.

The midpoint potentials of the complex peak (Figure 9.10) are 132 and 112 mV *vs.* NHE for the assay without and with irradiation, respectively. This negative shift of 20 mV is similar to the one obtained with cyclic voltammetry for the same assay; therefore, the same justification applies.

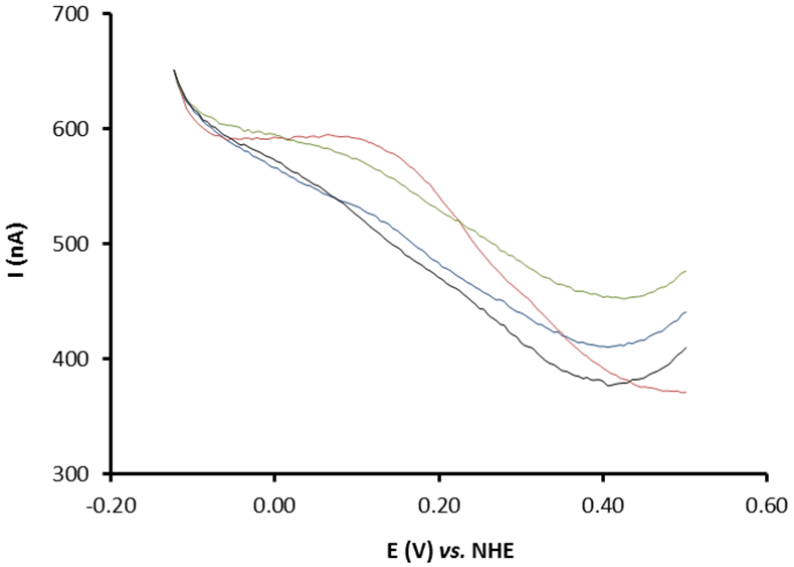

Figure 9.10 | Differential pulse voltammograms of the adsorbed complex, before and after UV irradiation, obtained on PG, with 25 mV pulse amplitude and 5 mV step potential. Blue line, irradiated complex; red line, complex without irradiation; green line, irradiated blank; black line, blank without irradiation. All runs were performed in 0.1 M Tris-HCl, pH 7.1 + 0.1 M NaCl, using an electrochemical cell of one compartment with a three-electrodes configuration *versus* Ag/AgCl reference and Pt auxiliary.

The voltammograms obtained by DPV were also overlaid in order to analyze the shift of the characteristic peak of Endo III.

For better visualization and comparison of Endo III and protein-DNA complex peak potentials, voltammograms were processed, using a baseline correction and the resulting peaks were normalized.

Regarding the assays without irradiation, Endo III binding to pDNA (green line) promotes a positive shift of 15 mV in the characteristic peak of Endo III (red line), which is clearly shown in the inset of Figure 9.11. The aforementioned midpoint potentials are 117 and 132 mV *vs.* NHE for unbounded Endo III and for protein-complex couple, respectively.

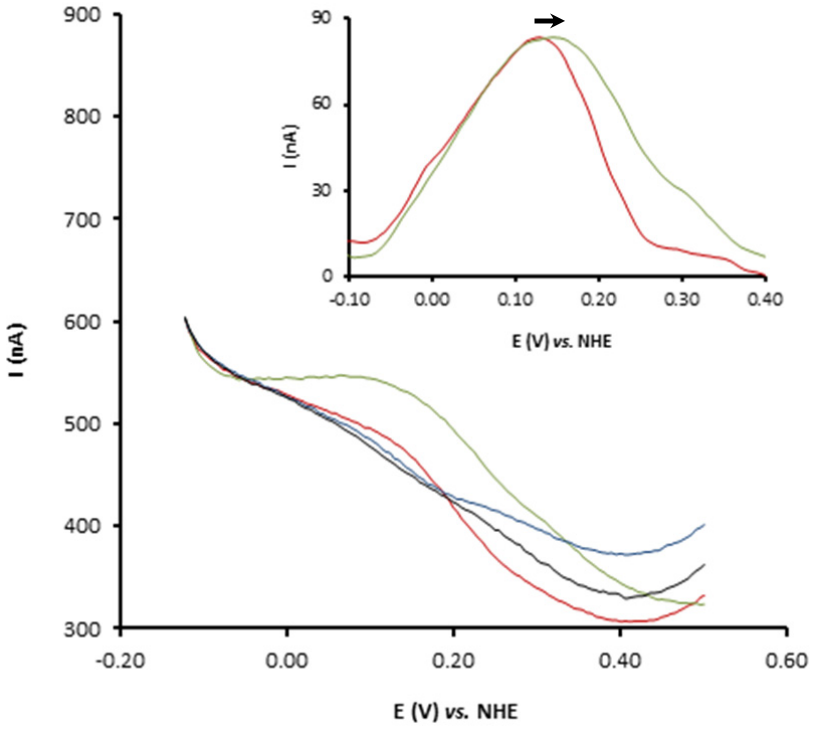

Figure 9.11 | Comparison of the differential pulse voltammograms of Endo III, pUC18 and protein-DNA complex samples, before UV irradiation, obtained on PG, with 25 mV pulse amplitude and 5 mV step potential. Red line, Endo III; green line, complex; blue line, pUC18; black line, blank. All runs were performed in 0.1 M Tris-HCl, pH 7.1 + 0.1 M NaCl, using an electrochemical cell of one compartment with a three-electrodes configuration *versus* Ag/AgCl reference and Pt auxiliary. Inset: normalized baseline correction (1.6x amplified) for better visualization and comparison of Endo III and complex peak potentials. The arrow indicates the shift direction.

More subtle is the positive shift of 5 mV between Endo III and complex peaks, after UV irradiation, shown in the inset of Figure 9.12. This behavior was previously observed in the cyclic voltammogram for the same conditions (Figure 9.5), so the same hypotheses apply.

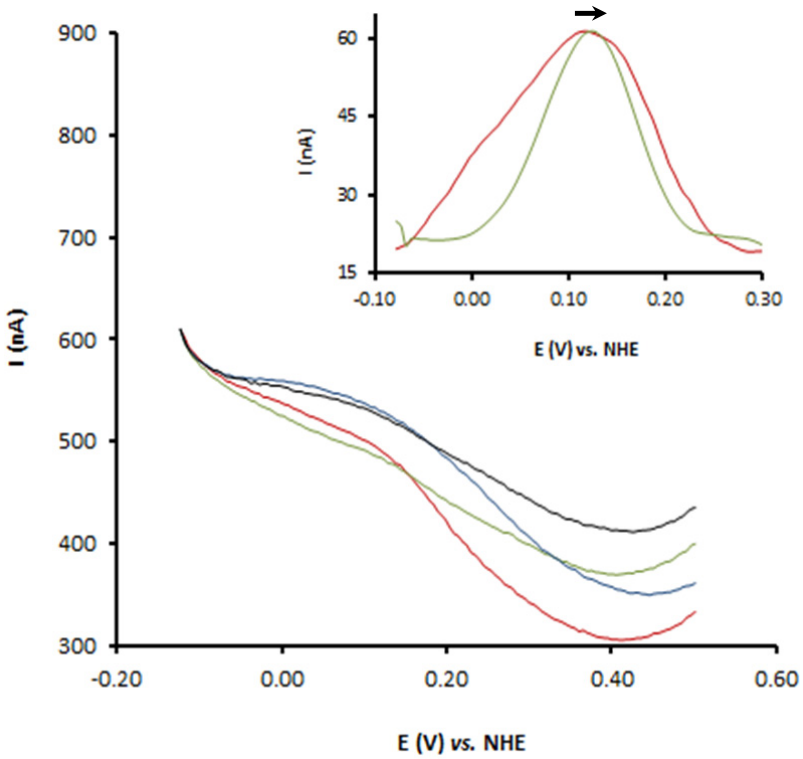

Figure 9.12 | Comparison of the differential pulse voltammograms of Endo III, pUC18 and protein-DNA complex samples, after UV irradiation, obtained on PG, with 25 mV pulse amplitude and 5 mV step potential. Red line, Endo III; green line, complex; blue line, pUC18; black line, blank. All runs were performed in 0.1 M Tris-HCl, pH 7.1 + 0.1 M NaCl, using an electrochemical cell of one compartment with a three-electrodes configuration *versus* Ag/AgCl reference and Pt auxiliary. Inset: normalized baseline correction (4x amplified) for better visualization and comparison of Endo III and complex peak potentials. The arrow indicates the shift direction.

Table 9.1 summarizes all midpoint potentials obtained by cyclic voltammetry and differential pulse voltammetry, in the different electrochemical assays.

Table 9.1 | Summary table of the midpoint potentials obtained by CV and DPV.

	$E^{o'}$ (mV *vs.* NHE)		
	CV	**DPV**	**CV (literature)***
Endo III without irradiation	118	117	250 (anodic)
Complex without irradiation	137	132	20
Endo III irradiated	110	107	-
Complex irradiated	112	112	-

* From Gorodetsky *et al* [33].

The midpoint potential determined for the direct electrochemical response of Endo III unbound to DNA, in this and in the previous chapter, is 118 and 178 mV *vs*. NHE, respectively. This shift in potential may be associated with slighly different experimental conditions used in these two assays. Indeed, to fullfill the experimental conditions used in the EMSAs (Chapter 7), in the set of assays performed in this chapter a different concentration of Endo III (6.18 μM) was used and the enzyme was incubated for 2 h, at room temperature. The altered midpoint may result from the incubation step. Further assays are needed to clarify this issue.

The midpoint potentials obtained by CV in this work are different from those found in the literature [33] (Table 9.1). The most likely explanation for the disparity are the different experimental conditions used, for instance, the use of a DNA-modified electrode (literature) *versus* a bare electrode (in this work).

As stated in Chapter 1, from observation of Figure 1.16 (Cyclic voltammetry assay of Endo III on a bare HOPG electrode) it seems that a cathodic peak is present around 50 mV *vs*. NHE, although it is not mentioned in the original paper. Since reported anodic peak is 250 mV *vs.* NHE, the midpoint potential for this redox couple would be around 150 mV *vs.* NHE, which is close to the midpoint determined in this work, given the associated errors.

Although more assays are needed for a better understanding of the phenomenon, it is worth noting that in the experimental conditions used it was possible to observe that protein-DNA complex formation promotes a positive shift in the characteristic redox couple of Endo III, in contrast to what was reported in the literature (negative shift).

Chapter 10 Conclusions

In this work, *E. coli* Endo III was overexpressed in *E. coli* and purified with a high degree of purity and in a fully-loaded form (four Fe ions per protein molecule). pUC18 plasmid was isolated and purified with a high degree of purity as well. This plasmid was successfully linearized with the restriction enzyme *Eco*R I.

Results of linear pDNA UV irradiation showed that over irradiation time some of pDNA molecules suffer nicks and double strand breaks, leading to the molecule's fragmentation. On the other hand, supercoiled pDNA UV irradiation led to the conversion of this form to the linear form, indicating once again that UV radiation cause double strand breaks in the DNA molecule. Total conversion occurred between 1 h 20 min and 1 h 40 min of UV radiation exposure, corresponding to radiation doses of 35.15 and 43.94 kJ, respectively.

Electrophoretic results of Endo III exposure to UV radiation showed that above 45 min of UV irradiation (19.77 kJ), a band with approximately twice the molecular mass of the one corresponding to monomeric Endo III starts to appear, with concomitant decrease in the monomeric Endo III band intensity. This behavior may be due to the formation of a covalent bond among Endo III protein monomers, probably between two tyrosyl radicals, which are formed when the polypeptide chain tyrosines residues are exposed to UV radiation. The UV-Vis spectrum of irradiated Endo III revealed significant modifications after 45 min of UV irradiation, with a decrease in the intensity of the absorption peak at 410 nm. This result raised two possibilities: a) UV radiation led to the destruction of the Fe-S bonds; b) UV radiation led to a different redox state of the [4Fe-4S] cluster. Further studies involving Mössbauer spectroscopy are planned to follow the chemical modification in the [4Fe-4S] cluster.

EMSAs with protein-DNA complex showed that Endo III binding to pDNA promotes a retardation of the free supercoiled DNA band, which is indicative of Endo III-DNA complex(es) formation. EMSAs also showed that Endo III is able to bind both linear and supercoiled pDNA, with K_d's of 0.28 ± 0.09 and 0.85 ± 0.13 μM, and n values of 1.68 ± 0.30 and 1.63 ± 0.22, respectively. These results are indicative of a higher Endo III affinity to linear pDNA than to its supercoiled form and a positive cooperativity on Endo III binding to both pDNA forms.

On the other hand, EMSAs performed with pDNA complexed with protein irradiated for 45 min (19.77 kJ) revealed that although shift occurred, the complexes formed were unstable and dissociated during electrophoresis. The reduced affinity of Endo III for DNA is possibly due to partial loss of the FCL motif resulting from a higher exposure time to UV radiation. This is consistent with what was concluded for Endo III UV irradiation results, where the formation of Endo III dimers is proposed. This event most likely modifies or destroys protein's three-dimensional structure in a

fashion that does not allow a stable ligation to DNA molecules. Moreover, it was possible to observe the formation of aggregates at higher protein/DNA molar ratios that were retained in the well, which reinforces the thesis that some Endo III molecules suffered some type of conformational change, probably unfolding, due to UV radiation exposure. After 6 h of irradiation (158.18 kJ) no shift occurred, i.e., no complexes were formed. This result led to the conclusion that Endo III molecules were irreversibly damaged.

Direct electrochemical response of Endo III unbound to DNA was observed on a pyrolytic graphite electrode by cyclic and differential pulse voltammetry. For the first time, without the presence of DNA, it was possible to observe a quasi-reversible redox couple displaying a midpoint potential of 178 ± 9 mV *vs.* NHE. This redox couple was attributed to the $[4Fe\text{-}4S]^{3+/2+}$ cluster redox process of Endo III adsorbed onto the electrode surface. The estimated k_{sh} of 0.50 ± 0.03 s^{-1} confirmed that this electrochemical system has a slow electronic transfer kinetic. For low scan rates, the redox peak currents of Endo III increased linearly with increasing scan rate, and the peak-to-peak separation also increased, indicating a diffusionless electrochemical system.

The effects of 20 min of UV radiation exposure (corresponding to a dose of 8.79 kJ), both on free Endo III and Endo III-DNA complex, assessed by cyclic voltammetry, are summarized in Figure 10.1.

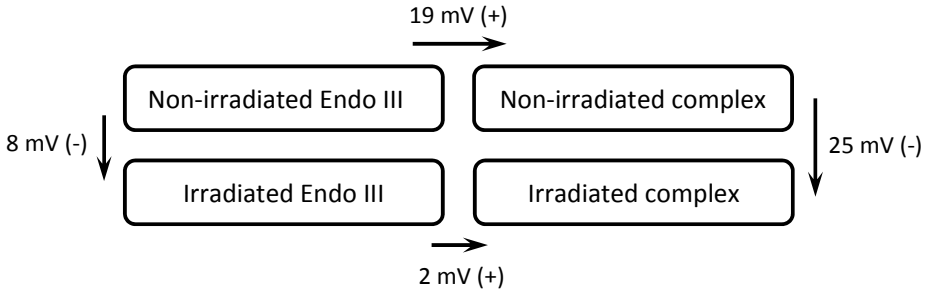

Figure 10.1 | Effects of 20 min of UV radiation exposure both on free Endo III and Endo III-DNA complex. The presented potential shifts were obtained by cyclic voltammetry, at ν = 5 mV/s. **(+)**, positive shift; **(-)**, negative shift.

Although only small differences are observed in the UV spectrum and SDS-PAGE gel of irradiated Endo III and in the EMSA gel of irradiated protein-DNA complex after 20 min of UV irradiation (when compared to non-irradiated entities), in the electrochemical assays these differences, represented by deviations in potential of about 20 mV, are observed between non-irradiated Endo III and protein-DNA complex, and non-irradiated and irradiated complex.

As discussed in Chapter 9, the observed shift in potential between both non-irradiated Endo III and protein-DNA complex assays may be due to conformational changes at the protein level arising

from DNA binding. On the other hand, the difference observed between non-irradiated and irradiated complex may be associated with complex instability resulting from UV irradiation and potential imposition, since in this experiment it was the complex that was irradiated after 2 h of incubation, rather than Endo III alone. Thus, these changes may lead to a complex conformation in which the protein behavior is similar to the free Endo III, or to the complex dissociation, which explain the potential obtained.

Further electrochemical assays are needed either to understand/clarify the obtained results and/or to test for reproducibility and obtain statistic relevance.

Overall, one can speculate that, at least for this type of UV radiation, both protein and DNA molecules are affected and show evidences of structural damage. This may lead one to believe that in cells (or living organisms) the deleterious effect of radiation does not only promote damage to DNA, leading, for instance, to mutations or cell death, but also to the repair mechanisms that were supposed to overcome those damages. Indeed, the results obtained in this work indicate that Endo III function is compromised after 45 min of exposure to UV radiation, corresponding to a dose of 19.77 kJ.

These findings lead to further investigation, where other sources of radiation may be used, together with different techniques, in order to identify mechanisms by which damages occur and also the minimum exposition doses that lead to those damages.

Chapter 11 Future work

The studied system proved to be highly complex. Therefore, further assays and the use of complementary techniques would be needed for a deeper understanding of this system. Possible paths for a more detailed study are:

- Perform further electrochemical assays for the best experimental conditions to test for reproducibility and obtain statistic relevance;
- Perform electrochemical assays with different exposure times to UV radiation and protein/DNA molar ratios, to test the potential shifts between all the proposed hypothesis;
- Perform assays of formal potential ($E^{o'}$) dependence with temperature, to verify the conformational and/or structural changes on the enzyme and in its [4Fe-4S] cluster, in the absence and presence of DNA;
- Optimize the conditions for using a gold electrode modified with thiolated-DNA, in order to use the Electrochemical Quartz Crystal Microbalance (EQCM) technique to study the protein-DNA complex stability;
- Use surface analysis techniques, such as Atomic Force Microscopy (AFM), to verify the presence of unbounded Endo III or protein-DNA complex and its orientation at the electrode surface;
- Use complementary spectroscopic techniques such as EPR, Fluorescence and Mössbauer to assess chemical modification of the primary structure of Endo III and the integrity and redox state of its [4Fe-4S] cluster, after exposure to radiation;
- Expose Endo III to other sources of radiation, for instance, γ-radiation and evaluate its effects.

References

[1] T. Lindahl, “Instability and decay of the primary structure of DNA”, *Nature*, vol. 362, no. 6422, (1993), pp. 709–715.

[2] O. D. Schärer, “Chemistry and biology of DNA repair”, *Angewandte Chemie (International ed. in English)*, vol. 42, no. 26, (2003), pp. 2946–2974.

[3] J. H. J. Hoeijmakers, “DNA damage, aging, and cancer”, *The New England Journal of Medicine*, vol. 361, no. 15, (2009), pp. 1475–1485.

[4] J. H. J. Hoeijmakers, “Genome maintenance mechanisms for preventing cancer”, *Nature*, vol. 411, no. 6835, (2001), pp. 366–374.

[5] J. L. Huffman, O. Sundheim & J. A. Tainer, “DNA base damage recognition and removal: new twists and grooves”, *Mutation research*, vol. 577, (2005), pp. 55–76.

[6] T. Lindahl & R. D. Wood, “Quality Control by DNA Repair”, *Science*, vol. 286, (1999), pp. 1897–1905.

[7] H. E. Krokan, R. Standal & G. Slupphaug, “DNA glycosylases in the base excision repair of DNA”, *The Biochemical Journal*, vol. 325, (1997), pp. 1–16.

[8] A. B. Robertson, A. Klungland, T. Rognes & I. Leiros, “DNA repair in mammalian cells: Base excision repair: the long and short of it”, *Cellular and Molecular Life Sciences*, vol. 66, (2009), pp. 981–993.

[9] O. D. Schärer & J. Jiricny, “Recent progress in the biology, chemistry and structural biology of DNA glycosylases”, *BioEssays*, vol. 23, no. 3, (2001), pp. 270–281.

[10] K. Hitomi, S. Iwai & J. A. Tainer, “The intricate structural chemistry of base excision repair machinery: implications for DNA damage recognition, removal, and repair”, *DNA repair*, vol. 6, (2007), pp. 410–428.

[11] S. S. Parikh, C. D. Mol, G. Slupphaug, S. Bharati, H. E. Krokan& J. A. Tainer, “Base excision repair initiation revealed by crystal structures and binding kinetics of human uracil-DNA glycosylase with DNA”, *The EMBO Journal*, vol. 17, no. 17, (1998), pp. 5214–5226.

[12] S. S. Parikh, C. D. Mol & J. A. Tainer, “Base excision repair enzyme family portrait: integrating the structure and chemistry of an entire DNA repair pathway”, *Structure*, vol. 5, no. 12, (1997), pp. 1543–1550.

[13] J. C. Fromme, A. Banerjee & G. L. Verdine, “DNA glycosylase recognition and catalysis”, *Current Opinion in Structural Biology*, vol. 14, (2004), pp. 43–49.

[14] A. Klungland & T. Lindahl, “Second pathway for completion of human DNA base excision-repair: reconstitution with purified proteins and requirement for DNase IV (FEN1)”, *The European Molecular Biology Organization Journal*, vol. 16, no. 11, (1997), pp. 3341–3348.

[15] A. Memisoglu & L. Samson, “Base excision repair in yeast and mammals”, *Mutation research*, vol. 451, (2000), pp. 39–51.

[16] J. C. Fromme & G. L. Verdine, “Structure of a trapped endonuclease III-DNA covalent intermediate”, *The EMBO Journal*, vol. 22, no. 13, (2003), pp. 3461–3471.

[17] D. O. Zharkov, “Structure and conformational dynamics of base excision repair DNA glycosylases”, *Molecular Biology*, vol. 41, no. 5, (2007), pp. 702–716.

[18] C. F. Kuo, D. E. McRee, C. L. Fisher, S. F. O’Handley, R. P. Cunningham & J. A. Tainer, “Atomic structure of the DNA repair [4Fe-4S] enzyme endonuclease III”, *Science*, vol. 258, (1992), pp. 434–440.

[19] M. M. Thayer, H. Ahern, D. Xing, R. P. Cunningham & J. A. Tainer, “Novel DNA binding motifs in the DNA repair enzyme endonuclease III crystal structure”, *The EMBO Journal*, vol. 14, no. 16, (1995), pp. 4108–4120.

[20] R. P. Cunningham, H. Asahara, J. F. Bank, C. P. Scholes, J. C. Salerno, K. Surerus, E. Münck, J. McCracken, J. Peisach & M. H. Emptage, “Endonuclease III Is an Iron-Sulfur Protein”, *Biochemistry*, vol. 28, (1989), pp. 4450–4455.

[21] C. F. Kuo, D. E. McRee, R. P. Cunningham & J. A. Tainer, “Crystallization and crystallographic characterization of the iron-sulfur-containing DNA-repair enzyme endonuclease III from Escherichia coli”, *Journal of Molecular Biology*, vol. 227, (1992), pp. 347–351.

[22] W. Fu, S. O’Handley, R. P. Cunningham & M. K. Johnson, “The Role of the Iron-Sulfur Cluster in Escherichia coli Endonuclease III”, *Journal of Biological Chemistry*, vol. 267, no. 23, (1992), pp. 16135–16137.

[23] S. L. Porello, M. J. Cannon & S. S. David, “A Substrate Recognition Role for the [4Fe-4S]2+ Cluster of the DNA Repair Glycosylase MutY”, *Biochemistry*, vol. 37, no. 18, (1998), pp.6465–6475.

[24] M. Kearse, R. Moir, A. Wilson, S. Stones-Havas, M. Cheung, S. Sturrock, S. Buxton, A. Cooper, S. Markowitz, C. Duran, T. Thierer, B. Ashton, P. Meintjes & A. Drummond, “Geneious Basic: An integrated and extendable desktop software platform for the organization and analysis of sequence data”, *Bioinformatics*, vol. 28, no. 12, (2012), pp. 1647–1649.

[25] M. Radman, “An endonuclease from Escherichia coli that introduces single polynucleotide chain scissions in ultraviolet-irradiated DNA”, Journal *of Biological Chemistry*, vol. 251, no. 5, (1976), pp. 1438–1445.

[26] H. E. Krokan, H. Nilsen, F. Skorpen, M. Otterlei & G. Slupphaug, “Base excision repair of DNA in mammalian cells”, *FEBS letters*, vol. 476, (2000), pp. 73–77.

[27] H. Asahara, P. M. Wistort, J. F. Bank, R. H. Bakerian & R. P. Cunningham, “Purification and Characterization of Escherichia coli Endonuclease III from the Cloned nth Gene”, *Biochemistry*, vol. 28, (1989), pp. 4444–4449.

[28] S. Bian & J. A. Cowan, “Protein-bound iron-sulfur centers. Form, function and assembly”,*Coordination Chemistry Reviews*, vol. 190–192, (1999), pp. 1049–1066.

[29] O. A. Lukianova & S. S. David, "A role for iron-sulfur clusters in DNA repair", *Current Opinion in Chemical Biology*, vol. 9, (2005), pp. 145–151.

[30] A. W. Bott, "Redox Properties of Electron Transfer Metalloproteins", *Current Separations*, vol. 18, no. 2, (1999), pp. 47–54.

[31] C. W. Carter, "X-ray analysis of high-potential iron-sulfur proteins and ferredoxins" in Iron-Sulfur Proteins, edited by W. Lovenberg, Academic Press, (1977), pp. 157–204.

[32] E. Yavin, E. D. A. Stemp, V. L. O'shea, S. S. David & J. K. Barton, "Electron trap for DNA-bound repair enzymes: a strategy for DNA-mediated signaling", *Proceedings of the National Academy of Sciences*, vol. 103, no. 10, (2006), pp. 3610–3614.

[33] A. A. Gorodetsky, A. K. Boal & J. K. Barton, "Direct electrochemistry of Endonuclease III in the presence and absence of DNA", *Journal of the American Chemical Society*, vol. 128, no. 37, (2006), pp. 12082–12083.

[34] A. K. Boal, E. Yavin, O. A. Lukianova, V. L. O'Shea, S. S. David & J. K. Barton, "DNA-bound redox activity of DNA repair glycosylases containing [4Fe-4S] clusters", *Biochemistry*, vol. 44, no. 23, (2005), pp. 8397–8407.

[35] A. K. Boal, E. Yavin & J. K. Barton, "DNA repair glycosylases with a [4Fe-4S] cluster: a redox cofactor for DNA-mediated charge transport?", *Journal of Inorganic Biochemistry*, vol. 101, (2007), pp. 1913–1921.

[36] E. M. Boon, A. L. Livingston, N. H. Chmiel, S. S. David & J. K. Barton, "DNA-mediated charge transport for DNA repair", *Proceedings of the National Academy of Sciences*, vol. 100, no. 22, (2003), pp. 12543–12547.

[37] J. C. Genereux, A. K. Boal & J. K. Barton, "DNA-mediated charge transport in redox sensing and signaling", *Journal of the American Chemical Society*, vol. 132, no. 3, (2010), pp. 891–905.

[38] P. A. Sontz, T. P. Mui, J. O. Fuss, J. A. Tainer & J. K. Barton, "DNA charge transport as a first step in coordinating the detection of lesions by repair proteins", *Proceedings of the National Academy of Sciences*, vol. 109, no. 6, (2012), pp. 1856–1861.

[39] E. M. Boon & J. K. Barton, "Charge transport in DNA", *Current Opinion in Structural Biology*, vol. 12, (2002), pp. 320–329.

[40] C. A. Romano, P. A. Sontz & J. K. Barton, "Mutants of the Base Excision Repair Glycosylase, Endonuclease III: DNA Charge Transport as a First Step in Lesion Detection", *Biochemistry*, vol. 50, (2011), pp. 6133–6145.

[41] A. K. Boal, J. C. Genereux, P. A. Sontz, J. A. Gralnick, D. K. Newman & J. K. Barton, "Redox signaling between DNA repair proteins for efficient lesion detection", *Proceedings of the National Academy of Sciences*, vol. 106, no. 36, (2009), pp. 15237–15242.

[42] E. Yavin, A. K. Boal, E. D. A. Stemp, E. M. Boon, A. L. Livingston, V. L. O'Shea, S. S. David & J. K. Barton, "Protein-DNA charge transport: redox activation of a DNA repair protein by guanine radical", *Proceedings of the National Academy of Sciences*, vol. 102, no. 10, (2005), pp. 3546–3551.

[43] A. A. Gorodetsky, M. C. Buzzeo & J. K. Barton, "DNA-Mediated Electrochemistry", *Bioconjugate Chemistry*, vol. 19, no. 12, (2008), pp. 2285–2296.

[44] D. Penas, "Estudo do efeito da radiação em enzimas de reparação de DNA - A EndonucleaseIII", Graduation Project, FCT-UNL, Lisbon, 2009.

[45] E. Gasteiger, C. Hoogland, A. Gattiker, S. Duvaud, M. R. Wilkins, R. D. Appel & A. Bairoch, "Protein Identification and Analysis Tools on the ExPASy Server" in *The Proteomics Protocols Handbook*, J. M. Walker (ed.), Humana Press Inc., Totowa, NJ, 2005, pp. 571-607.

[46] T. P. Hilbert, W. Chaung, R. J. Boorstein, R. P. Cunningham & G. W. Teebor, "Cloning and expression of the cDNA encoding the human homologue of the DNA repair enzyme, Escherichia coli endonuclease III", *Journal of Biological Chemistry*, vol. 272, no. 10, (1997), pp. 6733–6740.

[47] S. Ikeda, T. Biswas, R. Roy, T. Izumi, I. Boldogh, A. Kurosky, A. H. Sarker, S. Seki & S. Mitra, "Purification and Characterization of Human NTH1, a Homolog of Escherichia coli Endonuclease III", *Journal of Biological Chemistry*, vol. 273, no. 34, (1998), pp. 21585–21593.

[48] O. H. Lowry, N. J. Rosebrough, A. L. Farr & R. J. Randall, "Protein measurements with the Folin phenol reagent", *Journal of Biological Chemistry*, vol. 193, (1951), pp. 265–275.

[49] F. Folgosa, C. M. Cordas, J. A. Santos, A. S. Pereira, J. J. G. Moura, P. Tavares & I. Moura, "New spectroscopic and electrochemical insights on a class I superoxide reductase: evidence for an intramolecular electron-transfer pathway", *The Biochemical Journal*, vol. 438, (2011), pp. 485–494.

[50] P. K. Smith, R. I. Krohn, G. T. Hermanson, A. K. Mallia, F. H. Gartner, M. D. Provenzano, E. K. Fujimoto, N. M. Goeke, B. J. Olson & D. C. Klenk, "Measurement of protein using bicinchoninic acid", *Analytical Biochemistry*, vol. 150, no. 1, (1985), pp. 76–85.

[51] "Bicinchoninic Acid (BCA) Protein Assay", G-Biosciences, 2010, available at: http://www.gbiosciences.com/634096940789210559.pdf. [Accessed: Sep 21, 2012].

[52] K. M. Maloney, E. M. Quiazon & R. Indralingam, "Measurement of Iron in Egg Yolk: An Instrumental Analysis Experiment Using Biochemical Principles", *Journal of Chemical Education*, vol. 85, no. 3, (2008), pp. 399–400.

[53] "Experiment 9 : Determination of Iron with 1,10-Phenanthroline", Department of Chemistry, University of Tennessee, available at: http://www.chem.utk.edu/~chem319/Experiments/exp10.pdf. [Accessed: Sep 26, 2011].

[54] P. Tavares, "Estudo de Novos Centros Contendo Ferro: Isolamento e Caracterização de Proteínas de Desulfovibrio desulfuricans AlCC 27774", Doctoral Thesis, FCT-UNL, Lisbon, 1994.

[55] Maria de Lurdes Sadler Simões Gonçalves, *Métodos instrumentais para análise de soluções: análise quantitativa*, Third Edition, Fundação Calouste Gulbenkian, Lisbon, 1996.

[56] J. Sambrook & D. W. Russell, *Molecular Cloning: A Laboratory Manual*, Third Edition, Cold Spring Harbor Laboratory Press, New York, 2001.

[57] C. D. S. Mota, "Desenvolvimento de um sistema para irradiação por ultravioleta de biomoléculas", Master Thesis, FCT-UNL, Lisbon, 2011.

[58] M. D. Abràmoff, P. J. Magalhães & S. J. Ram, "Image Processing with ImageJ", *Biophotonics International*, vol. 11, (2004), pp. 36–42.

[59] "Using ImageJ to Quantify Gel Images", Physics/Astronomy Network of Intel Computers (PANIC), 2009, available at: http://panic.berkeley.edu/~ghe/GelDoc/UsingImageJ/UsingImageJ.pdf. [Accessed: Jun 03, 2012].

[60] C. Giulivi & K. J. A. Davies, "Dityrosine and Tyrosine Oxidation Products Are Endogenous Markers for the Selective Proteolysis of Oxidatively Modified Red Blood Cell Hemoglobin by (the 19 S) Proteasome", *Journal of Biological Chemistry*, vol. 268, no. 12, (1993), pp. 8752–8759.

[61] M. Valko, C. J. Rhodes, J. Moncol, M. Izakovic & M. Mazur, "Free radicals, metals and antioxidants in oxidative stress-induced cancer", *Chemico-biological interactions*, vol. 160, (2006), pp. 1–40.

[62] L. M. Hellman & M. G. Fried, "Electrophoretic mobility shift assay (EMSA) for detecting protein-nucleic acid interactions", *Nature protocols*, vol. 2, no. 8, (2007), pp. 1849–1861.

[63] B. Dey, S. Thukral, S. Krishnan, M. Chakrobarty, S. Gupta, C. Manghani & V. Rani, "DNA-protein interactions: methods for detection and analysis", *Molecular and Cellular Biochemistry*, vol. 365, no. (1–2), (2012), pp. 279–299.

[64] C. G. Timóteo, M. Guilherme, D. Penas, F. Folgosa, P. Tavares & A. S. Pereira, "Desulfovibrio vulgaris bacterioferritin uses H2O2 as co-substrate for iron oxidation and reveals DPS-like DNA protection and binding activities", *Biochemical Journal*, vol. 446, no. 1, (2012), pp. 125 – 133.

[65] K. K. Swinger & P. A. Rice, "IHF and HU: flexible architects of bent DNA", *Current Opinion in Structural Biology*, vol. 14, no. 1, (2004), pp. 28–35.

[66] G. S. Wilson, "Bioelectrochemistry", in *Encyclopedia of Electrochemistry*, Wiley-VCH, Weinheim, 2002.

[67] C. M. A. Brett & A. M. O. Brett, *Principles, Methods and Applications*, Oxford University Press Inc., New York, 1993.

[68] A. J. Bard & L. R. Faulkner, *Electrochemical Methods: Fundamentals and Applications*, John Wiley & Sons, Inc., New York, 2001.

[69] E. Laviron, "General expression of the linear potential sweep voltammogram in the case of diffusionless electrochemical systems", *Journal of Electroanalytical Chemistry*, vol. 101, (1979), pp. 19–28.

[70] R. G. Ehl & A. J. Ihde, "Faraday's electrochemical laws and the determination of equivalent weights", *Journal of Chemical Education*, vol. 31, no. 5, (1954), p. 226.

[71] E. R. Cohen, T. Cvitas, J. G. Frey, B. Holstrom & J. W. Jost (Eds.), *Quantities, Units and Symbols in Physical Chemistry*, Third Edition, Royal Society of Chemistry, Cambridge, 2007.

[72] N. Sato & H. Okuma, "Development of single-wall carbon nanotubes modified screen-printed electrode using a ferrocene-modified cationic surfactant for amperometric glucose biosensor applications", *Sensors and Actuators B*, vol. 129, (2008), pp. 188–194.

[73] J. Wang, *Analytical Electrochemistry*, Wiley-VCH, New York, 1994.

APPENDICES

Appendix A - Instrumentation

A.1 Sterilization

Sterilization of media and current laboratory materials was performed in an autoclave "Labo Autoclave" (*Sanyo*).

A.2 Buffer filtration

Filtration of buffers was carried out with a 0.45 µm pore filter (Cellulose Acetate, *GVS*) and a 47 mm Magnetic Filter Funnel (*Pall*).

A.3 Camera and transilluminators

To photograph gels, a "Gel Logic 100, Imaging System" camera (*Kodak)*, a White Light Transilluminator (*Uvitec*) and a "Safe Imager ^{TM} 2.0 Blue-Light" UV Transilluminator (*Invitrogen*) were used.

A.4 Cell disruption

E. coli cells were desintegrated through 3 cycles with an ultrasonic probe LABSONIC® M (*Sartorius*). Each cycle consisted of 3 min at 104 $W.cm^{-2}$ and 1 min 30 s at rest, always on ice.

A.5 Centrifugation

Harvesting of overexpressing cells after cell growth induction: centrifuge "Sigma 3-18K" (Sartorius) with a *Swinging Bucket 11180* rotor.

Low-speed centrifugations: microcentrifuge "Sigma 1-14" (*Sartorius*).

Ultracentrifugation: ultracentrifuge "Optima LE-80K" (*Beckman Coulter*), using the "Type 70 Ti" fixed-angle rotor for lower volumes (1 h 30 min at 118 000 *g* and 4 ^{o}C) and the "Type 45 Ti" fixed-angle rotor for higher volumes (1 h 30 min at 125 000 *g* and 4 ^{o}C).

A.6 Dialysis

Dialyses were performed in 12-14 kDa MWCO dialysis membranes (*Visking, Medicell International Ltd*).

A.7 Concentration through ultrafiltration

Vivaspin 2, 3 kDa MWCO (*GE Healthcare*).

A.8 Electrophoresis

For polyacrylamide gel electrophoresis, a *Biorad* system was used (including *Mini Protean® Tetra System* tray and accompanying material). "NuPAGE® Novex® Bis-Tris Mini Gels" electrophoresis were performed in a "XCell *SureLock*™ Mini-Cell" (*Invitrogen*). For agarose gel electrophoresis, a "Horizon® 11-14" (*Life Techonologies™*) tray was used. For all electrophoresis, an "Electrophoresis Power Supply - 301" (*GE*) voltage source was used.

A.9 Flame filtration

Syringes (*Braun*) and filters (32 mm Syringe filter with 0.8/0.2 μm *Supor*® Membrane, *Acrodisc, Pall*).

A.10 Material used in Ionic Exchange Chromatography for protein purification

Endo III was purified by Ionic Exchange Chromatography using a Resource S column (6 mL, *GE Healthcare)* pre-packed with Source 15 S resin (*GE Healthcare*).

The column was coupled to an "ÄKTA™ prime plus" system. For column refrigeration, the column was placed on ice.

A.11 pH Electrode

"pH Meter, Basic 20" (*Crison*).

A.12 Potentiostats and data acquisition software used in electrochemical assays

Potenciostat "μAutolab Type III" (*Autolab*) and potenciostat/galvanostat "Autolab 128N" (*Autolab*). The data acquisition software used was GPES (version 4.9, *Eco Chemie*).

A.13 Simultaneous Stirring and Incubation

Orbital incubator "Ovan" (*Alfagene*).

A.14 Spectrophotometer

"Evolution 300, UV-Vis" (*Thermo Scientific*).

Precision cells made of Quartz SUPRASIL® (*Hellma*).

A.15 Weighting

Two digital scales were used: "Acculab" (*Sartorius)* and "CP224S" (*Sartorius*).

Appendix B - Protocols

B.1 Preparation of *E. coli* C43 (DE3) competent cells

The preparation protocol used for this purpose was based on a Sambrook's protocol [1].

1. A 5 mL test tube filled with sterile LB medium was inoculated with C43 (DE3) cells taken from a stock stored at -80 ^{o}C.
2. Cells were incubated overnight (14 to 16 hours) at 37 ^{o}C, 220 rpm.
3. 1 mL of this pre-culture was added to 100 mL LB medium and allowed to growth at 37 ^{o}C, 220 rpm until an O.D. near 0.4 at 600 nm.
4. Cell culture was transferred to 50 mL sterile Falcons tubes and left to cool down for 10 min on ice.
5. Cell culture was centrifuged at 3900 *g* for 10 min at 4 ^{o}C and supernatant discarded. The bottles were placed on ice immediately and each pellet was resuspended in 10 mL of 100 mM $MgCl_2$ (*Sigma*), with a continuous swirling in ice water for about 5 min until fully resuspended.
6. Resuspended pellets were combined into one centrifuge bottle and 30 mL of $MgCl_2$ were added.
7. Resuspended pellet was centrifuged at 3900 *g* for 10 min at 4 ^{o}C and supernatant discarded. The bottle was placed on ice immediately and the resulting pellet was resuspended in 20 mL of 100 mM $CaCl_2$ (*Scharlau*), by swirling in ice water until fully resuspended.
8. 30 mL of $CaCl_2$ were added and the resuspended pellet was centrifuged at 3900 *g* for 10 min at 4 ^{o}C.
9. Supernatant was discarded, 5.4 mL of $CaCl_2$ were added to the resulting pellet and it was resuspend by swirling it in ice water.
10. 0.9 mL of 100 % Glycerol (*Sigma*) previously chilled were added. Cells were placed on ice quickly and mixed gently every 5 min for 30 min, until fully homogenized.
11. 200 μL of cells were aliquoted into chilled eppendorf tubes with chilled pipet tips. Aliquots were stored at -80°C.

B.2 Transformation of competent cells

B.2.1 *E. coli* C43 (DE3) competent cells transformation

The transformation protocol used for this purpose was based on *Lucigen Corporation* protocol [2].

1. *E. coli* C43 (DE3) competent cells were thawed on ice.
2. 5 µL of miniprep DNA sample (pET21c – EndoIII) were added to 50 µL of competent cells. For the positive control, 1 µL of pUC19 control DNA (*NZYTech*) were added to one eppendorf containing 50 µL of competent cells and for negative control, the volume that was left on the eppendorf containing the competent cells was used. Cells were gently mixed, without pipetting.
3. Reactions were incubated on ice for 30 min.
4. Each transformation was heat-shocked by placing them in a 42 ^{o}C water bath for 45 seconds.
5. Each transformation was placed on ice for 2 min.
6. 950 µL of room temperature LB medium were added to the cells in the culture tube.
7. Tubes were placed in a shaking incubator at 225 rpm for 1 hour and 15 min at 37 ^{o}C.
8. Using a sterile spreader, 50 and 200 µL of transformed cells were spreaded on LB/Agar plates supplemented with 0.1 mg/mL ampicillin. For positive and negative control only one volume was plated (e.g. 200 µL).
9. Plates were incubated overnight at 37 ^{o}C.

B.2.2 NZY5α competent cells transformation

The transformation protocol used for this purpose was based on *NZYTech* protocol [3].

1. Competent cells were thawed on ice and gently mixed.
2. To determine the transformation efficiency, 1 µL of pUC19 control DNA was added to 50 µL of competent cells.
3. For DNA from ligation reactions, 5 µL of the reaction were added to 50 µL of competent cells.
4. For negative control, the volume left on the eppendorf containing the competent cells was used.
5. Reactions were incubated on ice for 30 min.
6. Cells were heat-shocked by placing them in a 42 ^{o}C water bath for 30 seconds.
7. Cells were placed on ice for 2 min.

8. 900 µL of room temperature LB medium were added to the cells.
9. Tubes were placed in a shaking incubator at 225 rpm for 1 hour and 15 min at 37 ^{o}C.
10. Using a sterile spreader, 50 and 200 µL of transformed cells were spreaded on LB/Agar plates supplemented with 0.1 mg/mL ampicillin. For positive and negative control only one volume was plated (e.g. 200 µL).
11. Plates were incubated overnight at 37 ^{o}C.

B.3 Plasmid DNA extraction and purification

B.3.1 E.Z.N.A. Plasmid Midi Kit (*Omega*) [4]

1. Bacterial cells were harvested by centrifuging 20-50 mL of overnight culture at 7 000 rpm for 10 min.
2. Medium was decanted and to ensure that all traces of the medium were removed, a clean paper towel was used to blot excess liquid from the wall of the vessel.
3. 2.25 mL of the Solution I/RNase A were added to the bacterial pellet. Cells were resuspended completely by pipetting up and down.
4. Cell suspension was transferred to a 50 mL centrifuge tube capable of withstanding 12 000 *g*. 2.25 mL of the Solution II were added. Cell suspension was mixed gently and thoroughly by inverting and rotating the tube 8-10 times until a cleared lysate was obtained. This required 2-3 min of incubation at room temperature with occasional mixing.
5. 3.2 mL of the Solution III were added. The solution was mixed gently and thoroughly by inverting and rotating the tube several times until a flocculent white precipitates was formed. This required 5 min of incubation at room temperature with occasional mixing.
6. Cells were centrifuged for 20 min at 8 000 rpm and 4°C.
7. 1 mL of Equilibration Buffer was added to a HiBind® DNA Midi column pre-inserted in a 15 mL collection tube. The column was left to sit for 4 min at room temperature to equilibrate the membrane.
8. Buffer was centrifuged at 3 000 *g* for 3 min and the flow-through discarded. The HiBind® DNA Midi column was reinserted in the same collection tube.
9. 3.5 mL of the cleared supernatant from step 6 were added to the DNA Midi column by carefully aspirating it into the column.
10. The cleared supernatant was centrifuge at 5 000 *g* for 5 min and the flow-through discarded. The DNA Midi column was reinserted in the same collection tube.
11. Steps 9-10 were repeated until all of the supernatant passed through the column.

12. 3 mL of Buffer HB were added to the Midi column and centrifuged as above. The flow-through was discarded and DNA Midi column was reinserted in the same collection tube.
13. 3.5 mL of DNA Wash Buffer (previously diluted with absolute ethanol) were added to the Midi column and centrifuged as above. The flow-through was discarded and DNA Midi column was reinserted in the same collection tube.
14. Another 3.5 mL of DNA Wash Buffer were added to the DNA Midi column and centrifuged as above. The flow-through was discarded and DNA Midi column was reinserted in the same collection tube.
15. The empty DNA Midi column was centrifuged at 7 000 rpm for 20 min to dry the column matrix.
16. The DNA Midi column was place into a new/clean 15 mL centrifuge tube. 1 mL of Elution Buffer (10 mM Tris, pH 8.5) was added onto the center of the column matrix and the column was left to sit at room temperature for 3 min.
17. The Elution Buffer was centrifuged at 8 000 *g* for 5 min to elute DNA. A second elution was performed by adding 0.5 mL of Elution Buffer onto the center of the column matrix. The column was left to sit at room temperature for 3 min and then centrifuged as mentioned above.

B.3.2 NZYMiniprep Kit *(NZYTech)* [5]

1. 1-5 mL of an *E. coli* LB culture was/were pelleted for 30 s at 14 000 *g*. The supernatant was discarded and the medium was removed as much as possible.
2. Cell pellet was resuspended in 250 µL Buffer A1 by vigorous vortexing.
3. 250 µL of Buffer A2 were added and mixed gently by inverting the tube for 6-8 times.
4. The mix was incubated at room temperature for 4 min.
5. 300 µL Buffer A3 were added and mixed gently by inverting the tube for 6-8 times.
6. The mix was centrifuged for 5-10 min at 14 000 *g* and room temperature.
7. A NZYTech spin column was placed in a 2 mL collecting tube and the supernatant from step 3 was loaded onto the column.
8. The supernatant was centrifuge for 1 min at 11 000 *g* and the flow-through discarded.
9. 500 µL of Buffer AY were added onto the column and centrifuged for 1 min at 14 000 *g*. Flow-through was discarded.
10. 600 µL of Buffer A4 (with ethanol previously added) were added and centrifuged for 1 min at 14 000 *g*. Flow-through was discarded.

11. The NZYTech spin column was re-insert into the empty 2 mL collecting tube and centrifuged for 2 min at 14 000 *g*.
12. The dried NZYTech spin column was placed into a clean 1.5 mL microcentrifuge tube and 50 µL of Buffer AE were added into the center part of the column.
13. Buffer AE was incubate for 1 min at room temperature and centrifuged for 1 min at 14 000 *g*. A second elution was performed with 30 µL of the elution buffer.
14. Purified DNA was store at -20 °C.

This protocol is preceded by NZY5α competent cells transformation protocol (*vide* Appendix B.2.2), both of which were performed in order to have a stock of plasmid pET21c(+) – Endo III.

Appendix C - Culture mediums

C.1 LB and LB/Agar media

LB is a nutritionally rich medium that is widely used in molecular microbiology applications for the preparation of plasmid DNA and recombinant proteins. It continues to be one of the most common media used for propagation and maintenance of recombinant strains of *Escherichia coli*.

In this project, both the LB and the LB/Agar media (*NZYTech*) were already prepared and ready to be used. Their formula is presented in Table C.1.

Table C. 1 | Composition for 1 L LB or LB/Agar culture media.

Reagent	Quantity per Liter
NaCl	10 g
Tryptone	10 g
Yeast extract	5 g
Agar[1]	10 g

[1] For LB/Agar medium

The culture media (25 g for LB and 35 g for LB/Agar) are dissolved in 1 L of distillated water and the solutions are autoclaved at 121 ^{o}C for 20 min. The solutions are left to cool to 50 ^{o}C or below before adding antibiotics or additional nutritional supplements. The LB/Agar medium is then distributed in sterile Petri dishes, turning solid when completely cooled.

C.2 2xYT medium

2xYT is a nutritionally rich medium for the growth of recombinant strains of *Escherichia coli*. This bacteria thrives in this medium because of the additional amino acids, nucleotide precursors, vitamins, and other essential metabolites that the cell need during growth and development. Sodium chloride is present in the Tryptone medium and provides a suitable osmotic environment for the growing, replicating bacteria [6].

Table C. 2 | Composition for 1 L 2xYT medium broth.

Reagent	Quantity per Liter
Tryptone medium (*Fluka*)	20 g
Yeast extract (*Cultimed*)	10 g

The reagents are dissolved in 1 L of distillated water and the solutions are autoclaved at 121 ^{o}C for 20 min. The solutions are left to cool to 50 ^{o}C or below before adding antibiotics or additional nutritional supplements.

C.3 M9 medium

✓ M9 Salts (10x)

Table C. 3 | Reagents used in the preparation of M9 Salts (10X) solution.

Reagent	Quantity per Liter
$Na_2HPO_4.7H_2O$ (*Sigma*)	128 g
KH_2PO_4 (*Panreac*)	30 g
NH_4Cl (*Sigma*)	10 g
NaCl (*Panreac*)	5 g

The reagents are dissolved in deionized water and before making up to the final volume of 1 L the pH of the solution is adjusted to 7.0 with NaOH 1M.

✓ Preparation of M9 Medium (sterilized at 120 ^{o}C for 20 min)

Table C. 4 | Composition of the medium to be sterilized.

Volume	100 mL	1 000 mL
Deionized water	88 mL	880 mL
M9 Salts (10x)	10 mL	100 mL

✓ M9 Medium

The following reagents must be prepared and sterilized separately, and added to the previous sterilized medium (M9 Salts (10x) plus deionized water) prior to its use.

Table C. 5 | Reagents used in the preparation of M9 Medium.

Reagent	Volume per Liter
$MgSO_4.7H_2O$ 1M (*Sigma*) [1]	1 mL
$CaCl_2.2H_2O$ 0.1M (*Scharlau*) [1]	1 mL
Glucose 20 % (*Sigma*) [1]	20 mL
Tiamine-HCl 0.1 % (*Sigma*) [2]	0.5 mL
Vitamins (200x) [3]	5 mL
$FeSO_4.7H_2O$ 0.1 M (*Sigma*) [2]	1 mL
Ampicillin 100 mg/mL [3]	1 mL

[1] Flame filtration
[2] Preparation prior to use, flame filtration and storage at 4 ^{o}C
[3] Flame filtration and storage at 4 ^{o}C or -20 ^{o}C, for longer periods of time

- Vitamins (200x)

Table C. 6 | Reagents used in the preparation of vitamins solution (200x).

Reagent	Quantity per Liter
Tiamine-HCl	1 g
Biotine (*Fluka*)	200 mg
Cloreto de colina (*Sigma*)	200 mg
Folic acid (*Sigma*)	200 mg
Nicotinic acid (*Sigma*)	200 mg
Pantothenic acid hemicalcium salt (*Sigma*)	200 mg
Piridoxal (*Sigma*)	200 mg
Riboflavine (*Sigma*)	20 mg

Appendix D - Resource S chromatographic column

Resource S column (6 mL) was equilibrated in 20 % ethanol and was properly treated before being use as follows:

1. 3 column volumes of Milli-Q water at a flow rate of 1 mL/min to remove ethanol, since it causes buffer ion precipitation;
2. Buffer A (100 mM Tris-HCl, pH 7.1) at 1 mL/min to equilibrated the column.

After use, the column is washed and stored, as follows:

1. Buffer A to lower the conductivity;
2. 3 column volumes of Milli-Q water at a flow rate of 6 mL/min;
3. 1 column volume of 20 % ethanol at a flow rate of 6 mL/min;
4. Store at 4 ^{o}C.

All the aforementioned steps were carried out according to manufacturer's instructions [7].

Note: Both Buffer A and ethanol 20 % were previously filtered through a 0.45 µm pore filter.

Appendix E - Gels

E.1 Polyacrylamide Gel Electrophoresis in denaturing conditions (SDS-PAGE)

The sodium dodecyl sulfate polyacrylamide gel electrophoresis (SDS-PAGE) is a technique widely used both in the determination of a protein's molecular mass as to assess the purity level of the protein fractions throughout the purification. It is based on the technique described by Laemmli [8] and in this thesis it was used mainly for purity assessment.

Gel polimerization was performed according to the *BioRad* protocol, using the solutions and volumes shown in Table E.1. The samples were prepared by adding sample buffer containing β-mercaptoethanol in a 1:1 ratio to the sample and boiling them for 5 min, being then immediately applied onto the gel. The gels ran for 1 h 30 min at variable voltage (80-120 V) in 1x Tris-Glycine buffer (*vide* Table E.2). 4-12 % gradient pre-cast "NuPAGE® Novex® Bis-Tris Mini Gels" (*Invitrogen*) were also used, which ran for 35 min at 200 V in 1x NuPAGE® SDS Running buffer (1:20 dilution of 20x NuPAGE® MES SDS Running buffer (*Invitrogen*) in deionized water). The samples were prepared in the exact same way as mentioned above.

SDS-PAGE gels were stained with Coomassie Brilliant Blue R-250 staining solution and unstained afterwards with a bleach solution, both described in Table E.2. After bleaching, the gels were photographed with Gel Logic 100, Imaging System (*Kodak*).

Table E. 1 | Volumes of each solution used for a 12.5 % of acrylamide SDS-PAGE.

Solution	Stacking gel (5 % of Acrylamide)	Running gel (12.5 % of Acrylamide)
I	-	0.75 mL
II	0.45 mL	-
III	0.3 mL	2.08 mL
10 % SDS (*NZYTech*)	0.018 mL	0.05 mL
dH_2O	0.94 mL	2.1 mL
10 % APS (*BioRad*)	13.5 μL	38 μL
TEMED (*NZYTech*)	2 μL	2.5 μL

Table E. 2 | Stock solutions used for SDS-PAGE.

Solution	Reagents	Amount	Obs.
Running gel buffer (I)	2.5 M Tris Base 37 % HCl H_2O	30.3 g until pH 8.8 up to 100 mL	pH 8.8-9.0
Stacking gel buffer (II)	0.5 M Tris Base 37 % HCl H_2O	6.06 g until pH 6.8 up to 100 mL	pH 6.6-6.8
Acrylamide/Bisacrylamide (III) (37.5:1)	Acrylamide Bisacrylamide H_2O	30 g 0.8 g up to 100 mL	Already prepared (*BioRad*)
10 % SDS	SDS H_2O	10 g up to 100 mL	-
10 % APS	Ammonium Persulfate H_2O	0.02 g 200 μL	Prepare prior to use
Tris-Glycine buffer	0.25 M Tris Base 1.92 M Glycine (*Sigma*) 0.1 % SDS H_2O	30.3 g 144.1 g 10 g up to 1 000 mL	pH 8.3 Dilute 1:10 prior to use
Sample buffer	Solution II 10 % SDS β-mercaptoethanol (*Sigma*) Glycerol (*Sigma*) Bromophenol Blue (*Riedel*) H_2O	5 mL 8 mL 1 mL 2 mL 4 mg up to 20 mL	Add 1:1 to the sample
Coomassie Brilliant Blue Staining	Coomassie Blue R-250 (*Sigma*) Glacial Acetic Acid (*Merck*) Methanol (*Carlo Erba*) H_2O	1 g 15 mL 90 mL up to 200 mL	-
Bleach solution	Glacial Acetic Acid Methanol H_2O	75 mL 450 mL up to 1 000 mL	-

The molecular weight markers used in SDS-PAGE electrophoresis were *NZYTech* Low Molecular Weight (LMW) Standard and *Invitrogen* SeeBlue® Pre-stained Standard. Their electrophoretic profiles are exemplified in Figure E.1.

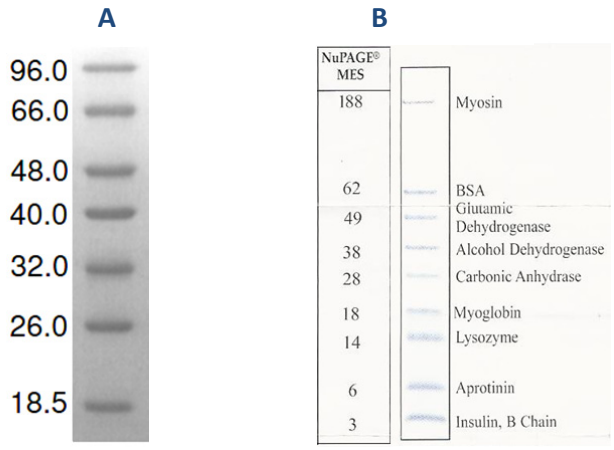

Figure E. 1 | A. NZYTech Low Molecular Weight (LMW) Standard. The gel was loaded with 5 μL of LMW marker on a pre-cast 14 % SDS-PAGE gel and stained with Coomassie Brilliant Blue. The molecular weight (kDa) of each standard is indicated on the left side of the figure; **B**. *Invitrogen* SeeBlue® Pre-stained Standard. The gel was loaded with 5 μL of this marker on a 10-20 % Tricine Gel and stained with Coomassie Brilliant Blue. The molecular weight (kDa) of each standard is indicated on the left side of the figure.

E.2 Agarose gel electrophoresis

Agarose gel electrophoresis is a technique widely used both in the determination of a DNA fragment's molecular weight as to assess the purity level of these fragments.

This type of electrophoresis allows the separation of nucleic acids fragments by their size. These, when subjected to electromotive force, migrate from a negative pole to a positive pole, since they have overall negative charge due to their phosphate groups. The larger the fragment, the slower will be its migration, thus smaller fragments migrate faster in the gel.

Gel polymerization was performed according to the manufacturer's instructions, varying between 0.8 % and 1 % (p/v). Samples were prepared by adding BlueJuice™ Gel Loading Buffer (*Invitrogen*) in a 1:1 ratio. The gels ran for 1 h 30 min - 1 h 45 min at 80 V in 1x TAE (v/v) buffer (40 mM Tris-acetate (*Panreac/Sigma*) pH 8.0, 1 mM EDTA (*Sigma*)). They were stained with SYBR® Safe (*Invitrogen*) staining solution, which has the ability to intercalate between the DNA bases in the same way as ethidium bromide. The major difference is that SYBR® Safe, like the name indicates, is safer to the user, while ethidium bromide is carcinogenic. After staining, the gels were imaged with Safe Imager ™ (*Invitrogen*) in a Gel Logic 100, Imaging System (*Kodak*).

The molecular weight marker used in agarose gel electrophoresis was NZYDNA Ladder III Standard (*NZYTech*), which is a ready-to-use marker especially designed for easy quantification and size determination. Its electrophoretic profile is shown in Figure E.2.

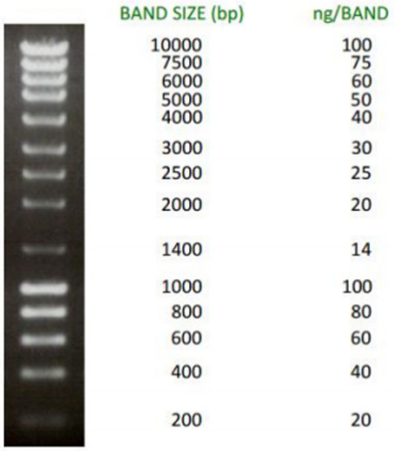

Figure E. 2 | NZYDNA Ladder III (*NZYTech*) Standard. The gel was loaded with 5 μL of NZYDNA Ladder III and run in a 1 % (p/v) agarose gel. The gel was buffered with 1x TAE (v/v) buffer and stained with Ethidium Bromide. The molecular weight (bp) and precise quantity of DNA (ng) of each standard is indicated on the right side of the figure.

Appendix F - Protein and iron quantifications

F.1 Protein quantification

F.1.1 Lowry's method

Protocol:

1. Prepare 11 protein standards (0 to 50 µg) and 2 protein samples with different concentrations into a final volume of 0.1 mL (dilutions made with Milli-Q water).
2. Add to each standard and sample 1 mL of solution C and incubate for 10 min.
3. Add 0.1 mL of solution D, mix and incubate for 30 min.
4. Measure the absorbance at 580, 680 and 750 nm.

The solutions used in this method are described in Table F.1.

Table F. 1 | Solutions used for Lowry's method [9].

Solution	Description	Preparation details
A	2 % Na_2CO_3 (*Merck*) in 0.1 N NaOH (*Eka*)	2 g Na_2CO_3 + 0.4 g NaOH in 100 mL of H_2O
B1	1 % $CuSO_4.5H_2O$ (*AnalaR, BHD Chemicals*)	1 g $CuSO_4.5H_2O$ in 100 mL of H_2O
B2	2 % Sodium tartarate (*Sigma*)	2 g Sodium tartarate in 100 mL of H_2O
B	1:1 mixture of B1 and B2	- (prepared prior to use)
C	Alkaline copper solution	50 mL of A + 1 mL of B (prepared prior to use)
D	Folin reagent 1:1 diluted (*Sigma*)	- (prepared prior to use)

F.1.2 BCA method

This method relies on two reactions. Firstly, the peptide bonds in the protein sample reduce Cu^{2+} ions from the alkaline copper solution to Cu^{+}. The amount of Cu^{2+} reduced is proportional to the amount of protein present in the solution. Next, two molecules of BCA chelate with each Cu^{+} ion, forming a water-soluble purple-colored complex that strongly absorbs light at a wavelength of 562 nm. Thus, the amount of protein present in a solution can be quantified by measuring the absorption spectra and comparing with protein solutions with known concentrations [10, 11].

The most likely explanation for the quantification by this method has failed relates to the fact that Endo III contains a [4Fe-4S] cluster. Iron, even at very low concentrations, interferes in the quantification because it is also capable of reducing Cu^{2+} to Cu^{+} [11], leading to a higher quantity of Cu^{+} ions. Thus, the amount of reduced Cu^{2+} is no longer proportional to the amount of protein present in the solution, leading to a wrong, higher value of protein concentration.

F.2 Iron content determination using Phenanthroline method

As mentioned in Subchapter 4.2, the Phenanthroline method requires extraction of iron from the protein polypeptide chain. Therefore, the samples (30 nmol Fe) with volumes of 500 and 600 µL were reduced with 60 µL of 10 % L(+)-Ascorbic acid sodium salt (*Fluka*). Then, the samples were incubated for 10 min with 75 µL of 8 N HCl (*Sigma*) in order to lower the pH of the solution to prevent iron oxides formation. After this, 75 µL of 80 % Trichloroacetic acid (*Alfa Aesar*) were added to precipitate the proteic content of the sample and leave the iron in solution. After 10 min, a centrifugation (5 min at 4 722 *g*) was carried out and the supernatant was transferred to a new tube [12].

The calibration curve was obtained with a standard iron solution (0.01 mg/mL) following a protocol adapted from [13]. The standard iron solution was prepared with Milli-Q water at pH 2 to prevent the formation of iron oxides.

The solutions used in this method are described in Table F.2.

Table F. 2 | Reagents and volumes (in mL) used for the calibration curve.

Reagent	Test tube					
	0	**1**	**2**	**3**	**4**	**5**
Standard iron solution (*Fluka*)	0	0.2	0.4	0.8	1.2	1.6
Milli-Q water	2.5	2.3	2.1	1.7	1.3	0.9
	Mix (vortex)					
10 % Hydroxylamine (*Sigma*)	0.4	0.4	0.4	0.4	0.4	0.4
	Mix (vortex)					
0.3 % Phenanthroline (*Panreac*)	0.4	0.4	0.4	0.4	0.4	0.4
	Mix (vortex) and wait 10 min					
Milli-Q water	1.7	1.7	1.7	1.7	1.7	1.7
	Measure Abs at 510 nm					

Vf = 5 mL

The exact same method was applied to the iron samples, with the exception of the sample volumes, which were 0.5 and 0.6 mL.

Appendix G - pUC18 digestion

pUC18 plasmid was hydrolyzed with *Eco*R I. This restriction enzyme was chosen by analysis of pUC18 plasmid vector map (Figure G.1).

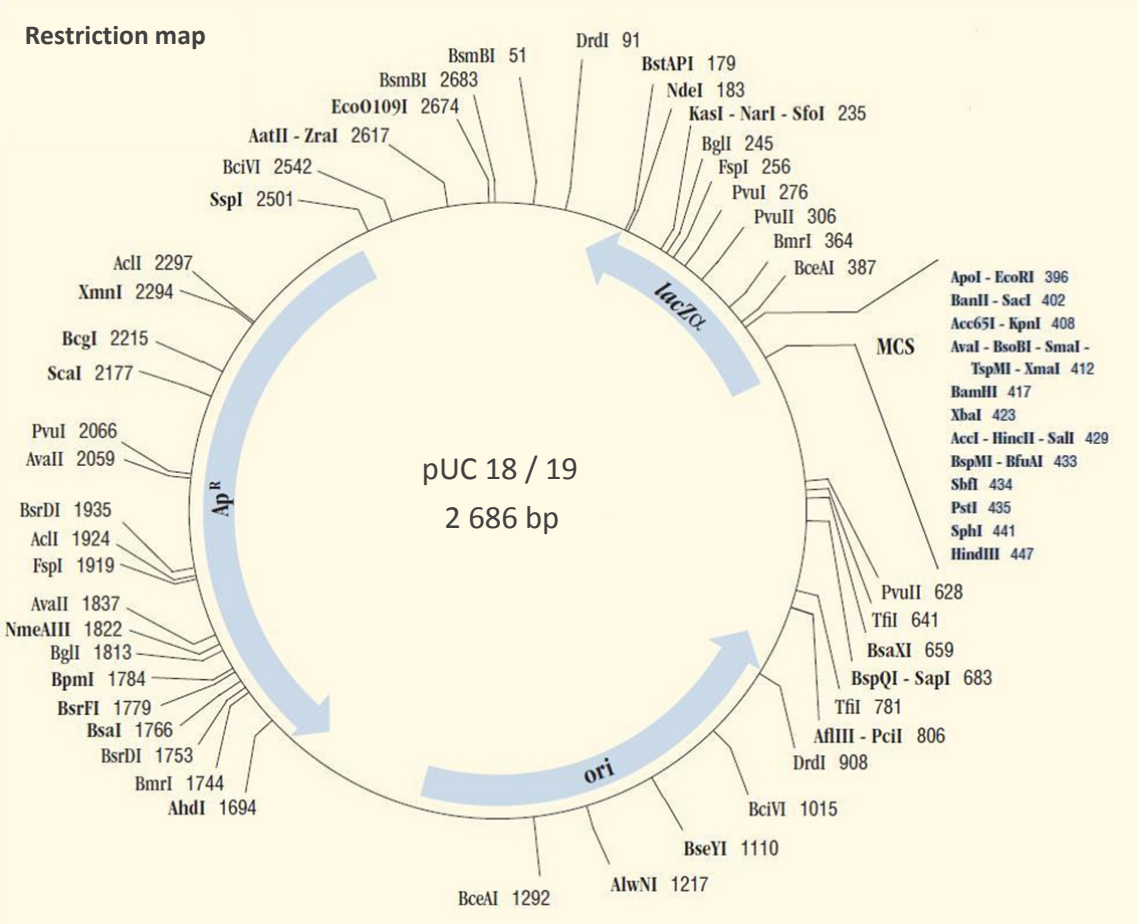

Figure G. 1 | pUC18 cloning vector map. Adapted from [14].

The preparation protocol used for this purpose was based on Takara's protocol [15] (Table G.1).

Table G. 1 | Composition of the reaction mixture for pUC18 hydrolysis.

Reagent	Volume
pUC18	35 µL
*Eco*R I (*Takara*)	2 µL
10x H Buffer (*Takara*)	4 µL

Appendix H - Experimental details of the irradiation assays

H.1 Irradiation of linear and supercoiled pUC18

For each of these assays, a bulk solution of 700 µl (7 samples x 100 µL) was prepared, consisting of 665 µL of 100 mM Tris-HCl, pH 7.1 plus 35 µL of pUC18, either linear (7 samples x 5 µL, hence the 35 µL of hydrolyzed pDNA) or in its supercoiled form.

The linear pUC18 final concentration was determined to be 3.41 ng/µL, i.e., 1.92 nM.

$[pUC18]_i$ = 80 ng/µL

$Volume_{pUC18}$ = 35 µL

$Volume_{hydrolysis}$ = 41 µL

$Volume_{sample}$ = 5 µL

$$80\ ng\mu L^{-1}\ x\ 35\ \mu L = cf\ x\ 41\ \mu L\ \Leftrightarrow\ cf = 68.29\ ng\mu L^{-1}$$

$$68.29\ ng\mu L^{-1}\ x\ 5\ \mu L = cf\ x\ 100\ \mu L\ \Leftrightarrow\ cf = 3.41\ ng\mu L^{-1} = 3.41e^{-3}\ gL^{-1}$$

$MW_{dsDNA\ bp}$ = 660 Da

MW_{pUC18} = 2 686 bp x 660 Da = 1772760 Da

$$\frac{3.41e^{-3}\ gL^{-1}\ x\ 1e^{9}}{1772760\ gmol^{-1}} = 1.92\ nM$$

The same concentration was used for the assay with supercoiled pUC18.

As stated in page 42 (Subchapter 5.3), to further explore the effects of UV radiation on supercoiled pDNA, a series of samples was prepared to increase the number of experimental points in the irradiation time course. For that, a bulk solution of 1100 µL (11 samples x 100 µL) was prepared, consisting of 1045 µL of 100 mM Tris-HCl, pH 7.1 plus 55 µL of supercoiled pUC18 (11 samples x 5 µL).

H.2 Endonuclease III exposure to UV radiation

For this assay, a bulk solution of 4400 µL (11 samples x 400 µL) was prepared, consisting of 3300 µL of 100 mM Tris-HCl, pH 7.1 plus 1100 µL of Endo III (36.94 µM).

H.3 EMSAs with irradiated Endonuclease III

Endo III samples were irradiated in pairs for two different periods of time. Thus, before each irradiation assay, two bulk solutions of 800 µl (2 samples x 400 µl) were prepared, one with an Endo III final concentration of 6.18 µM and the other with 15 µM. These dilutions were necessary for Endo III/pDNA molar ratios.

Appendix I - Electrochemical assays with recombinant Endonuclease III

Table I. 1 | Summary table of all the assays done until the Endo III electrochemical signal was obtained.

Date	Assay	[Endo III] (μM)	WE				RE		Supporting electrolyte			Method	
			Glassy Carbon	Graphite	Gold	Pyrolytic Graphite	SCE	Ag/AgCl	0.1 M Tris-HCl, pH 7.1 + 0.1 M KNO_3	0.1 M Tris-HCl, pH 7.1 + 0.1 M NaCl	0.1 M KPi, pH 7.1 + 0.1 M NaCl	Physical Adsorption	Cellulose Membrane
22.Sep.11	Endo III	36.94	■				■		20 mL			5 μL	
23.Sep.11	Endo III	36.94	■				■		20 mL			2x 5 μL	
27.Sep.11	Endo III	36.94		■			■		20 mL			8 μL	
27.Sep.11	Endo III	36.94		■			■		20 mL				10 μL
28.Sep.11	Endo III	36.94		■			■		20 mL				15 μL
29.Sep.11	Endo III	123.13		■			■		20 mL				15 μL
04.Oct.11	Endo III	114.12	■				■		20 mL				15 μL
07.Oct.11	Endo III	114.12	■				■		20 mL			2x 5 μL	5 μL
07.Oct.11	Endo III	114.12		■			■		20 mL			10 μL	
11.Oct.11	Endo III + BSA	114.12	■				■		20 mL			10 μL (mix)	
12.Oct.11	Endo III + BSA	114.12		■			■			20 mL		10 μL (mix)	
12.Oct.11	Endo III + BSA	114.12	■				■			20 mL		10 μL (mix)	
12.Oct.11	Endo III + BSA	114.12			■		■			20 mL		10 μL (mix)	
14.Oct.11	Endo III in modif. WE w/ 0.1 M 1-Propanthiol	114.12			■		■			20 mL		5 μL	
18.Oct.11	Endo III in solution	36.94	■	■	■	■		■	2 mL (Endo III + 0.1 M NaCl)				
21.Oct.11	Endo III + magnesium ion (Mg^{2+})	36.94	■	■	■	■	■		2 mL (Endo III + 0.1 M NaCl + 0.2 M $MgCl_2$)				
02.Nov.11	Endo III	314.71	■	■	■	■	■	■			4 mL	5 μL	
02.Nov.11	Endo III + Neom 2 mM	314.71	■	■	■	■	■	■			4 mL	2 μL N + 5 μL E	
03.Nov.11	Endo III + Neom 2 mM	314.71	■	■	■	■	■	■			4 mL		2 μL N + 5 μL E
07.Nov.11	Endo III + Neom 2 mM	314.71	■	■	■	■	■	■			4 mL		2 μL N + 5 μL E
17.Nov.11	Endo III	314.71				■		■			4 mL	5 μL	
18.Nov.11	Endo III	314.71				■		■			4 mL	5 μL	
06.Dec.11	Endo III + Neom 2 mM	314.71				■		■			4 mL	3 μL N + 5 μL E	
12.Dec.11	Endo III + Neom 2 mM	314.71				■		■			4 mL	3 μL N + 5 μL E + 5 μL E	
13.Dec.11	Endo III + Neom 2 mM	125.88				■		■			4 mL	3 μL N + 2 μL E + 3 μL B	
13.Dec.11	Endo III + Neom 2 mM	62.94				■		■			4 mL	3 μL N + 1 μL E + 4 μL B	

Abbreviations: WE, working electrode; RE, reference electrode; SCE, saturated calomel electrode; BSA, bovine serum albumin; Neom or N, neomycin; E, Endo III; B, buffer.

Bovine Serum Albumin (BSA) is a high molecular mass protein that, precisely for this reason, is used for the WE surface modification, i.e., it fills the empty spaces and creates a layer on the electrode surface in order to minimize the contribution of the oxides/hydroxides that are formed in solution with the carbon electrode surface.

Magnesium ion (Mg^{2+}) was used in order to increase the number of positive charges that would promote electrostatic interactions with the WE surface.

Neomycin is a promoter with positive charges, which promotes enzyme immobilization through electrostatic interactions with its negative residues.

In Figure I.1 are represented some of the methods and conditions used in the electrochemical assays mentioned in Table I.1.

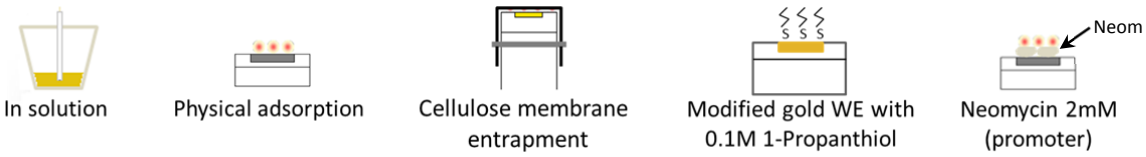

Figure I. 1 | Schematic representation of methods and conditions used in the electrochemical assays.

Appendix J - Electrochemical characterization of electrode surface

During the project, it was necessary to rebuild the working electrode more than once, in order to clean and smooth its surface, leading to a higher electrochemical performance and improvement in its conductivity.

Before its use, the working electrode was properly tested. For this test, an extremely well defined redox pair was chosen for maximum precision (Figure J.1).

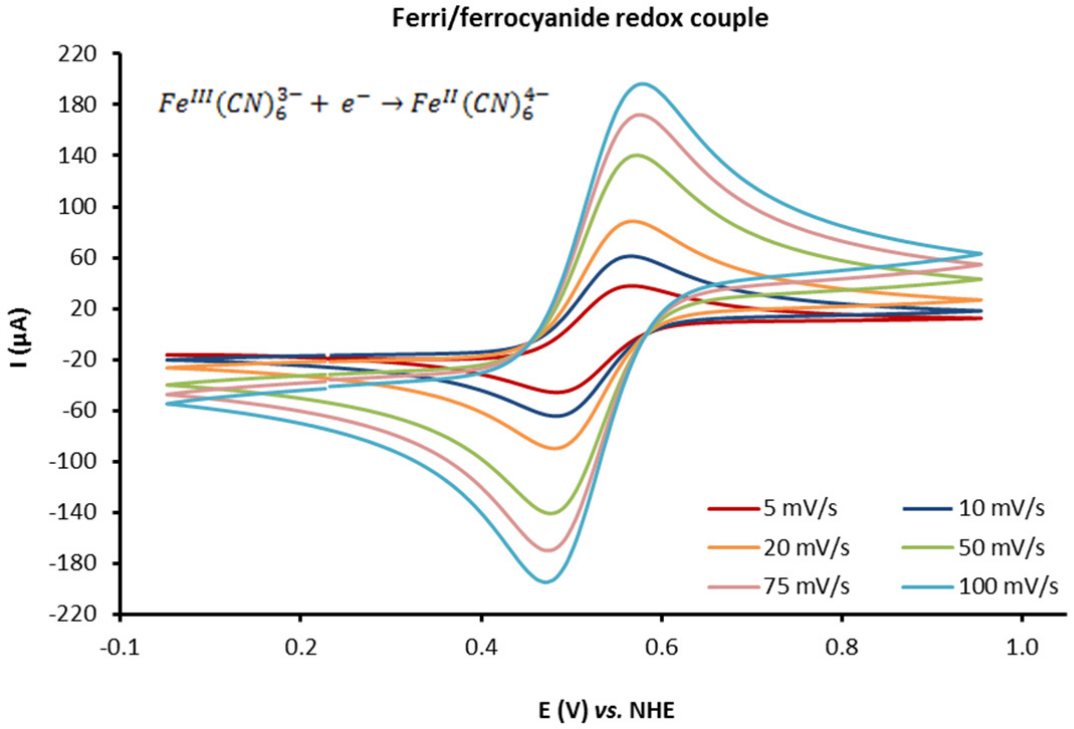

Figure J. 1 | Voltammogram for pyrolytic graphite electrode test, using a 10 mM ferri/ferrocyanide solution (*Sigma*) in 1 M KNO_3 (*Panreac*), between -0.2 to 0.7 V (*vs*. Ag/AgCl) at various scan rates.

The standard potential of the ferri/ferrocyanide redox pair in an aqueous solution at 25 ^{o}C is 0.316 V *vs*. NHE [16]. The formal potential for this pair in 1 M KNO_3 at 20 ^{o}C was determined to be 0.475 ± 0.001 V *vs*. NHE, which was considered to be close to the standard value. This indicated that the electrode was active and ready to be used in the electrochemical assays.

This test also allowed the determination of the real area of the working electrode, using the Randles–Sevcik equation:

$$I_p = (2.69x10^5)n^{3/2}AD^{1/2}C\upsilon^{1/2}$$

where I_p is the peak current (A), n is the number of moles of electrons transferred per mole of electroactive species (mol^{-1}), A is the electrode area (cm^2), D is the diffusion coefficient (cm^2/s), C is the concentration in (mol/cm^3), and υ is the scan rate (V/s). It is apparent from this equation that the peak current is proportional to the square root of the scan rate. Thus, a linear curve may be constructed from voltammograms at different scan rates (Figure J.2).

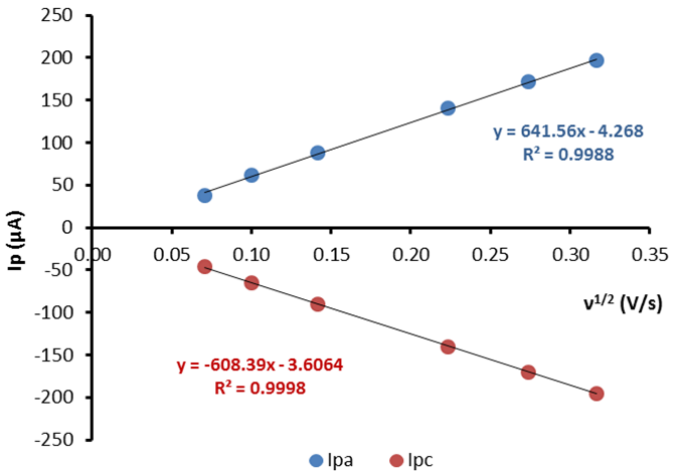

Figure J. 2 | Plot of the current peaks *versus* the square root of the applied scan rates, both for anodic and cathodic peaks.

Using one of the slopes obtained with I_p *vs.* $\upsilon^{1/2}$ and the known values of n, D (anodic or cathodic) and C, the real electrode area (A) was determined. Even though the experiment was performed in 1 M KNO_3, the diffusion coefficient value found in the literature [17] was determined through an experiment in 1 M KCl. However, these authors stated that little difference exists between KCl and KNO_3 as supporting electrolytes and, therefore, this value was used for the determination of A.

n = 1
$D_a = 0.726x10^{-5}\ cm^2/s$
$C = 10\ mM = 1x10^{-5}\ mol/cm^3$

$$641.56x10^{-6} = 2.69x10^5 * 1^{3/2} * A_{real} * (0.726x10^{-5})^{1/2} * 1x10^{-5} \Leftrightarrow A_{real} = 0.09\ cm^2$$

The geometric area was also determined, its value being 0.07 cm^2. As expected, the real area is greater than the geometrical area, since it accounts for the irregularities (roughness) in the electrode surface.

Appendix K - Appendix References

[1] J. Sambrook & D. W. Russell, *Molecular Cloning: A Laboratory Manual*, Third Edition, Cold Spring Harbor Laboratory Press, New York, 2001.

[2] "OverExpress Chemically Competent Cells", *Lucigen Corporation*, 2010, available at: http://lucigen.com/store/docs/manuals/MA031-OverExpress-Chemicallycompetent-Cells.pdf. [Accessed: Jan 9, 2012].

[3] "NZY5α Competent Cells", *NZYTech*, available at: https://www.nzytech.com/site/Competent-Cells/NZY5alpha. [Accessed: Oct 29, 2011].

[4] "E.Z.N.A. Plasmid Midi Kit", *Omega*, 2009, available at: http://www.omegabiotek.com/files/resource/Handbook/86058100.pdf. [Accessed: Nov 22, 2011].

[5] "NZYMiniprep", *NZYTech*, available at: https://www.nzytech.com/site/DNA-RNA-Purification-kits/NZYMiniprep. [Accessed: Jan 12, 2012].

[6] "2xYT Medium Broth", *Amresco*, 1998, available at: http://www.amresco-inc.com/media.acux?path=/media/products/dfu/dfu-J902.pdf. [Accessed: Jan 18, 2012].

[7] "RESOURCE S, 1 ml and 6 ml", *GE Healthcare*, 2011, available at: https://www.gelifesciences.com/gehcls_images/GELS/RelatedContent/Files/1314823637792/litdoc71714600AI_20110831225040.pdf. [Accessed: Sep 15, 2011].

[8] U. K. Laemmli, "Cleavage of Structural Proteins during the Assembly of the Head of Bacteriophage T4", *Nature*, vol. 227, (1970), pp. 680–685.

[9] O. H. Lowry, N. J. Rosebrough, A. L. Farr & R. J. Randall, "Protein measurements with the Folin phenol reagent", *Journal of Biological Chemistry*, vol. 193, (1951), pp. 265–275.

[10] "Bicinchoninic Acid (BCA) Protein Assay", *G-Biosciences*, 2010, available at: http://www.gbiosciences.com/634096940789210559.pdf. [Accessed: Sep 21, 2012].

[11] "Pierce ® BCA Protein Assay Kit", *Thermoscientific*, 2012, available at: http://www.piercenet.com/instructions/2161296.pdf. [Accessed: Sep 22, 2012].

[12] P. Tavares, "Estudo de Novos Centros Contendo Ferro: Isolamento e Caracterização de Proteínas de Desulfovibrio desulfuricans AlCC 27774", Doctoral Thesis, FCT-UNL, Lisbon, 1994.

[13] Maria de Lurdes Sadler Simões Gonçalves, *Métodos instrumentais para análise de soluções : análise quantitativa*, Third Edition, Fundação Calouste Gulbenkian, Lisbon, 1996.

[14] "pUC18/19 DNA", *GeneOn*, 2010, available at: http://www.taq-dna.com/puc18-dna-_149.html. [Accessed: Nov 22, 2011].

[15] "EcoR I", *Takara*, 2012, available at: http://www.clontech.com/takara/US/Products/Molecular_Biology/Restriction_Enzymes/Restriction_Enzymes_e_f/EcoRI. [Accessed: Feb 15, 2012].

[16] A. J. Bard & L. R. Faulkner, *Electrochemical Methods: Fundamentals and Applications*, John Wiley & Sons, Inc., New York, 2001.

[17] S. J. Konopka & B. McDuffie, “Diffusion coefficients of ferri- and ferrocyanide ions in aqueous media, using twin-electrode thin-layer electrochemistry”, Analytical Chemistry, vol. 42, no. 14, (1970), pp. 1741–1746.